MASARYKOVA UNIVERZITA
Přírodovědecká fakulta
Ústav fyzikální elektroniky

Diplomová práce

Brno 2021 **Dario Cipciar**

MASARYKOVA
UNIVERZITA
PŘÍRODOVĚDECKÁ FAKULTA
ÚSTAV FYZIKÁLNÍ ELEKTRONIKY

Ion and electron temperature study in the edge plasma of the tokamak device

Diplomová práce

Dario Cipciar

Vedoucí práce: prof. RNDr. David Trunec, CSc. **Brno 2021**

Bibliografický záznam

Autor:	Dario Cipciar Přírodovědecká fakulta, Masarykova univerzita Ústav fyzikální elektroniky
Název práce:	Studium iontové a elektronové teploty v okrajové oblasti plazmatu na zařízení typu tokamak
Studijní program:	Fyzika
Studijní obor:	Fyzika plazmatu a nanotechnologií
Vedoucí práce:	prof. RNDr. David Trunec, CSc.
Konzultant:	Mgr. Jiří Adámek, Ph.D.
Akademický rok:	2020/2021
Počet stran:	viii + 77
Klíčová slova:	tokamak COMPASS; iontová teplota; radiální profil; elektronová teplota; ball-pen sonda; Langmuirova sonda; SOL; RFA; pomer iónovej a elektrónovej teploty; L-mód

Bibliographic Entry

Author:	Dario Cipciar Faculty of Science, Masaryk University Department of electronics
Title of Thesis:	Ion and electron temperature study in the edge plasma of the tokamak device
Degree Programme:	Physics
Field of Study:	Plasma physics and nanotechnology
Supervisor:	prof. RNDr. David Trunec, CSc.
Assistant:	Mgr. Jiří Adámek, Ph.D.
Academic Year:	2020/2021
Number of Pages:	viii + 77
Keywords:	tokamak COMPASS; ion temperature; radial profile; electron temperature; ball-pen probe; Langmuir probe; SOL; RFA; ion to electron temperature ratio; L-mode

Abstrakt

V této diplomové práci se věnujeme systematickému meření iontové a elektronové teploty ve okrajovém plazmatu dvou tokamakových zařízení. Výsledky jsou získány pomocí rychle rozmítané ball-pen sondy s vysokým časovým rozlišením (10 μs). Je představena vylepšená analytická technika, která je nadstavbou dříve provedeného výzkumu. Výsledky s vysokým časovým rozlišením poukazují na ne-Gaussovské rozdělení teploty iontů s maximem při nízkých teplotách a ocasem do vysokých teplot způsobeným bloby. Bloby se vytváří v okolí separatrix a šíří se okrajovým plazmatem anomálním kolmým transportem. Rychlé meření (10 μs) se pak používají k simulaci *I-V* charakteristiky pomalého (3 ms) retarding filed analyzátoru (RFA). Pomocí lineárního fitu RFA-like *I-V* charakteristiky s okrajovými podmínkami citlivými na fluktuace získáváme téměř ploché radiální profily iontové teploty. Radiání profily iontové a elektronové teploty jsou studovány pro různé hustoty plazmatu, čímž se získají poměry 1-2 v blízkosti separatrix a 3-4 v hlavním SOL, v závislosti na hustotě plazmatu.

Abstract

This thesis reports on a systematic ion and electron temperature measurements in the scrape-off layer (SOL) of two tokamak devices. Results are obtained using a fast swept ball-pen probe with unprecedented temporal resolution (10 μs). Moreover, an improved analysis technique is presented which increases the amount of relevant data obtained in comparison to previously published research. The results with high temporal resolution indicate non-Gaussian ion temperature histograms with a peak at low temperatures and a high temperature tail associated with blobs. The blobs are originating in the vicinity of last closed flux surface and propagate perpendicularly to the magnetic field lines through the SOL plasma. The resulting fast measurements are used to simulate the *I-V* characteristic of a slow swept (3 ms) retarding field analyzer (RFA). The exponential part of the RFA-like *I-V* characteristic also determines the ion temperature, but with low temporal resolution (3 ms). The ratios of the ion to electron temperatures are studied for different plasma densities. We observed that the ratio depends on the line-average plasma density and it is close to 1-2 in the vicinity of LCFS and 3-4 in the main SOL. A study of the ion temperature fluctuations shows an agreement with a stochastic model for intermittent turbulence in SOL.

MASARYKOVA UNIVERZITA
PŘÍRODOVĚDECKÁ FAKULTA
KOTLÁŘSKÁ 2, 611 37 BRNO
IČ: 00216224
DIČ: CZ00216224

ZADÁNÍ DIPLOMOVÉ PRÁCE

Akademický rok: 2020/2021

Ústav:	Ústav fyzikální elektroniky
Student:	Bc. Dario Cipciar
Program:	Fyzika
Specializace:	Fyzika plazmatu a nanotechnologií

Ředitel *ústavu* PřF MU Vám ve smyslu Studijního a zkušebního řádu MU určuje diplomovou práci s názvem:

Název práce:	Studium iontové a elektronové teploty v okrajové oblasti plazmatu na zařízení typu tokamak
Název práce anglicky:	Ion and electron temperature study in the edge plasma of the tokamak device
Jazyk závěrečné práce:	angličtina

Oficiální zadání:
Cílem práce bude studium iontové a elektronové teploty v okrajové oblasti plazmatu na fúzním zařízení typu tokamak (COMPASS, ASDEX Upgrade, GOLEM) pomocí sondové diagnostiky. Měření elektronové teploty bude využívat již zavedenou techniku kombinace plovoucí Langmuirovy a ball-pen sondy. Hlavní důraz bude kladen na získání radiálních profilů iontové teploty z rozmítané ball-pen sondy v režimech s různou hustotou plazmatu. Cílem práce bude také srovnání získaných profilů s výsledky získanými jinou sondovou technikou jako je např. RFA (Retarding Field Analyzer).

Literatura:
CHEN, Francis F. *Úvod do fyziky plazmatu*. Vyd. 1. Praha: Academia, 1984. 328 s.

Vedoucí práce:	prof. RNDr. David Trunec, CSc.
Konzultant:	Mgr. Jiří Adámek, Ph.D.
Datum zadání práce:	14. 11. 2019
V Brně dne:	18. 4. 2021

Zadání bylo schváleno prostřednictvím IS MU.

Bc. Dario Cipciar, 15. 4. 2021
prof. RNDr. David Trunec, CSc., 15. 4. 2021
prof. RNDr. David Trunec, CSc., 15. 4. 2021

Acknowledgments

I would like to express my gratitude to my supervisor prof. RNDr. David Trunec, CSc. for his support and guidance, Mgr. Jiří Adámek, Ph.D. for his endless inspiration, patience and advises over the course of past years, Ing. Vojtech Svoboda, CSc. for making the measurements on the tokamak Golem possible, despite all the restrictions during pandemic. His enthusiastic approach and careful preparation of the tokamak experiment proved to be a great step forward in development of this unique technique. My thanks also belongs to RNDr. Jan Stockel, CSc. for his patience and indispensable advises during the experiments on tokamak Golem.

Prohlášení

Prohlašuji, že jsem svoji diplomovou práci vypracoval samostatně pod vedením vedoucího práce s využitím informačních zdrojů, které jsou v práci citovány.

Brno 1. June 2021 .....

Dario Cipciar

Contents

Chapter 1. Introduction **1**
1.1 Nuclear fusion, the process that powers the stars. 1
1.2 Controlled Thermonuclear fusion 3
1.2.1 Inertial confinement fusion 5
1.2.2 Magnetic confinement fusion 5
1.3 The tokamak design 6
1.3.1 The magnetic surfaces and the Last Closed Flux Surface 6
1.3.2 Plasma instability and energy loss 7
1.3.3 The shape of tokamak plasma and confinement modes 10

Chapter 2. Plasma diagnostics in a tokamak device **12**
2.1 Tokamak operation 12
2.2 Plasma heating 12
2.3 Electric probes 13
2.3.1 Langmuir probe 13
2.3.2 Retarding field analyzer 15
2.3.3 Ball-pen probe 16

Chapter 3. Measurement on the tokamak COMPASS **19**
3.1 Tokamak Compass 19
3.1.1 The Scrape-off layer 20
3.1.2 Experimental setup 20
3.1.3 Electron temperature measurement using floating LP and BPP 21
3.1.4 Estimation of the separatrix position 21
3.2 Ion temperature measurement using fast swept BPP 22
3.2.1 Signal preprocessing 22
3.2.2 4-parameter fit of the ball-pen probe electron branch 25
3.3 Improved analysis 26
3.3.1 The cut-off fitting technique 27
3.4 Results of measurements on COMPASS 30
3.4.1 Temporal evolution of plasma potential obtained with 10 μs resolution 31
3.4.2 The radial profile of the ion temperature 31
3.4.3 The temporal evolution of the plasma parameters 34
3.4.4 Statistical evaluation of the results with 10 μs resolution 34
3.5 Ion temperature obtained from RFA-like I-V characteristics 39
3.5.1 Fitting of the synthetic RFA-like I-V characteristics 39

3.5.2 Ion temperature radial profile from RFA-like *I-V* characteristics 40
3.6 Comparison of results from discharges with different densities 43
3.6.1 Limitations of the technique 44
3.6.2 Comparison of histograms resulting from the fast measurements during discharges with low and high density 45
3.6.3 Comparison of RFA-like radial profiles of discharges with low and high density 46
3.6.4 Ion and electron temperature density profiles 47

Chapter 4. Measurement on the tokamak GOLEM 48
4.1 Tokamak Golem 48
4.2 Measurement of the calibration constant α_{BPP} 49
4.2.1 Experimental setup 50
4.2.2 Signal preprocessing 50
4.2.3 Description of the method 50
4.2.4 Summary 54
4.3 Measurement of the ion and electron temperature on Golem 55
4.3.1 Experimental setup 55
4.3.2 Electron temperature measurement using floating LP and BPP 57
4.3.3 The ion temperature measurement 57
4.3.4 The cut-off fitting technique 59
4.3.5 Temporal evolution of ion and electron temperature 59
4.3.6 Ion temperature obtained from RFA-like *I-V* characteristics 61
4.3.7 Summary 62

Conclusion 65

Appendix 66

Bibliography 74

Chapter 1

Introduction

Electric energy is essential for our everyday lives. It powers all fundamental facilities which support life of almost every human on this planet and beyond. The economic growth and overall quality of life depends on cheap source of electric power. With further population growth and industrialization the energy demands will inevitably grow.

Existing low-cost energy solutions (coal, oil) in the perspective of worsening environmental impact will have to be replaced by green, sustainable sources of energy, no matter the cost. There are options for green sources of energy, however they usually come with downsides and limitations. Hydroelectric power is eco-friendly and inexpensive source of energy that will certainly make contribution to electricity production although it is limited to availability of high water-flow rivers and thus the possibilities for expansion are limited. On the other hand considering solar panels as an ecological source of energy is disputable. The manufacturing process uses harmful substances, produces waste water and emissions. Mass production of solar panels has began only recently and thus the problem with ecological disposal of solar panels is yet to be solved. Efficiency of solar panels and the limitation to daylight creates a need for significant number of solar panels covering a very large area that could be otherwise used for agricultural purposes. Also storage of electric energy in accumulators is quite difficult and expensive. The same limitations apply to wind power, since the strength of wind is non-constant an accumulator is needed. Production of significant amount of power from wind requires a great number of windmills over a very large area. Nuclear fission will always pose a risk of an catastrophic malfunction. The fuel supplies are limited and nuclear waste needs to be handled and stored with extreme caution.

It is obvious that no existing energy option can satisfy the requirements of an ideal source of energy, which could produce unlimited amounts of energy, without excessive land usage or CO_2 or toxic waste production and other drawbacks or disadvantages. The nuclear fusion as a source of energy has the potential to harness the benefits of both, ecological sources of energy in combination with power intensity and compact design of a nuclear reactor.

1.1 Nuclear fusion, the process that powers the stars.

Nuclear fusion is a process in which nuclei of two light elements merge (fuse) into one and release energy. In comparison to chemical reactions (e.g. burning of fossil fuel), where the electron structure of a molecule is rearranged and the molecular biding energy is released (fraction of eV per atom per reaction), the nuclear reactions cause rearrangements of the nuclei and thus chemical element transmutations. Since the stars similar to our Sun are composed mostly of hydrogen, the dominant set of reactions is proton-proton chain reaction. The stellar core must reach the temperature in order of 10^7 K and densities in order of 100 g/cm^3. The p-p chain is a series of

reactions including a weak-force interaction in form of a β^+ decay and consequent annihilation of the positron with a free electron. This set of reactions occurs in stellar core due to a low chance of deuterium meeting a tritium nucleus. In turn the energy produced by this reactions prevents the core form collapsing due to gravitational pressure [1]. For use on Earth the above mentioned cycle would not be beneficial. In order to produce electricity the important by-product are the high-energy neutrons. Ergo, all neutron initiated fusion reactions are unfavorable, since neutrons would be consumed rather than produced. The most favorable reactions for electric power generation are as follows [2]:

$$^2\mathrm{H} + {}^2\mathrm{H} \rightarrow {}^3\mathrm{He} + {}^1\mathrm{n} + \varepsilon(3.3\mathrm{MeV}),$$
$$^2\mathrm{H} + {}^2\mathrm{H} \rightarrow {}^3\mathrm{H} + {}^1\mathrm{H} + \varepsilon(4.0\mathrm{MeV}),$$
$$^2\mathrm{H} + {}^3\mathrm{H} \rightarrow {}^4\mathrm{He} + {}^1\mathrm{n} + \varepsilon(17.6\mathrm{MeV}),$$

where ^{2}H is the isotope of hydrogen called deuterium (D), ^{3}H is the isotope called tritium and ^{1}n is neutron. The unit 1 eV = 1.602 10^{-19} J. The amount of kinetic energy released by the reaction is represented by ε. It is obvious that these reactions do not produce any carbon emissions or other greenhouse gasses. Since (D-T) reaction releases significantly more kinetic energy than (D-D) reaction and has the highest cross-section it is of the main interest for electricity production. The end product of fusion would be harmless helium. Another reason supporting fusion energy is an abundance of deuterium in ocean water. 1 liter of ocean water contains 0.00015 % of deuterium, which is the energy equivalent of 300 liters of gasoline. Since there is so much water, the supplies of deuterium for nuclear fusion reaction on our planet would last for approximately 2 billion years, if we consider the present total energy demands [3]. After the fusion occurs the released kinetic energy of 17.6 MeV is divided between the two products inversely proportional to their masses. Thus the neutron will carry away majority of the binding energy (14.1 MeV) and heavier alpha particle will carry away the rest (3.5 MeV). The main problem with using this particular reaction in nuclear fusion devices is the absence of naturally occurring tritium, since tritium has a half-life of only 12.3 years. Solution of this problem is breeding of tritium by absorption of neutron in lithium isotope ^{6}Li. The fusion blanket, which surrounds the vessel of the fusion reactor can be used for capturing the energetic neutrons and converting their kinetic energy into heat and consequently into rotation of a steam turbine. The lithium ^{6}Li could be preset in the fusion (breeding) blanket, thus the needed tritium can be produced simply as a by-product of the process itself using a reaction:

$$^6\mathrm{Li} + {}^1\mathrm{n} \rightarrow {}^4\mathrm{He} + {}^3\mathrm{T} + \varepsilon(4.9\mathrm{MeV}).$$

Thus the fuel for a fusion reactor is only limited by the availability of ^{6}Li on Earth, which is estimated to last on the order of 20000 years. The key difference between fusion reactor and fission reactor is the amount of fuel present in the reactors core. While inside the fission reactors core several tons of highly unstable fission material is present during the whole operation, the fusion reactor core would contain less than 1 g of fusion fuel at a moment. The fuel for nuclear synthesis would be injected into vacuum vessel at a controlled rate corresponding to it's consumption rate and hence the operation poses no risk of nuclear meltdown as we know it. This key difference implies the inherent safety of fusion.

The issues of nuclear fusion are mostly of technological complexity and also include handling of radioactive tritium. However, the big advantage of fusion comparing to fission is the short half-life of tritium. Thus nuclear waste would have to be stored only in order of a hundred years. The amount of unburned tritium can be reduced by fusion fuel recycling, which breaks down to just another engineering challenge. The neutrons produced by fusion will also cause structural activation, before they are absorbed by the fusion blanket. This effect can be deteriorated by a good choice of materials. The success of fusion depends upon mastering of all the technological challenges and finding a practical design of a reactor with favorable power balance.

1.2 Controlled Thermonuclear fusion

The basic concept of thermonuclear method is based on giving the deuterium and tritium nuclei enough kinetic energy to overcome the repulsive forces and approach each other close enough for the strong short-range attractive nuclear interaction to take place. An illustration of this process is shown on Fig. 1.1, where the repulsive only Coulomb potential adds up with attractive only nuclear strong interaction to form a total potential, which becomes attractive if the distance of nuclei r is in order of 1 fm. Deuterium nuclei need an energy in order of 100 keV for breaking the Coulomb barrier. One possible way how to achieve such energies is in a particle accelerator. However, such a device is inherently energy inefficient and the energy used to accelerate the particles would outweigh the energy gained by fusion. The other possible way is the Thermonuclear fusion. In the thermonuclear reactor all particles are heated instead of individual ones and thus the temperature of particles is normally distributed. High-energy particles from the hot-tail of distribution are fusion capable even though the mean plasma temperature needed is in order of 10 keV. These particles will ignite the fusion reactions.

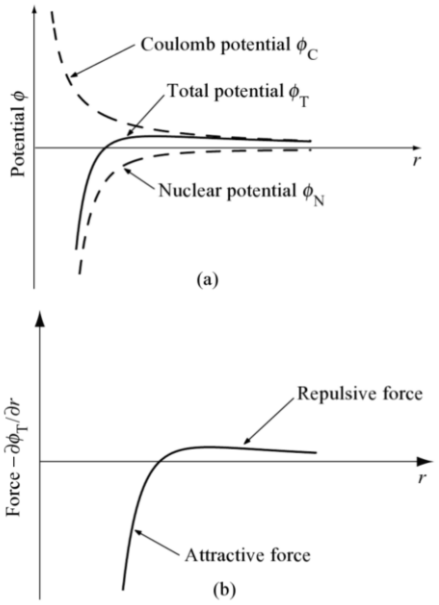

Figure 1.1: (a) Potential energies of the Coulomb, nuclear and total interaction ; (b) the corresponding total force $F(r) = -\frac{\partial \phi_T}{\partial r}$ [3].

If we consider an element with N neutrons and Z protons, the integer sum of individual isolated particles gives only an approximate nuclear mass $A : N + Z \approx A$. Comparison of experimentally measured nuclear mass m_A with sum of the masses of isolated particles (namely protons (m_p) and neutrons (m_n) shows that

$$N m_\mathrm{n} + Z m_\mathrm{p} > m_A. \tag{1.1}$$

The difference in mass corresponds to the nuclear binding energy E_B defined as:

$$E_\mathrm{B} = (N m_\mathrm{n} + Z m_\mathrm{p} - m_A)c^2. \tag{1.2}$$

The reason for choosing elements with the lowest nuclear masses as a fuel for a reactor is the following. We can compare the binding energy per nucleon defined as E_B/A, describing the average binding energy an individual nucleon, for all the elements. We find that the forces binding the

nucleons are the weakest for very light elements and strongest for the element iron (A = 56) see Fig.1.2.

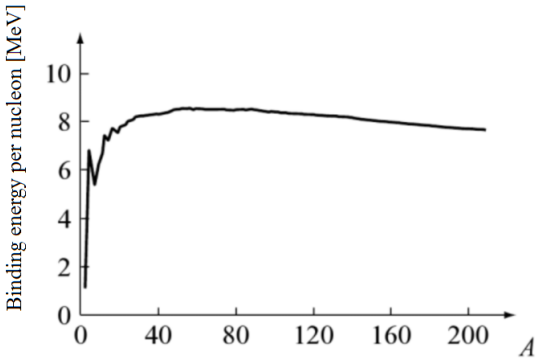

Figure 1.2: Binding energy per nucleon for the dominant form of each chemical element [3].

Hence initiation of nuclear reaction is easier either for elements much lighter or much heavier than iron. Energy is released when the reactants have lower binding energy per nucleon than the end product. Thus nuclear fusion can produce energy when binding two elements lighter than iron and nuclear fission is energetically favorable when splitting nuclei of elements heavier than iron.

Now we know which fuel to use in order to produce energy and why. Criterion which defines the conditions under which the D-T fusion reaction will take place is called the Lawson criterion. This criterion is based on a requirement of positive power balance where more power is generated by fusion (P_{gain}) than power lost (P_{loss}). It defines the energy confinement time as $\tau_E = \frac{W}{P_{\text{loss}}}$, where W the total energy of heated plasma. This variable is useful, since instead of complicated calculation of all possible P_{loss} (Bremsstrahlung, heat transfer) we can use τ_E as a measure of these losses. The internal plasma energy can be obtained as:

$$W = \frac{3}{2} n_{\text{i}} k T_{\text{i}} + \frac{3}{2} n_{\text{e}} k T_{\text{e}} = 3 n_{\text{e}} k T, \text{ while } n_{\text{i}} \approx n_{\text{e}}. \tag{1.3}$$

From $P_{\text{gain}} > P_{\text{loss}}$, we can write:

$$< \sigma v > n_{\text{D}} n_{\text{T}} E_{3.5\text{MeV}} > P_{\text{loss}}, \tag{1.4}$$

where $< \sigma v > n_{\text{D}} n_{\text{T}}$ can be written (for equal ratio of deuterium to tritium) as $\frac{1}{4} n_{\text{e}}^2 < \sigma v >$ is the D-T collision rate, σ is the cross section of D-T reaction, v is relative velocity $<>$ denotes the mean at the temperature T of a Maxwellian velocity distribution and $E_{3.5\text{MeV}}$ is the kinetic energy of He ions (product of D-T reaction). We can substitute for P_{loss} and receive:

$$\frac{1}{4} n_{\text{e}}^2 < \sigma v > E_{3.5\text{MeV}} \geq \frac{3kT}{\tau_E} n_{\text{e}}, \tag{1.5}$$

Which can be simplified to:

$$n \tau_E \geq \frac{12}{E_{3.5\text{MeV}}} k \frac{T}{< \sigma v >} = L \approx 1.5 \times 10^{20} \text{s m}^{-3}, \tag{1.6}$$

where T is temperature and n is volume-averaged density. Firstly we need the parameter L to be small. The function 1.6 for D-T reaction has a minimum at T = 15 keV (given by temperature dependency of the collision rate $< \sigma v >$). All the other possible reactions (as D-D) would require

even higher temperatures (have higher L). Secondly if we know the Lawson parameter L we need to increase the confinement time or density for ignition to occur. In order to achieve such conditions the fusion plasma needs to be isolated from any physical material. Such plasma literally needs to levitate in vacuum, which can only be achieved by:

- gravitational confinement
- inertial confinement
- magnetic confinement

The goal is to reach such confinement time, density and temperature, that overall power balance would be $P_{\text{out}} > P_{\text{in}}$. The tokamak concept is presently the leading candidate for fusion power generation, due to achieved parameters τ, n, T very close to meet the Lawson criterion. The typical plasma density in a tokamak device is $n = 10^{20}$ m^{-3}. Higher density is inconvenient, due to limited maximal magnetic field (technological maximum for B is 13T, given by material strength of the coils). Increasing plasma density, while keeping the toroidal magnetic field constant, due to construction limitations, would lead to increase of plasma pressure, anomalous transport and instabilities as pinch, sausage and kink instability and consequently collapse of plasma.

1.2.1 Inertial confinement fusion

This approach utilities extremely high density n in order to reach Lawson criteria. The fuel in form of a D-T ice pellet is exposed to intense laser radiation (X-ray pulse) or heavy ion bombardment. The external pressure applied must be spherically symmetrical (multiple lasers). The high density is reached in a very short time in the center of the pellet, due to sudden heating and expansion of the outer layer of the pellet. An example of such device is a hydrogen bomb.

1.2.2 Magnetic confinement fusion

In order to reach the Lawson criterion we can trap charged particles in an enclosed toroidal magnetic filed (B_{t}). Charged particles are thus forced to perform helical movement along magnetic field lines, thus the confinement time τ_E will become much longer than the inertial value. The movement of a charged particle (cyclotron rotation) is described by a Larmor radius

$$r_{\text{L}} = \frac{m v_{\perp}}{QB}, \tag{1.7}$$

where $v_{\perp}$ is the velocity perpendicular to $\vec{B}$. Velocity ($v^2 = v_{\perp}^2 + v_{\parallel}^2$) is in general given by plasma temperature T as $\frac{1}{2}mv^2 = k_{\text{B}}T$. Now when we can adjust confinement time, we can rise the pressure and achieve the condition 1.6 to be fulfilled. Two successful concepts utilising magnetic confinement were introduced. The stellerator and the tokamak. The geometry of the magnetic field and vacuum vessel is a torus in both cases, thus the magnetic field lines form nested magnetic surfaces. The key difference is how these machines solve the issue of instability caused by drifts of charged particles. The toroidal magnetic field causes the creation of strong magnetic field on the inner side of torus (High Field Side or HFS) and weaker field on the external side (Low Field Side or LFS). This causes the $\nabla\vec{B} \times \vec{B}$ drift. Oppositely charged particles drift in axial direction away form each other (vertical drift), which gives rise to an electric field and thus $\vec{E} \times \vec{B}$ drift, pushing the charged particles radially outwards. Therefore an additional poloidal magnetic field is needed to compensate vertical drift.

In the stellerator the poloidal field is created by complex (non-planar) geometry of external coils. The poloidal magnetic field is constant which is the advantage of this approach, since the operation does not need to be pulsed. In the tokamak design, the same effect is reached by an induction of strong toroidal current (I_p) in the highly conductive plasma. In order to induce this current a transformer is used. A large toroidal coil makes primary wiring and the secondary wiring is the plasma itself. This induced current creates an additional poloidal field, which moves charged particles poloidally and thus on average effectively suppresses the $\nabla\vec{B}\times\vec{B}$ drift. The superposition of toroidal magnetic field with a poloidal magnetic field gives rise to magnetic field with shape of a helix. The scheme of above described tokamak concept is shown on Fig. 1.4. The outer poloidal coils are important for producing a non-circular cross section to improve MHD stability limits and alleviate plasma-wall impurity problems [3].

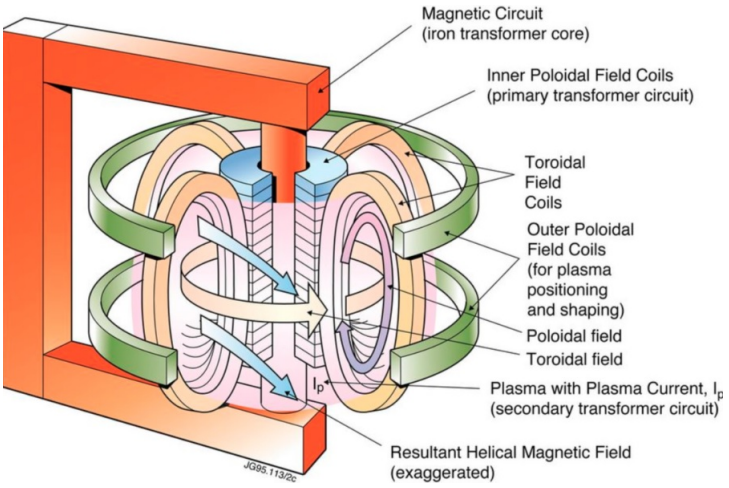

Figure 1.3: Scheme and description of a typical tokamak device. [4].

1.3 The tokamak design

1.3.1 The magnetic surfaces and the Last Closed Flux Surface

The isobaric surfaces are an interesting hypothetical concept derived form motion of electrically conducting liquid (plasma) placed in magnetic field. The study of properties of such conducting liquid is studied by MagnetoHydroDynamics (MHD). Therefore we will describe the motion of plasma with the momentum conservation law of MHD written as

$$\rho_\mathrm{m}\frac{\partial\mathbf{v}_\mathrm{m}}{\partial t}=\mathbf{j}\times\mathbf{B}-\nabla p+\rho_\mathrm{m}\mathbf{g}, \tag{1.8}$$

where $\mathbf{v}_\mathrm{m}$ is the speed of liquid with density ρ_m, $\mathbf{j}$ is current flowing through liquid in magnetic field $\mathbf{B}$. Term $\rho_\mathrm{m}\mathbf{g}$ describes gravitational forces which can be neglected. The ∇p denotes kinetic pressure. The vector ∇p, normal to the surface at any point, is called isobaric surface, over which the kinetic pressure is constant. Using a hydrostatic simplification for non-accelerating liquid in equilibrium we receive

$$\mathbf{j}\times\mathbf{B}=\nabla p. \tag{1.9}$$

Since the ∇p is perpendicular to both $\mathbf{B}$ and $\mathbf{j}$ we can write

$$\mathbf{B}\nabla p=0$$

$$\mathbf{j}\nabla p = 0.$$

Therefore both **B** and **j** lie on isobaric surfaces and thus the isobaric surface becomes the magnetic surface. For the collision-less case the charged particles follow their magnetic surface. Also we can see that the $\mathbf{j} \times \mathbf{B}$ creates a kinetic pressure with direction toward the center of torus. Thus it is counterbalancing the effect of expansion of hot plasma from center. Unfortunately the plasma has a finite resistivity, due to collisions that inevitably happen, the assumption of charged particles "frozen" on a field lines is not entirely true. These little deviations from ideal MHD cause instabilities discussed in the next section.

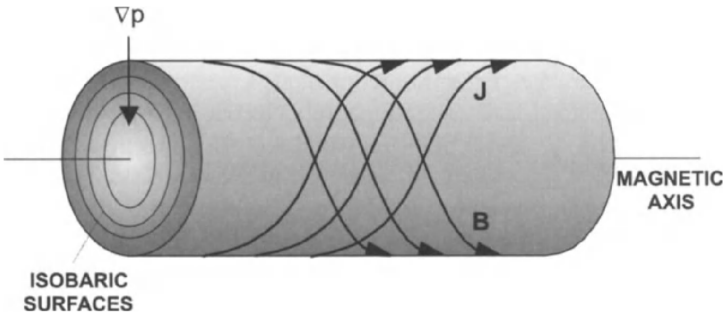

Figure 1.4: Concentric isobaric surfaces, with ∇p increasing in radial direction toward magnetic axis. Vectors **j** and **B** follow $\mathbf{j} \times \mathbf{B} = \nabla p$. [2].

In tokamak plasma the Last Closed Flux Surface (LCFS) is than a boundary between closed magnetic field lines (core plasma) and opened filed magnetic field lines (edge plasma or scrape-off layer), where the field lines cross the material limiters. In divertor configuration the LCFS forms a crossing called X-point before connecting to a divertor located at the bottom of the tokamak. The LCFS separates two regions with distinct properties.

1.3.2 Plasma instability and energy loss

As mentioned above, the plasma particles tend to follow enclosed magnetic field lines on magnetic surfaces, however due to drifts and collisions the particles can move across magnetic field lines. This effect is undesirable for confinement and can lead to plasma breakdown (disruptions) and damage of the wall materials. For if a slight disturbance occurs the motion of particles related to it can deform the magnetic field and produce forces that will amplify the original disturbance.

Collisions are necessary for fusion to occur, however they cause the diffusion across magnetic field this diffusion. The radial particle flux Γ_r is given by Fick's law [2] given as:

$$\Gamma_r = -D_\perp \nabla n = -D_\perp \frac{dn}{dr}, \tag{1.10}$$

where $D_\perp$ is the diffusion coefficient. The exact form of $D_\perp$ depends on the model we take into consideration. The classical diffusion coefficient $D_\perp \propto 1/B^2$. If we account also for the drifts in toroidal systems including plasma turbulence and consequent $\mathbf{E} \times \mathbf{B}$ drift we receive Bohm diffusion with $D_\perp \propto 1/B$.

Plasma instabilities pose another problem. Two types of instabilities occur, macroscopic and microscopic. The macroscopic instabilities studied by MHD affect the plasma on a global scale. Hot plasma which we attempt to confine in magnetic field is not in thermodynamic equilibrium, since the core temperature is much greater than at the edge temperature. This means that if a disturbance disrupts the (unstable) equilibrium the potential energy will turn to kinetic energy.

Perhaps the most important macroscopic instability is an interchange instability in tokamak plasma, which is called Flute instability. The flute instability occurs when a wave-like ripple develops on the plasma-vacuum interface. Charged particles in curved, non-uniform magnetic field (such as toroidal magnetic field) are affected by a curvature drift. The curvature drift is charge dependent leading to a charge separation and $\mathbf{E} \times \mathbf{B}$ drift. The flute instability arises when, the radius-of-curvature vector is directed away from the region of maximum plasma pressure. The resulting surface of the plasma becomes rippled with filaments of plasma, which will move outwards. Inwards moving filaments of vacuum will compensate for this effect. [5]. Principle of this effect is shown in Fig. 1.5. Similar effect is observed in gravitational field, where it is called Rayleigh-Taylor instability, which occurs when liquid with higher density is above lower density liquid. Any disturbance that occurs will grow until the whole system will suddenly fall into state with lower energy.

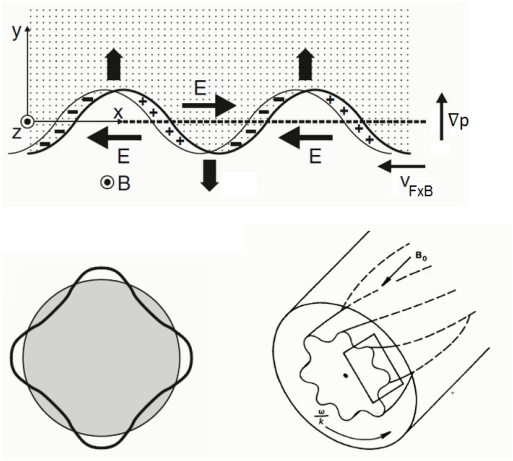

Figure 1.5: Top: The mechanism of Flute instability. Curvature drift, due to non-uniform magnetic field leads to charge separation on the plasma-vacuum interface. Consequent electric field in combination with magnetic field causes drift that amplifies the initial perturbation. Bottom: The resulting rippled plasma on the plasma-vacuum interface due to flute instability [5].

The possible way of overcoming this instability is creation of magnetic shear layers. The shear layer is an interface between magnetic surfaces with differently oriented **B** (see Fig. 1.6). The mentioned instability is created on isobaric surfaces with suitably oriented magnetic field. The parallel transport will be diminished due to change of magnetic field direction as the instability transverses the isobaric surfaces with unsuitable orientation.

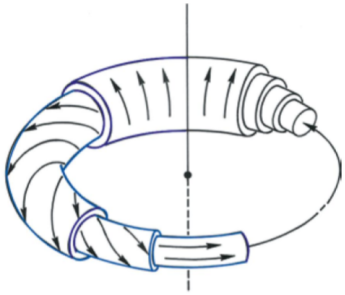

Figure 1.6: The mechanism of Flute instability prevention by creation of magnetic shear layers. [7].

Disruptions and on large tokamak devices are particularly harmful to plasma facing components such as divertor. Means of prevention of such instabilities are the mentioned magnetic shear layers, confinement of hot plasma in region with absolute minimum in the strength of the magnetic field and dynamical stabilization. On the International Thermonuclear Experimental Reactor (ITER), currently under construction, special Disruption Mitigation Systems or DMS, will be installed, which can trigger a massive gas injection to protect the reactor from damage if a disruption is detected. The early response of this system will be of a crucial importance [6].

Microscopic instabilities play a role on a small scale (gyration radius, mean free path) and are studied by kinetic theory requiring numerical simulations. These instabilities are caused by ions gyrating around guiding center what gives rise to Finite Larmor Radius effect (FLR). Instabilities can also be caused by a deviation in Maxwellian velocity distributions, an effect called Landau damping. Sometimes even small electron inertia plays a role. The plasma is always be more dense at the center of torus rather than at the outside, this creates pressure that acts against the applied magnetic pressure. Also if there is even a small resistivity, the plasma is able to create electric fields that allow it to move perpendicular to the magnetic field lines to the tokamak walls. The density gradient leads to microscopic instabilities like ion diamagnetic drift. One particularly important microscopic instability is an ion temperature gradient instability. It is a form of resistive drift instability, where initial waves break up into blobs of higher density and temperature, which drift onto the walls by their internal electric field [7]. The formation mechanism of such instability, as the name suggests, lies with the ion temperature gradient (∇T) in combination with suitably aligned $\nabla \mathbf{B}$, which is proportional to particle's temperature. As a result of ions drifting with $\nabla \mathbf{B}$ drift in the temperature gradient, the ions with higher temperature will drift further than ions with lower temperature. This leads to charge separation, internal electric field and $\mathbf{E} \times \mathbf{B}$ drift. The resulting drift increases with size of such perturbation and creates new temperature perturbations and consequently exponential growth of instability (positive feedback loop see Fig. 1.7). This means that plasma propagates toward walls in "bunches" or blobs or higher density. These blobs form rather long tubes or filaments than spheres. It is actually possible to take a photograph of blobs moving radially outwards on tokamak device (Fig. 1.8).

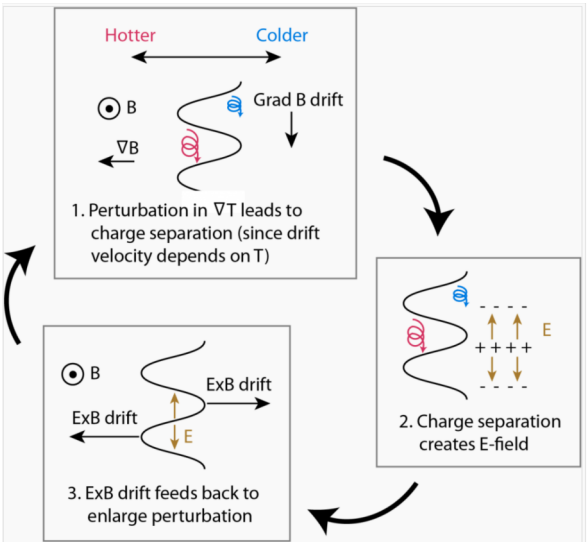

Figure 1.7: The mechanism of ion temperature gradient instability. [8].

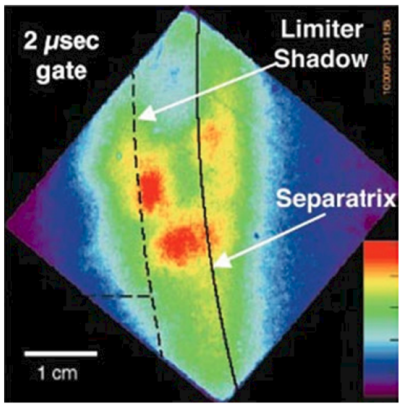

Figure 1.8: The resulting blobs of plasma moving radially outwards (left) due to ion temperature gradient instability. Taken with a shutter speed of 2μ s [7].

1.3.3 The shape of tokamak plasma and confinement modes

In tokamak the plasma is confined in a region of enclosed magnetic field lines. Separatrix creates an interface, which separates central plasma and the edge plasma region called Scrape Off Layer (SOL). However, the products of fusion reactions (plasma exhaust, He) and impurities (desorbed form vessel) still need to be removed from magnetically confined plasma. Impurities, in form of heavy elements, cause cooling of plasma and lead to instabilities. In order to remove these particles two main concepts were created.

The first concept of tokamak device keeps the edge plasma in direct contact with a light metal plate called limiter. The plasma than hits the limiter rather than the walls of a vacuum vessel. Since limiter is composed of lighter elements than wall materials, physical sputtering of limiter material is less disruptive. The heat load on limiter is inevitably very high, which brings technological limitations to plasma parameters. Typical shape of plasma (the cross-section) in a tokamak with limiter configuration is circular. Due to unavoidable impurity contamination only the Low confinement (L-mode) is possible in this configuration.

The second configuration creates D-shaped plasma, typical for all of the current leading experiments (JET, ASDEX-U). In this configuration the escaping plasma is channeled along field lines, that leave the LCFS and lead outwards into an external plate, called divertor, where it recombines and is pumped out. The divertor is located at the bottom of torus, under the crossing of LCFS, called X-point, thus it is not in direct contact with confined plasma. This brings an important advantage for capturing the impurities. The greatest advantage of a divertor configuration is possibility to achieve a mode with High confinement called H-mode. In this operating mode significantly higher temperatures, pressures and $2\times$ longer confinement time are achieved. These properties are reached as a consequence of creation of a pressure pedestal of the Edge Transport Barrier (ETB). The ETB performs as an isolation "wall" greatly decreasing the amount of escaping particle flux. The increase in confinement is observable by the disappearance of the H_α emission line. Surprisingly ETB is created by the power loss itself. Inside it the strong electric field crates an $\mathbf{E}\times\mathbf{B}$ drift in toroidal direction, creating and electric shear. The strong toroidal shear is not susceptible to microscopic instabilities, discussed in previous section, and greatly slows down the instability-controlled diffusion [7]. H-mode has typical periodical oscillations between the L-mode and H-mode, called Edge Localized Modes (ELMs). The ELMs play an important role in plasma exhaust transport, since H-mode does not allow for particles to escape.

A new improved confinement mode called I-mode was observed in the Alcator C-Mod toka-

mak. I-mode combines performance benefits of both L-mode and H-mode. Key feature is an edge energy transport barrier, without a particle barrier. I-mode has a stationary temperature pedestal with edge localized modes typically absent, while plasma density is controlled using divertor cryopumping [9]. This means that the impurities are not confined in the core plasma, while the energy confinement of the H-mode remains preserved.

Chapter 2

Plasma diagnostics in a tokamak device

2.1 Tokamak operation

Presence of impurities in form of heavy elements is undesirable in tokamak plasma. Impurities cause rapid cooling of the plasma and also affect probe measurements. Reaching low impurity contamination is very important for our experiment, as well as for eventual reaching the thermonuclear fusion. In a tokamak device impurities are released due to plasma-surface interactions at a limiter or at the target plate in magnetically diverted discharges. The impurity release processes include arcing, thermal desorption, particle induced desorption and sputtering [10]. In order to decrease the impurity content a purge is performed before the tokamak operation (usually after tokamak opening), which typically consists of two phases:

- Vessel baking. The tokamak vessel is heated up to high temperatures (roughly 250 °C) for the duration of about 10 minutes. Molecules (H_2O , O_2, N_2) adsorbed in the walls of the vacuum vessel are released (through thermal desorption) and removed using a vacuum pump.
- Helium glow discharge. An glow discharge in an inert gas is performed, releasing particles such as hydrogen, trapped in the tokamak walls [11] or carbon dust deposited on the wall surface. The vessel is negatively biased in order to achieve ion bombardment. The toroidal magnetic field (B_t) is not applied, thus very low confinement is achieved.

Operation of tokamak typically begins with establishment of a strong toroidal magnetic field (B_t). Afterwards the working gas is injected into evacuated chamber and pre-ionized. The most common pre-ionisation technique is electron cyclotron resonance heating and upper hybrid resonant heating. The power is introduced into plasma using a gyrotron device, which generates millimeter-wave electromagnetic radiation which corresponds to electron cyclotron frequency in a magnetic field. Other technique for pre-ionisation is the thermal emission electron gun [12]. After the pre-ionisation the plasma current can be induced by the transformer. The toroidal current is ”ramped-up” to desired value and held constant. The constant phase in discharge is called ”flat-top”. Most experiments and additional plasma heating (NBI) is performed during this phase.

2.2 Plasma heating

The transformer's function apart from plasma stabilization is also an ohmic heating. The voltage induced by transformer coil, which drives the plasma current through highly conductive plasma column is called loop voltage U_{loop}. The ohmic heating power is than given as $P_{OH} = U_{loop} I_p = \eta U_{loop}^2$, where $\eta \propto T^{-3/2}$ corresponds to plasma resistivity. The analysis shows that maximum

temperature achievable by P_{OH} is T lower than 3 keV [3]. Thus for desired high plasma temperature ($T = 15$ keV) ohmic heating becomes ineffective and additional sources of energy are needed. Widely used plasma heating technique is Neutral Beam Injection (NBI) and RF heating. The NBI utilities a high-energy beam of neutral deuterium atoms injected into the plasma. The reason for using atoms instead of ions is that ions can not penetrate the magnetic field, while neutrals are unaffected. Thus a neutral beam propagates in a straight line until ionized and than passes its energy to surrounding particles through Coulomb collisions.

2.3 Electric probes

Plasma diagnostics play a crucial role in understanding various plasma processes and verification of constantly evolving plasma simulations. The success of nuclear fusion depends upon correct measurements, computer models and resulting predictions. Electric probes are one of the oldest, but most important plasma diagnostic tools. They operate in scrape-off layer of plasma, where other diagnostic techniques cannot be used. For example, electron temperature can be very precisely measured in the core plasma using Thompson scattering technique, but not in SOL. The role of probe measurements in scrape-off layer is of an increasing interest. In particular the plasma-wall interactions and consequent impurity production and transport into the core plasma is of a great concern. Measurement of distribution of the ion energy incident on plasma-facing component is important for determining of physical sputtering of the material and impurity release, while chemical sputtering depends on surface temperature and constituent elements of the plasma-facing component.

2.3.1 Langmuir probe

The Langmuir probe (LP) still belongs to most commonly applied diagnostics of tokamak edge plasma. In the most typical configuration the probe tips are cylindrical pins at normal incidence to the magnetic field. The tips are made out of highly conductive metal capable of withstanding high temperatures (tungsten). They are used in tokamak edge plasma to determine the electron temperature (T_{e}), electron density (n_{e}) and floating potential (V_{fl}). Langmuir probes are installed on tokamak devices in various configurations. Flush-mounted Langmuir probes can be embedded in divertor plates and limiters, rake probes consist of an array of LPs and are ideal for profile measurements. Double probes, triple probes and many other configurations are developed and implemented. In this thesis we have performed measurements with single, so called, proud Langmuir probes (electrodes extend into the volume of the plasma) installed on a fast probe drive and reciprocated by an external system of pneumatic pistons.

An advantage of Langmuir probes is high spacial and temporal resolution and ease of data analysis. However, correct interpretation of the data can be difficult and usually it is based on assumption that the plasma is uniform with Maxwellian velocity distribution with $T_{\mathrm{i}} \approx T_{\mathrm{e}} \approx T$ in three dimensions:

$$f(v) = \left(\frac{m}{2\pi kT}\right)^{3/2} 4\pi v^2 \exp\left(\frac{-mv^2}{2kT}\right), \quad \text{where} \quad v = ||\vec{v}|| \tag{2.1}$$

Than the velocity distribution, just in front of the probe surface, where the particles with the direction away from the probe surface are absent (absorbed by the probe), is given by approximately one half of a Maxwellian distribution. The particle flux to the probe surface is given as:

$$\Gamma_\alpha = \frac{1}{4} n_\alpha < v >_\alpha \quad \text{with} \quad < v >_\alpha = \sqrt{\frac{8kT_\alpha}{\pi m_\alpha}} = \int_0^\infty v_\alpha f(v_\alpha)\, dv_\alpha, \tag{2.2}$$

this holds for the electrons and ions separately (particle species denoted by α), where n_α is the local plasma density of ions or electrons in the vicinity of the probe. Thus when $T_\mathrm{i} \approx T_\mathrm{e}$ more electrons will reach the probe surface comparing to much heavier ions. Therefore an insulated probe will reach an equilibrium ($I = 0$) at a negative potential called floating potential ($V_\mathrm{fl}^\mathrm{LP}$), which is lower than local plasma potential Φ. Voltage is measured relative to a reference electrode which is also in contact with plasma (tokamak vessel). Since the probe operates in tokamak devices, the plasma is typically magnetized. Ions and electrons are gyrating around guiding center with different gyration radius (equation 1.7) in magnetized plasma. The typical probe dimensions (1 mm) are comparable to r_L of ions, thus the probe has higher effective collection area for ions. We can express the floating potential in terms of effective collection areas for ions and electrons A_i and A_e, respectively as [13]:

$$V_\mathrm{fl}^\mathrm{LP} = \Phi - \alpha_\mathrm{LP}\left(\frac{kT_\mathrm{e}}{e}\right), \quad \text{where} \quad \alpha_\mathrm{LP} = \ln\left|\frac{j_\mathrm{sat}^\mathrm{e} A_\mathrm{e}}{j_\mathrm{sat}^\mathrm{i} A_\mathrm{i}}\right| = \ln\left(\frac{I_\mathrm{sat}^-}{I_\mathrm{sat}^+}\right), \tag{2.3}$$

where T_e is the electron temperature, e and k denote the elementary charge and Boltzmann constant, respectively. I_sat^- and I_sat^+ represent the electron and ion saturation currents, respectively. The coefficient α_LP is not routinely measured due to difficulty with magnitude of I_sat^-. When Langmuir probe is operating in electron saturation mode the currents are rather high even in the edge plasma of tokamak device and the probe can be destroyed by high power loads. The value of $\alpha_\mathrm{LP} = 2.8$ was experimentally obtained and used on tokamak COMPASS and ASDEX-U [14]. In the absence of magnetic field this ratio is much higher.

By connecting the probe to an external circuit and applying swept voltage we can measure the voltage-current dependency or so-called I-V characteristics. A conventional analysis of such characteristics assumes that the electron current saturates and the characteristic is described by analytical function [10]:

$$I = I_\mathrm{sat}^+\left(1 - \exp\left(\frac{V - V_\mathrm{fl}}{kT_\mathrm{e}/e}\right)\right), \quad \text{for} \quad V < \Phi \tag{2.4}$$

where I is the probe current measured at certain voltage V applied to the probe. By performing non-linear fit one can obtain the following parameters: The floating potential V_fl, the ion saturation current I_sat^+ and the electron temperature kT_e/e (eV). The exponential term is due to the before mentioned Maxwellian distribution of electron velocities. The electron current decays exponentially as a direct consequence of an increase in the applied repulsive potential. The ion saturation current measured for V sufficiently negative ($V_\mathrm{fl} - V \gg kT_\mathrm{e}/e$) is typically assumed to be a constant contribution to the total probe current and is caused by the ions accelerated in the pre-sheath towards the probe surface, independently on the probe potential as long as it is negative relative to the plasma potential. At the floating potential the probe current equals zero.

However, effects of sheath expansion are causing that the I-V characteristics not to saturate, but the current rather continues to increase linearly with voltage applied. These non-saturating characteristics are assumed to be due to growing effective collection area given by the Debye sheath. To overcome this problem one could increase the physical size of the probe to be much larger than the Debye sheath, but this approach is impractical. Therefore, a model for analysis is often used, which takes into account even the possibility of the probe current linearly growing with the applied voltage. Fitting of the Langmuir probe characteristic is than performed using a 4-parameter formula given as [16]:

$$I = I_\mathrm{sat}^+[1 + K(V - V_\mathrm{fl})] - I_\mathrm{sat}^+ \exp\left(\frac{(V - V_\mathrm{fl})}{kT_\mathrm{e}/e}\right), \tag{2.5}$$

where $K = \Delta I/\Delta V$ [A/V] denotes the slope of the non-saturating region. This method is practical, since it avoids calculating the sheath thickness. Even though the fitted value of K can be

inconsistent with exact theoretical sheath expansion rate, it can be shown that this approach brings substantial improvement and the results are consistent with more advanced techniques as a Child-Langmuir law based method or perimeter sheath expansion method [16].

2.3.2 Retarding field analyzer

Retarding Field Analyzer (RFA) is possibly the most successful diagnostic tool used for measurement of the ion temperature in the tokamak SOL. [17] [18] [19]. The basic principle is simple. By applying varying electric fields parallel to the magnetic field it slows down ions, which will or will not reach the collector.

It typically consists of a cavity with a set of two biasable grids as is shown on Fig. (2.1). Negatively biased small slit-shaped aperture admits ions to get inside the cavity, while electrons are repelled. Collector is located on the back side of the RFA opposing the slit. The current recorded by the collector depends on the voltage applied on one of the grids and the energy of ions. The RFA can operate in DC regime, however the proper selection of two repelling voltages makes the implementation complicated [18]. Even if sweeping of the applied voltage brings other difficulties, it is the most commonly used operation mode of the RFA. By sweeping the voltage applied on grid 1, only ions with sufficient energy are allowed to reach the collector and so the current-voltage characteristics can be obtained allowing to deduce the ion temperature. The *I-V* characteristics (see Fig. 2.2 a)) can be described by an analytical function [10]:

$$I_{\mathrm{col}} = I^{+}_{\mathrm{sat}}; (V < \Phi) \quad \text{and} \quad I_{\mathrm{col}} = I^{+}_{\mathrm{sat}} \exp\left(\frac{\Phi - V}{T_{\mathrm{i}}}\right); (V > \Phi) \tag{2.6}$$

The second grid is biased negatively in order to reflect any secondary electrons, caused by ions impacting on collector of the back of a slit.

Multiple approaches for RFA data analysis can be performed. Most commonly used technique (classical) is based on averaging the *I-V* characteristic after taking the natural logarithm of the collector current. Linear fit is performed in a suitable region (typically $5 < V_{\mathrm{G1}} < 50$V), where the *I-V* characteristics slope appears due to fractional repelling of the ions. The parameter T_{i}, describing the exponential decay of ion current, is obtained from the slope of the linear fit. The voltage range of $50 < V_{\mathrm{G1}} < 100$V is usually removed due to high noise level. However, the approach based on conditionally averaged plasma parameters can alone cause substantial errors in estimated T_{i}. The resulting ion energy distribution depends also on the choice of a fitting region (boundary conditions) as well as on a temporal resolution of the measurement, as was shown in [18]. If the boundary conditions are strictly set to $5 < V_{\mathrm{G1}} < 50$V, we ignore all I_{col} fluctuations and lower T_{i} are measured in comparison to boundary conditions set to follow the fluctuations. The reason for the existing discrepancy is the turbulent nature of scrape-off layer, which is studied with unprecedented temporal resolution in this thesis and than compared to the most recent RFA measurements.

The retarding field analyzer has two major disadvantages. The first is the physical size of the device (cylinder of 60 mm in diameter), which can have significant cooling effects on the SOL plasma. The second disadvantage is liming the ion temperature measurements to a few kHz, due to low effective current (in order of tens of μA) relative to the parasitic current significantly increasing with sweeping frequency. Complex electronics compensation stage has to be applied in order to subtract the stray currents and enable the measurement with as high sweeping frequency as 10 kHz [18]. The low signal-to-noise ratio and bulky construction of this device renders it difficult to deploy in small tokamak devices such as COMPASS. These disadvantages are far less severe when using a ball-pen probe for ion temperature measurement.

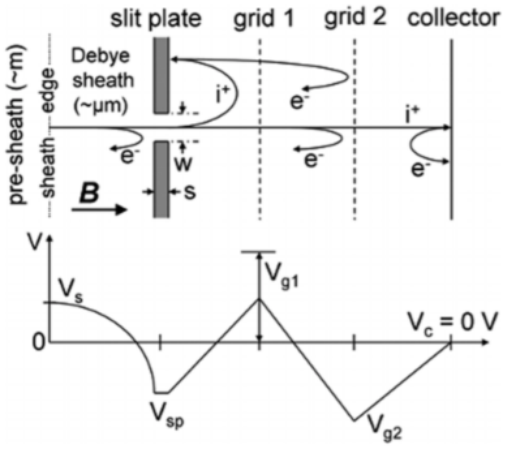

Figure 2.1: Top figure: a schematic of RFA in an ion analysis mode. Botom figure: the typical grid biasing. [17]

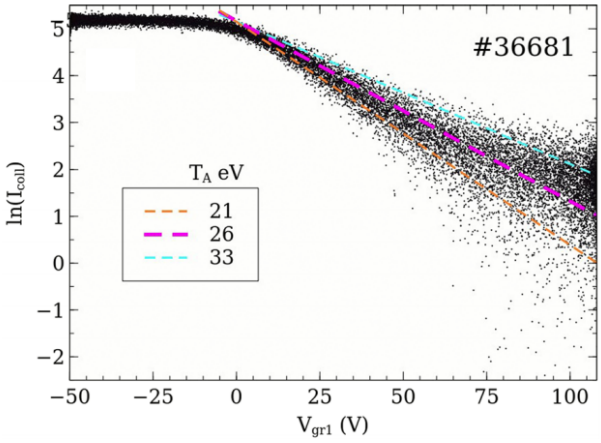

Figure 2.2: RFA voltage-current characteristic measured in ion analysis mode over 30 ms time interval. The measured characteristics is plotted on logarithmic scale. The black dots represent raw data. The resulting $T_i = 26$ eV, within the error bars 21-33 eV. The voltage value 0 V represents the plasma potential [10].

2.3.3 Ball-pen probe

The ball-Pen Probe (BPP) is an electric probe with it's construction similar to Katsumata probe. The key difference is that BPP has only one conductive part - stainless steel collector, which is embedded in ceramic (dielectric) tube. The basic principle of BPP is based on difference in Larmor gyration radius (see eq. 1.7) of electrons and ions in magnetized plasma. The shielding tube screens-off adjustable part of the electron current, while ions with larger gyration radius can still reach the collector. The shielding thus reduces the electron saturation current to approximately same amplitude of the ion saturation current. The scheme of ball-pen probe along with illustration of the basic principle of the electron shielding is shown on Fig.2.5.

The effect of $\vec{E} \times \vec{B}$ drift enables electrons to reach the collector and causes the electron current to be higher than the ion current. The drift is caused by the opposite direction of Larmor rotation of ions and electrons, resulting in electric field inside the tube in direction perpendicular to its axis (see Fig. 2.3). Electrons than reflect off the sheath formed along the tube, while being driven by $\vec{E} \times \vec{B}$ drift towards the collector (see Fig. 2.4). The potential on the tube internal wall decreases with depth, (becomes closer to Φ) which results in reduced electron current. Thus, due to weaker sheath potential less electrons are reflected by the sheath. The mechanism of particle transport inside the shielding tube was simulated and the effect of $\vec{E} \times \vec{B}$ drift confirmed by 3D PIC simulations [20].

The PIC simuations [20] show, that the ion transport inside the shielding tube is sensitive to the diameter of the probe. It was shown that, if the probe is too narrow the ions will not reach the collector before encountering the tunnel wall.

The collector depth is not an important consideration while the collector is recessed sufficiently for the electrons to be magnetically shielded form the collector. Sufficient retraction of collector h appears to be a few electron larmor radii, beyond which the electrons are magnetically shielded and the probe operates as BPP. If the collector is not sufficiently retracted or the strength of magnetic field is not sufficient the BPP operates as a simple Langmuir probe [20]. The electron saturation current and ion saturation currents are almost balanced when the collector is suficiently retracted

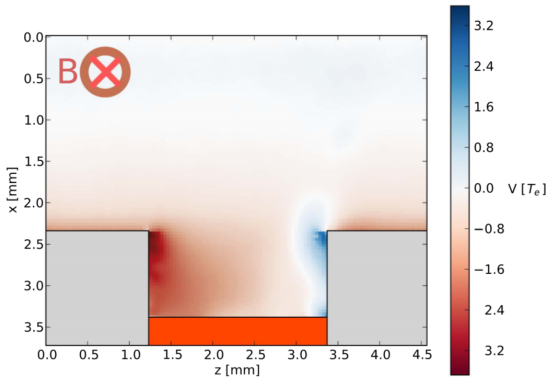

Figure 2.3: The cross-section of electric potential inside shielding tube, which in turn results in electric field in the z direction. Particles move along magnetic field lines, indicated in the upper left corner, into and out of the plane shown. Their gyration orbits can take them into contact with the walls resulting in the potential structure shown. [20]

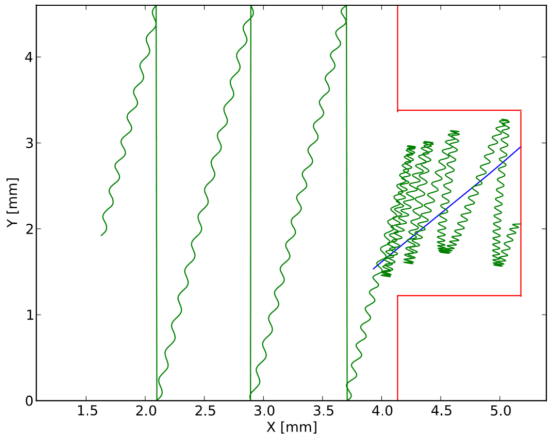

Figure 2.4: The electron trajectory (green) and ion trajectory (blue) inside a shielding tube (red) of BPP calculated using PIC simulation. The electrons follow magnetic field lines in a periodic simulation domain until entering the tube, where they oscillate due to reflections from wall sheaths. Ions with large gyro-radius simply travel down the tunnel [20].

inside the shielding tube. For example at COMPASS, for magnetic field $B_t = 1$ T the optimal colector depth is $h = -1$ mm [21].

Ball-pen probe was originally designed for direct plasma potential (Φ) measurement in magnetized plasma, where the BPP is placed perpendicular to the magnetic field lines. The floating potential of BPP is found near the plasma potential with a potential difference by a factor of $T_e \alpha_{BPP}$. Similarly to Langmuir probe we can obtain the local plasma potential using an equation

$$\Phi_{fl}^{BPP} = \Phi - \alpha_{BPP} T_e, \tag{2.7}$$

where T_e is the electron temperature in eV and Φ is the plasma potential and α_{BPP} is given as the ratio of electron saturation current to ion saturation current:

$$\alpha_{BPP} = \ln \left| \frac{I_{sat}^-}{I_{sat}^+} \right|, \tag{2.8}$$

where I_{sat}^- is the electron saturation current and I_{sat}^+ is the ion saturation current. Coefficient α_{BPP} attains a minimum and remains constant for a given experimental setup (working gas, probe size, collector depth) and was empirically found for deuterium plasma at the tokamak COMPASS and ASDEX-U as $\alpha_{BPP} = 0.6$ [15, 22, 14] and at tokamak CASTOR as $\alpha_{BPP} = 0.1$ [21]. Letting both Langmuir probe and ball-pen probe measure floating potential at the same time allows for uniquely fast direct measurement of electron temperature, assuming that the probes are calibrated and the coefficient α_{BPP} and α_{LP} are known. The calculation of electron temperature simplifies to a simple relation [15]:

$$T_e = \frac{\Phi_{fl}^{BPP} - V_{fl}^{LP}}{\alpha_{LP} - \alpha_{BPP}}, \tag{2.9}$$

where $\alpha_{LP} = 2.8$ and $\alpha_{BPP} = 0.6$ were found empirically and will be used in our measurements at tokamak COMPASS in further chapters.

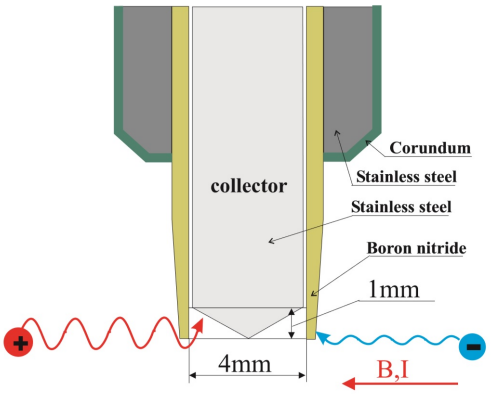

Figure 2.5: The scheme and basic principle of BPP used on tokamak CASTOR [23].

Chapter 3

Measurement on the tokamak COMPASS

3.1 Tokamak Compass

The tokamak COMPASS (COMPact ASSembly) belongs to the medium-sized tokamaks. It has geometry similar to the future ITER downscaled by a factor of ten. The diverted configuration allows for operation in the high-confinement mode (H-mode), which makes research on this tokamak ITER-relevant. The working gas used is deuterium. The basic engineering parameters are shown in the Table 3.1.

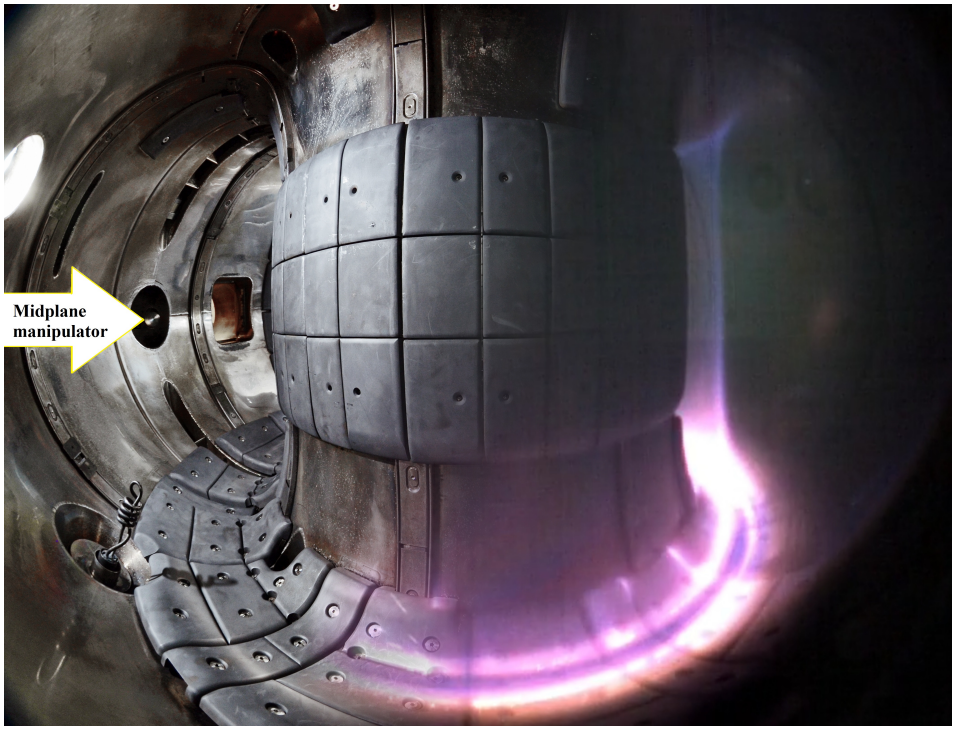

Figure 3.1: View of the tokamak COMPASS inside. Location of the midplane diagnostic port equipped with reciprocating manipulator is indicated. [24]

Major radius of vessel (R)	0.56 m
Minor radius of plasma (a)	0.23 m
Plasma current (I_P)	$<$ 400 kA
Magnetic field (B_T)	0.9 - 2.1 T
Elongation	1.8
Poloidal plasma shape	D
Pressure	10^{-6} Pa
Electron density (n_e)	3 - 9 $\times 10^{19}$ m^{-3}
Plasma duration	$\approx$ 1 s

Table 3.1: Basic engineering parameters of tokamak COMPASS, from [25].

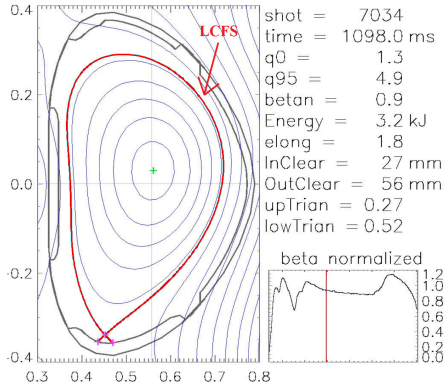

Table 3.2: The EFIT equilibrium reconstruction, with indicated position of the LCFS, from [26].

3.1.1 The Scrape-off layer

The Scrape-Off Layer (SOL) is the region with opened magnetic field lines. On the tokamak mid-plane, the anomalous perpendicular transport through SOL plays an important role. It is typically investigated using the electrostatic probes (Langmuir probe, retarding field analyzer, tunnel probe). Turbulence in SOL appears in form of density holes existing inside the separatrix and blobs moving outwards throughout SOL. Since it is expected that blobs and holes originate from the same process, these structures must be formed in the vicinity of separatrix [27, 28]. The amount of particles and energy transported by intermittent blobs or filaments through SOL is significant [29].

The understanding of the turbulence, in particular the blobs on the tokamak mid-plane is essential. However, ion dynamics is rarely measured or included in simulations, recently published results from HESEL code are already available, showing results on blob dynamics for high and low divertor collisionality [29] providing a good comparison for this thesis. Fast measurements are in general difficult to perform. Fast electron temperature measurements with a sampling rate of 1 μs are necessary to analyze the blob dynamics. Probe techniques capable of this resolution are the triple-probe, mirror-Langmuir probe and the combination of ball-pen with Langmuir, which was used in this thesis for direct measurement of the electron temperature with 1 μs resolution. The ion temperature is even more difficult to measure with high resolution. Recently published results using retarding field analyzer swept at $f = 10$ kHz show that fast measurements of ion temperatures and statistical methods are desirable for an adequate description of random fluctuations caused by such intermittent events as blobs [18]. However, precise measurement of blob ion temperature requires even higher sampling. In this thesis we present a probe technique capable of resolution of 10 μs and higher.

3.1.2 Experimental setup

Ball-pen and Langmuir probe head is installed on a midplane horizontal reciprocating manipulator (position indicated in Fig. 3.1) at the tokamak COMPASS and inserted into the scrape-off layer during L-mode discharges (see Fig. 3.2). The linear motion of the pneumatically driven manipulator is always perpendicular to the magnetic field lines when inserting the ball-pen probe into plasma. The maximum depth of insertion is approximately 60 mm. One reciprocation (in and out) takes approximately 170 ms. The probes were connected using standard coaxial cables. The BPP collector was swept between 0 V and +150 V with a sweeping frequency of 50 kHz. The electron

saturation current recorded by the BPP is in order of hundreds of mA, so the typical probe power amounts to a few tens of W. The data were collected using and acquisition system with a sampling frequency rate of $f = 5$ MHz. The probe head carrying ball-pen and Langmuir probes is shown in Fig. 3.3. The BPP stainless steel collector has a diameter of 2 mm and is retracted into the shielding tubes with inner diameter of 5 mm by $h = -1$ mm. The graphite proud Langmuir probes have 0.9 mm in diameter and protrude 1.5 mm into the plasma.

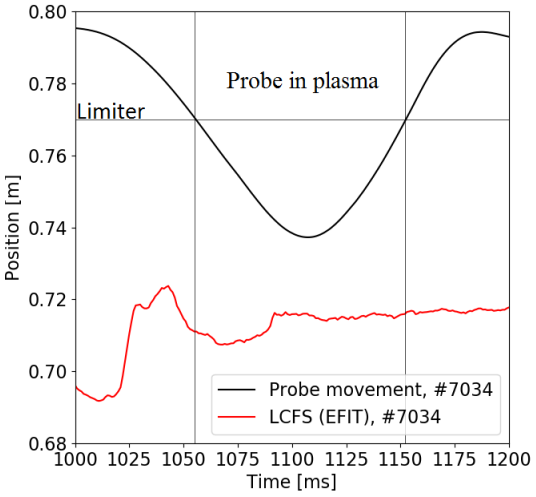

Figure 3.2: The motion of the probe head relative to the position of separatrix calculated using EFIT.

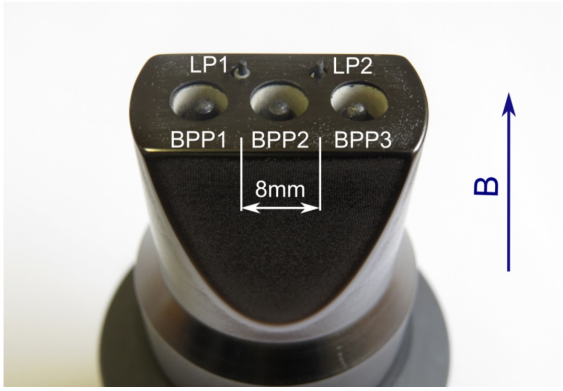

Figure 3.3: The probe head carrying three ball-pen and two Langmuir probes installed on COMPASS, from [23].

3.1.3 Electron temperature measurement using floating LP and BPP

The radial profiles of the LP and BPP floating potentials are plotted in Fig. 3.4. The gradient of the floating potential, of both the LP and the BPP, corresponds to the radial electric field. We observe that the $\Phi_{\mathrm{fl}}^{\mathrm{BPP}}$ is systematically higher than the $V_{\mathrm{fl}}^{\mathrm{LP}}$. The difference between potentials is caused by the suppressed influence of the electron temperature on the floating potential of the ball-pen probe. Thus, using the equation 2.9 we can also construct the radial profile of the electron temperature with 1 μs resolution, which is shown on the Fig. 3.5.

3.1.4 Estimation of the separatrix position

In order to compare different radial profiles obtained in the SOL of tokamak plasma, the probe head position is plotted with respect to the position of the LCFS. Typically the radial profiles are plotted with respect to the position of the LCFS. This approach allows to compare the measurements preformed during different discharges even on different devices. The position and size of the plasma is not constant, therefore the position of separatrix evolves and fluctuates throughout the discharge. Its position is routinely calculated by numerical equilibrium reconstruction using so-called EFIT code.

Another possibility of estimation of the separatrix position is through the probe diagnostics. In particular, from measurement of the radial profile of plasma potential using a BPP and a LP probe in a floating regime. The LCFS is characterized by the change of the poloidal plasma rotation

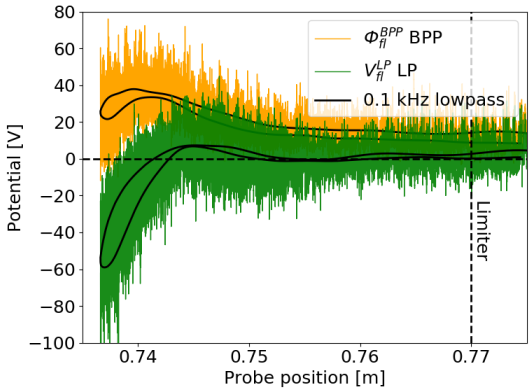

Figure 3.4: The radial profiles of the Langmuir (green) and ball-pen probe (orange) floating potentials in the scrape-off layer, #7034

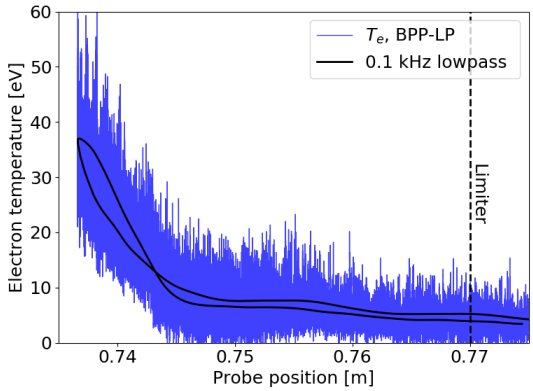

Figure 3.5: The radial profile of the resulting electron temperature, calculated using the relation (2.9) in the scrape-off layer, #7034

(plasma shear) as point where the poloidal rotation is equal to zero. The LCFS is located as a maximum of the plasma potential [27], where:

$$\vec{E}_{\mathrm{r}} = -\frac{\mathrm{d}\Phi}{\mathrm{dr}} = 0, \tag{3.1}$$

where $\vec{E}_{\mathrm{r}}$ is the vector of the radial electric field. This fact results in $\vec{E}_{\mathrm{r}} \times \vec{B}$ drift being restrained, thus the separatrix acts as a transport barrier increasing the plasma confinement.

It was shown that the absolute value of separatrix position obtained by EFIT reconstruction differs from the position obtained from probes by 2 - 3 cm. [30]. Thus, for the purpose of this thesis all radial profile measurements on tokamak COMPASS are plotted relatively to the position of separatrix obtained by probe technique which is assumed to be more precise as reported in [30]. However, the probe technique is not capable of measurement of the separatrix position fluctuations (only 2 instances of the probe crossing the separatrix can occour per discharge), which are precisely obtained by the EFIT reconstruction. For this reason at first we normalize the probe position with respect to the EFIT LCFS position (including fluctuations) and only after subtract the difference between the position obtained by the probe technique and EFIT reconstruction. This we introduce as R_{LCFS} in Fig 3.6. An example of this procedure applied for every discharge is shown in Fig. 3.6.

3.2 Ion temperature measurement using fast swept BPP

3.2.1 Signal preprocessing

Fast sweeping is often used for probe diagnostics and is always accompanied with a set of technical difficulties. If fast sweeping is applied, capacitance of a standard coaxial cable distorts the signal measured by the probe, due to the derivation effect. One also needs to account with the pickup signal created by cross-talk between diagnostic cables. In our experiment the coaxial cable used was RG-58/U with a parasitic capacity of 100 pFm^{-1}. Voltage from 0 to +150 V was applied on a Ball-pen probe at a frequency of 50 kHz, which gives rise to stray (capacitive) current $I_{\mathrm{stray}} \approx 25$ mA over a 10 m long coaxial cable.

A first step of the raw signal (ploted on Fig. 3.7 a) preprocessing is application of the lowpass filter. This step is performed in order to remove structures with much higher frequency than the

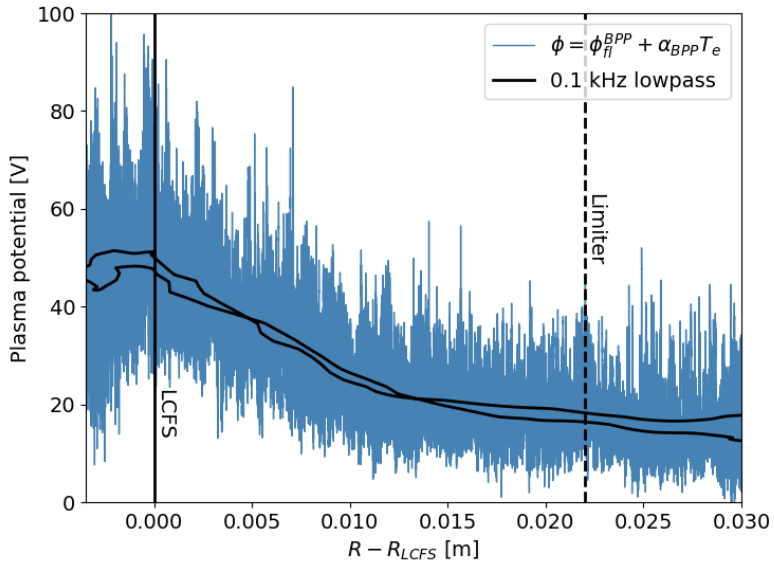

Figure 3.6: Example of the separatrix position estimation from maximum of the plasma potential. Shot: #7034

voltage sweeping frequency. The study of non-linear IV-characteristics with a sweeping frequency of 50 kHz requires that we measure also higher harmonics of this frequency. The Fourier transform of signal before and after the lowpass filter was applied is compared (shown on Fig. 3.7 b). We can see that the dominant frequency (sweeping frequency) of 50 kHz is clearly visible (above noise level) up to 7 harmonics. The upper bandwidth limit was thus set to 370 kHz, which allows to measure these 7 harmonics. The spectral analysis also shows that the signal with frequency lower than 7 harmonics is unaffected by the filter applied.

Next step before further processing of data is the stray current reconstruction and subtraction from the raw signal. We can model the stray current as a result of derivation of the voltage as:

$$I = C\frac{dV}{dt} + \text{offset}, \tag{3.2}$$

where V is the swept voltage applied on the probe. We can obtain the coupling constant C and offset of the raw signal from a linear fit of the current measured and the derivative of a voltage applied on probe, acquired before the insertion of the probe into plasma when we expect $I = 0$ A. The linear fit along with the stray current removal is shown on Fig. 3.7 c. The coupling constant calculated by the fit is $C = (1169 \pm 1$ pF) corresponding to the coaxial cable with a length of approximately 10 m. Thus, from the obtained coupling constant and the offset we can reconstruct the stray current and subtract it from the raw signal (see Fig. 3.7 d).

The final result of the signal preprocesing procedure is also shown on the of Fig. 3.7 d). The contribution of the capacitive to the total current is reduced roughly by a factor of 10.

After the preprocesing procedure individual I-V characteristics can be plotted for ramp-up and ramp-down half-periods divided into individual I-V characteristics. The division is done through locating the local maxima and minima of the applied voltage through second derivatives. Since the current is measured synchronously with the applied voltage, the division can be performed without any interpolation. Measurement of each I-V represents a measurement with (10 μs) period. The sampling frequency of 5 MHz provides approximately 50 data points per I-V that can be fitted by

equation (3.5). Therefore, sweeping with f = 50 kHz provides a measurement with a temporal resolution of 10 μs.

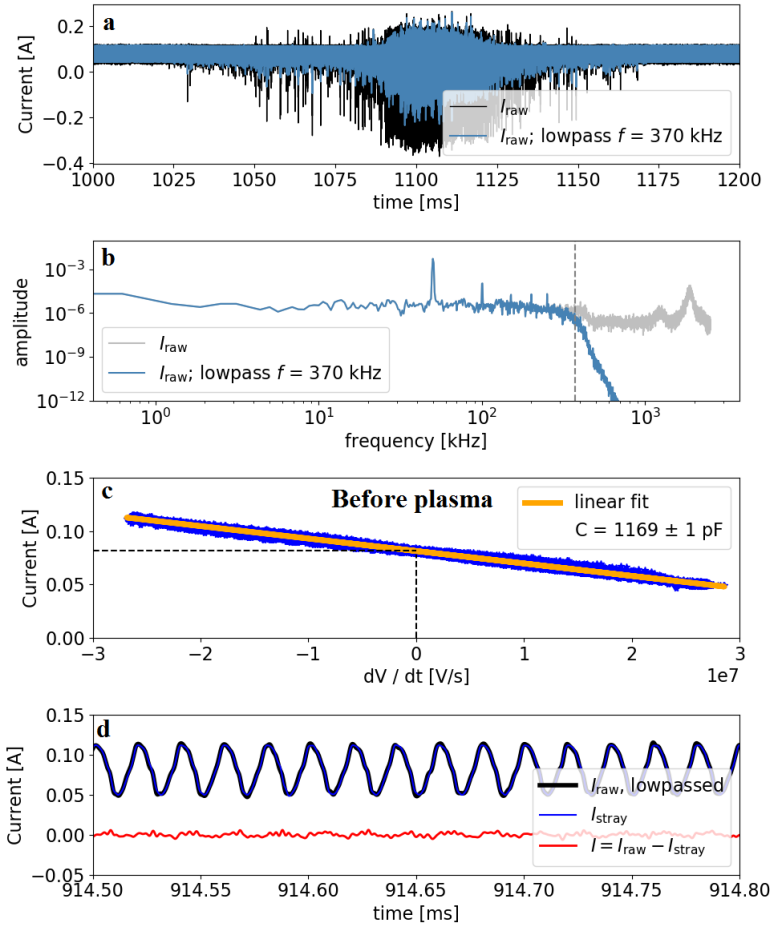

Figure 3.7: An example of the stray current reconstruction and removal. The figure a) shows an overview of the signal measured with swept BPP during the discharge (black) and the lowpassed signal (blue). The figure b) shows the Fourier transform of the signals. The figure c) shows the fit of a linear dependency between current measured and the first derivative of voltage applied. The figure d) is an enlarged interval before the discharge used to reconstruct the stray current. The final result of the cleaning is the red signal. Shot: #7034.

3.2.2 4-parameter fit of the ball-pen probe electron branch

The main purpose of this thesis is to further explore and confirm the possibility of ion temperature measurement using ball-pen probe during a discharge in a tokamak device. Basic diagnostic methods at tokamak COMPASS do not include routine measurements of the ion temperature. Only a limited number of measurements with retarding field analyzer were performed.

The main advantage of a ball-pen probe is its relatively high effective current (in order of 100 mA) [14], in comparison to the stray currents generated by high sweeping frequency in the coaxial cable. The probe can be swept at frequencies of 50 kHz or higher. The high sweeping frequency allows for measurement with a temporal resolution of 10 μs or higher. As it turns out, high temporal resolution is as important for T_i measurements as for measurements of all the other local plasma parameters (T_e, n_e, Φ). The reason for the necessity of high resolution both in time and space is the study of turbulent structures. The typical autocorrelation time of blobs observed on COMPASS is 10 - 20 μs. [31]. Recent measurements on ASDEX-U confirm that reaching higher sweeping frequencies ($>$ 10 kHz) is necessary for accurate reconstruction of the ion temperature histograms using a retarding field analyzer [18]. Due to limitation caused by high level of parasitic current and low effective signals (as discussed before) the sweeping of RFA with frequency higher than 10 kHz is currently impossible.

It will now be explained how to obtain the ion temperatures from the electron branch of the ball-pen probe *I-V* characteristics. The plasma potential, located in the inflection point of the *I-V* characteristics divides the *I-V* characteristic of a ball-pen probe into ion and electron branch. The electron branch can be measured by applying only positive swept voltage on the collector, above the plasma potential ($V > \Phi$). The electron branch of the *I-V* characteristic is the sum of an ion current, exponentially decaying with coefficient T_i, and an electron current, saturated or linearly increasing with the probe voltage. In order to subtract the non-constant (linear) portion of the electron current we introduce the 4th fitting parameter (K), which matches the slope of the non-saturating region. The same 4-parameter fitting approach is routinely applied to account for sheath expansion causing the non-saturating ion current measured by the Langmuir probe (eq. 2.5). However, in case of measurement of the electron branch the sheath expansion does not play a role (see chapter 2.4.4). This effect is not yet explained for BPP, but most probably is caused by the increase in $\vec{E} \times \vec{B}$ transport [20]. We assume than more electrons can reach the shielded collector due to an increase of the electric field when the applied voltage is increased.

The ion temperature T_i is determined from the exponential part of the electron branch using a 4-parameter formula given as:

$$I(V) = I_\mathrm{sat}^{-}[1 + K(V - \Phi)] - I_\mathrm{sat}^{+} \exp((\Phi - V)/T_\mathrm{i}). \tag{3.3}$$

Using the equation (2.8) we obtain:

$$I_\mathrm{sat}^{-} = \exp(\alpha_\mathrm{BPP}) I_\mathrm{sat}^{+}. \tag{3.4}$$

We can write:

$$I(V) = I_\mathrm{sat}^{+} \left(\exp(\alpha_\mathrm{BPP})[1 + K(V - \Phi)] - \exp((\Phi - V)/T_\mathrm{i}) \right), \tag{3.5}$$

where the fitting parameters obtained are ion temperature (T_i) in eV, plasma potential (Φ), ion saturation current (I_sat^{+}) and the linear increase of the electron current is described by slope (K). All the fittings use the least squares technique. Since the data points tend to fluctuate significantly more towards higher probe bias, we are using a weighted fit with the weighting factor of $1/\sigma$. σ is obtained as a standard deviation of the probe current fluctuation during $\pm$ 1 ms interval ($\pm$100

I-V characteristics) for each voltage interval (5 V). The obtained values of σ were then assigned to each data point of the central *I-V* characteristic accordingly.

However, the model described by the equation 3.5 is valid only for the electron branch given as $(V > \Phi)$. Therefore, the plasma potential Φ must be estimated beforehand. Typically the analysis of *I-V* characteristics involves locating the plasma potential as an inflection point (knee) using derivatives. This approach is well suitable for measurements with high number of samples per characteristic, in our case the requirement, due to very high sweeping frequency is not always met. Thus we perform a primary fit starting at BPP floating potential (where $I \approx 0$ A) which estimates the value of Φ. This parameter is than used to find the electron branch and to perform a secondary fit starting at the plasma potential $(V > \Phi)$. Tertiary fit can be also performed if the amplitude of a swept voltage is less than three times the T_i measured. In this case the linear increase of electron current does not affect the shape of *I-V* characteristic and we can set the parameter K to zero. An example of a 4-parameter fit starting at plasma potential is shown on Fig. 3.8 and 3.9.

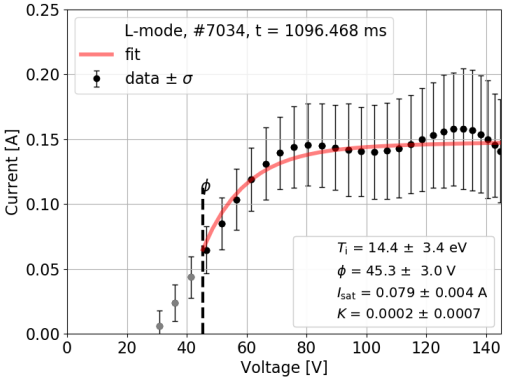

Figure 3.8: An example of a weighted fit starting at the plasma potential yielding low ion temperature, #7034.

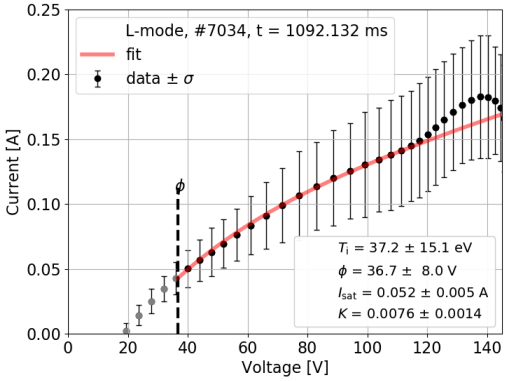

Figure 3.9: An example of a weighted fit starting at the plasma potential yielding high ion temperature, #7034.

3.3 Improved analysis

In this section I will discuss the further advancement of the previously described fitting routine greatly improving the number of successfully obtained fitting results. This technique is based on the assumption that the resulting ion temperature should not depend on the voltage sweeping amplitude. If so, than we can attempt to find such a voltage range, when the fitting results remain constant with change of voltage. Of course the amplitude of the voltage applied must be sufficiently high above the plasma potential in order to apply this technique, otherwise the results can be biased. Therefore a minimum voltage range requirement is set as $(V_{peak} - \Phi) \geq T_i$. Note, that during this interval, due to increase in repulsive potential the ion saturation current decays to e^{-1} of the original amplitude. We can formulate the main goals of the improved analysis technique as:

- The primary goal is to prove that the ion temperature obtained from exponential part of *I-V* characteristic within a fitting interval $(V_{peak} - \Phi) > T_i$ does not change with the increment of the voltage V_{peak} applied.
- Secondary goal of cut-off fitting technique is to obtain more relevant data from 4-parameter fits.

For example if we use an amplitude of swept voltage with $V_{\text{peak}} = 140$ V and the plasma potential $\Phi = 50$ V the highest ion temperature that we can obtain is 90 eV. Thus if we measure $T_{\text{i}} = 30$ eV, the resulting ion temperature should not depend on the peak or "cut-off" voltage if it is between 80 to 140 V. However, due to plasma turbulence with autocorrelation time in order of 10μs, parts of the measured *I-V* characteristics are typically deformed. If the deformation happens at the end of *I-V* characteristics and we perform the fit til the end it could converge to an mediate ion temperature with large uncertainty. This would lead to fit being discarded by the filtering criteria. This often observed phenomenon can be overcome by an cut-off refit procedure.

3.3.1 The cut-off fitting technique

We apply the cutoff fitting technique when the previously fitted *I-V* characteristics were rejected due to the filtering criteria mentioned before. This robust technique sequences the *I-V* characteristic into given amount of voltage intervals and performs the 4-parameter fit starting at a plasma potential until the cutoff voltage for each interval. The plasma potential is estimated by a single 4-parameter fit of the whole *I-V* characteristic, as was described in section 3.4. The voltage interval step is given by the sampling rate and an arbitrary multiplicative constant. Note that the skew of this particular approach (which appears if the swept voltage is a sine wave) is taken into account when we preform the numerical derivatives described below. For the purpose of this thesis we have chosen to perform a fit for each sample of the *I-V* characteristic. Of course, this is the most computationally demanding option. Other possibility is to perform a fit each two or three samples. We have tested and confirmed the independence of this parameter on the resulting distribution function of the ion temperature. The routine takes into account the fitting interval $(V_{\text{peak}} - \Phi) \geq T_{\text{i}}$ and does not converge if this criterion is not satisfied. The routine also needs to avoid taking into consideration the results which did not converge correctly during the 4-parameter fitting. All the results of individual fits are stored, while only the results which satisfy: $T_{\text{i,err}}/T_{\text{i}} > 0.6$ are passed to the numerical approximation of the derivative (forward difference), given as :

$$derivative = \frac{T_{\text{i}}[j+1] - T_{\text{i}}[j]}{V_{\text{cutoff}}[j+1] - V_{\text{cutoff}}[j]}. \tag{3.6}$$

The absolute value of derivative which is closest to 0 and satisfies a criterion $\left|\frac{\Delta T_{\text{i}}}{\Delta V_{\text{cutoff}}}\right| < 0.5$ is considered the plateau. The relative change of the resulting ion temperature was found as an optimal value from many observations. Future enhancement of the result selection subroutine could eliminate the need of such criterion. Since the numerical derivative can be calculated for either of the two following results (forward / backward difference) we can assume that the results of the two following fits are almost identical (within the margin set by the criterion). Thus, we have placed the derivative "in between" and we choose the fit with lower variance as the final result. An example of ball-pen probe *I-V* characteristic providing proof that the primary goal is achieved is shown on Fig. 3.10. It can be clearly seen that the ion temperature remains near constant with voltage applied.

Another example of the ball-pen probe *I-V* characteristic is providing proof that the secondary goal was achieved as well. As shown on Fig. 3.11 the *I-V* characteristic becomes deformed at around 140 V. The deformation is caused by a sudden decrease in local plasma density, which can be associated with blobs. Due to such an event this fit would be discarded by the filtering criteria. However, by cutting off the deformed part the fit converged successfully with a resulting $T_{\text{i}} = 26.3 \pm 1.1$ eV. The parameter K was set to zero, due to not enough voltage range (30 V) for the linear part to be fitted. It can also be seen that when the voltage range increases the K parameter is estimated by the 4-parameter fit and it does not affect the resulting temperature.

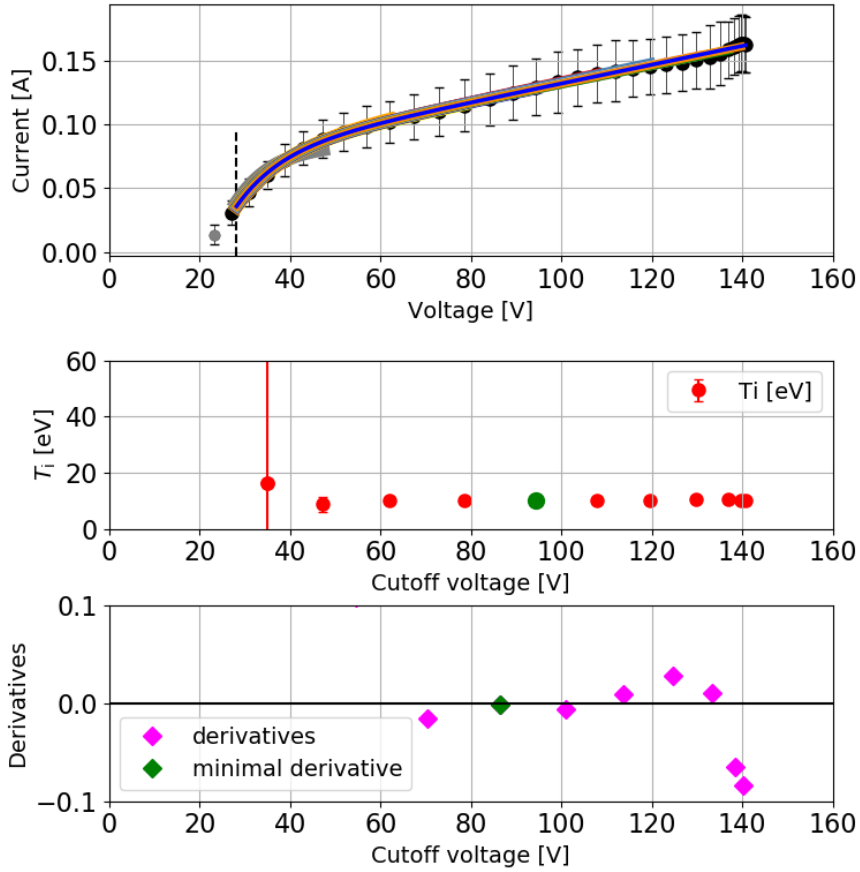

Figure 3.10: Top figure: An example of the ball-pen probe *I-V* characteristic fitted using the cut-off fitting technique. Middle figure: dependency of the estimated T_i on the cut-off voltage. Bottom figure shows the derivatives corresponding to the results plotted on the middle figure. Green color marks the resulting T_i chosen by the cutoff procedure. For clarity decreased cut-off voltage sampling was used. Shot: #7034.

It is important to note that the typical blob autocorrelation time (10 -20 μs) is very close to the temporal resolution of the swept BPP resulting in most of the *I-V* characteristics deformed as the fast T_i change takes place during measurement of one *I-V* characteristic. Such deformed *I-V* characteristics typically results in relative error of the fit exceeding 60 %. These *I-V* characteristics are then attempted to fit again using the cut-off technique. The cut-off technique has increased the number of obtained fits passing the filtering criteria from 30% to more than 50% of all possible fits. However, the temporal resolution of 10 μs is still not high enough in order to capture all the blob events. If a low to high temperature transition appears during measurement of a single *I-V* characteristics the cut-off procedure will most probably converge to the low temperature, since the sudden disruption will produce non-constant T_i. Therefore the gain of the background T_i may be higher than gain of the blob T_i.

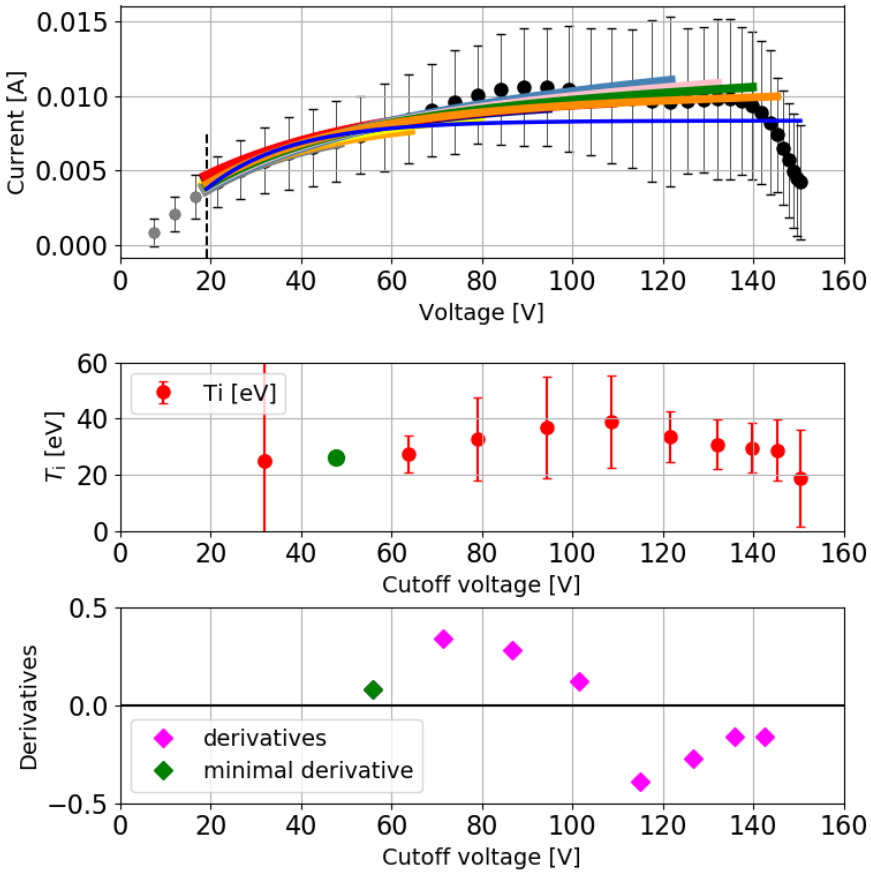

Figure 3.11: Top figure: An example of the ball-pen probe *I-V* characteristic fitted using the cut-off fitting technique. Middle figure: dependency of the estimated T_i on the cut-off voltage. Bottom figure shows the derivatives corresponding to the results plotted on the middle figure. Green color marks the resulting T_i chosen by the cutoff procedure. For clarity decreased cut-off voltage sampling was used, Shot: #7034.

3.4 Results of measurements on COMPASS

In this section all results from cut-off fitting procedure preformed during L-mode discharge #7034 will be discussed and compared to to the results of a complementary discharge #7029, published in [34]. As shown on Fig. 3.12, both discharges have similar macroscopic plasma parameters which allows us to reproduce and compare the results. The measurement was performed during the flat-top phase, when the discharge parameters (B_T = 1.15 T, I_P = 170 kA, $n_e = 5 \times 10^{19}$ m $^{-3}$) are held constant.

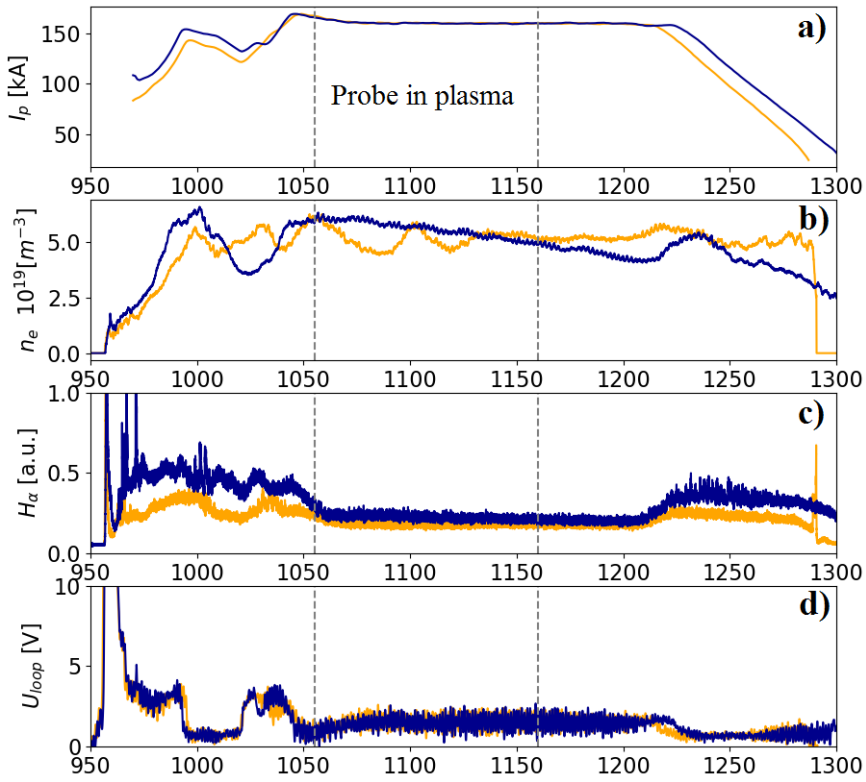

Figure 3.12: Comparison of time evolution of macroscopic plasma parameters during discharges #7029 (yellow line) and #7034 (blue line). a) plasma current, b) the line-average density, c) H_α signal, d) loop voltage

The plasma current

The plasma current shown on Fig. 3.12 a) is measured by Rogowski coil poloidally wrapped around the vacuum chamber of tokamak device and estimated from induced poloidal magnetic field B_p using Ampere's law:

$$\oint_l \vec{B}\,d\vec{l} = \mu I, \tag{3.7}$$

where I is the induced current and μ is the magnetic permeability of the medium. From the magnetic flux ϕ through Rogowski coil given as:

$$\phi = NA\mu I, \tag{3.8}$$

where A is the cross-sectional area and N is the number of wire turns. The output voltage V_{coil} is

$$V_{coil} = \dot{\phi} = NA\mu\dot{I}. \tag{3.9}$$

Thus, the voltage measured by the Rogowski coil is proportional to the derivative of the plasma current with respect to time. Using analog integrator we can obtain the plasma current. This measurement allows us to locate the flat-top phase of the discharge and compare the discharges.

The line-average density

The plasma line-average density shown on Fig. 3.12 b) is measured by a microwave interferometer. This technique is based on phase shift measurement between the electromagnetic waves passing through volume of plasma and a reference. The integral value of a phase shift is proportional to the electron density along the beam chord [32].

The visible light emission

The H_α measurement shown on Fig. 3.12 c) represents the intensity of the spectral line emitted by impurities through black body radiation. This measurement allows us to compare the impurity content in plasma during different discharges.

The loop voltage measurement

The U_{loop} measurement shown on Fig. 3.12 d) is the voltage induced by a single loop of wire along the torus (toroidal direction) given as:

$$U_{\text{loop}} = -\frac{d\psi}{dt}, \tag{3.10}$$

where ψ is the magnetic flux through transformer core. The loop voltage relates to the resistivity of the plasma $R_{\text{p}} = \frac{U_{\text{loop}}}{I_{\text{p}}}$ and inductance, which can be neglected during flat-top phase of the discharge. Since with increasing impurity content the plasma resistivity increases the loop voltage is also proportional to the impurity content. The ohmic heating power can be estimated as: $P_{\text{OH}} = U_{\text{loop}} \cdot I_{\text{p}}$.

3.4.1 Temporal evolution of plasma potential obtained with 10 μs resolution

The plasma potential is simultaneously measured by an independent technique using BPP1 and LP1 (shown on Fig. 3.3). These probes are both in a floating regime, thus using relation 2.9 we can obtain the electron temperature with a uniquely high temporal resolution (1 μs). Using the equation 2.7 we can calculate the plasma potential with the same resolution. Since the all probes are located on the same probe head we can compare these results with the plasma potential measured by the swept BPP3. The results of the two techniques are matching and we can assume that the probe is well calibrated and fitting is set-up correctly. However, we need to take into account that the probes are at slightly different positions in the poloidal direction (8 mm). Thus, simultaneous measurements are not necessarily synchronous. An example of such comparison is shown on Fig. 3.13, where the plasma potential obtained from fits (red circles) was filtered with a criterion of maximum relative error not exceeding 60%.

3.4.2 The radial profile of the ion temperature

In order to construct the radial profile of the ion temperature we will use the probe head position relative to the position of the LCFS as was described in the section (3.1.4). The Fig. 3.14 shows the electron temperature obtained using equation 2.9 with temporal resolution of 1 μs and the ion

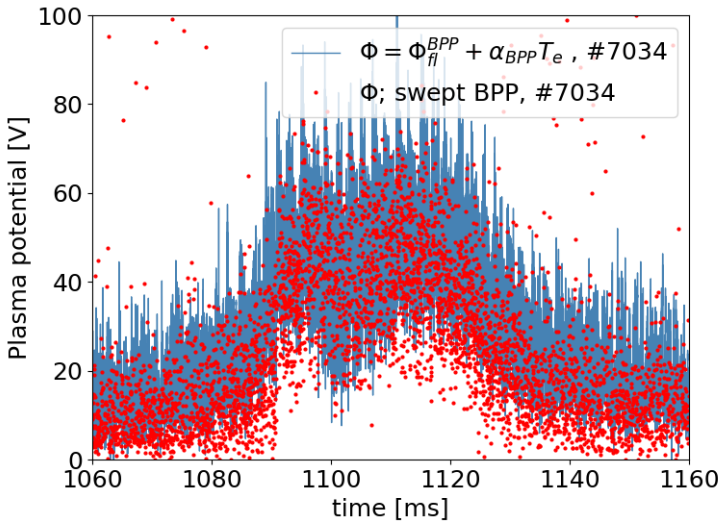

Figure 3.13: Comparison of the plasma potential estimated from 4-parameter fit (red circles) to the direct measurement of the plasma potential during the same discharge. Shot: #7034

temperature measured with a temporal resolution of 10 μs. Since the T_i is obtained by a fitting routine filtering criteria for the fit quality must be placed. We have set filtering criteria as follows:

$$T_{\mathrm{i,err}}/T_\mathrm{i} < 0.6,$$

$$\Phi_{,\mathrm{err}}/\Phi < 0.6,$$

$$T_\mathrm{i} < (V_\mathrm{peak} - \Phi)/1,$$

where $V_\mathrm{peak} = 150$ V is the peak value of voltage applied on the BPP. The last criterion is a technical limitation of technique set by the chosen amplitude of the applied voltage. Only the ion temperatures, passed these filtering criteria are plotted in the Fig. 3.14. From the radial profile we can see that the fast measurements reveal T_i fluctuations, highly exceeding the T_e fluctuations, shown with the same temporal resolution. This can be caused by stronger damping of the electron temperatures in the SOL. Using fast swept RFA in [33] it was confirmed that although electrons deposit their energy closer to the strike point, ions can travel much further with their energy to regions which aren't expecting any heat loads.

The very low temperatures ($T_\mathrm{i} < 5$ eV) observed throughout the entire SOL can be also caused by impurity content, which can lead to temperature underestimation, as was shown by simulating the RFA measurements in impure plasma [17].

A comparison between the resulting radial profile obtained using the technique recently published in [34] shown on top in Fig. 3.14 and the improved cut-off technique is shown on the bottom in Fig. 3.14. The results plotted in both figures were filtered by the filtering criteria stated above. The number of successfully fitted values in Fig. 3.14 represent roughly 2500 fits, which corresponds to 30 % of the available fits, while the results of the improved analysis represent roughly 5000 fits, which corresponds to approximately 60 % of the available fits.

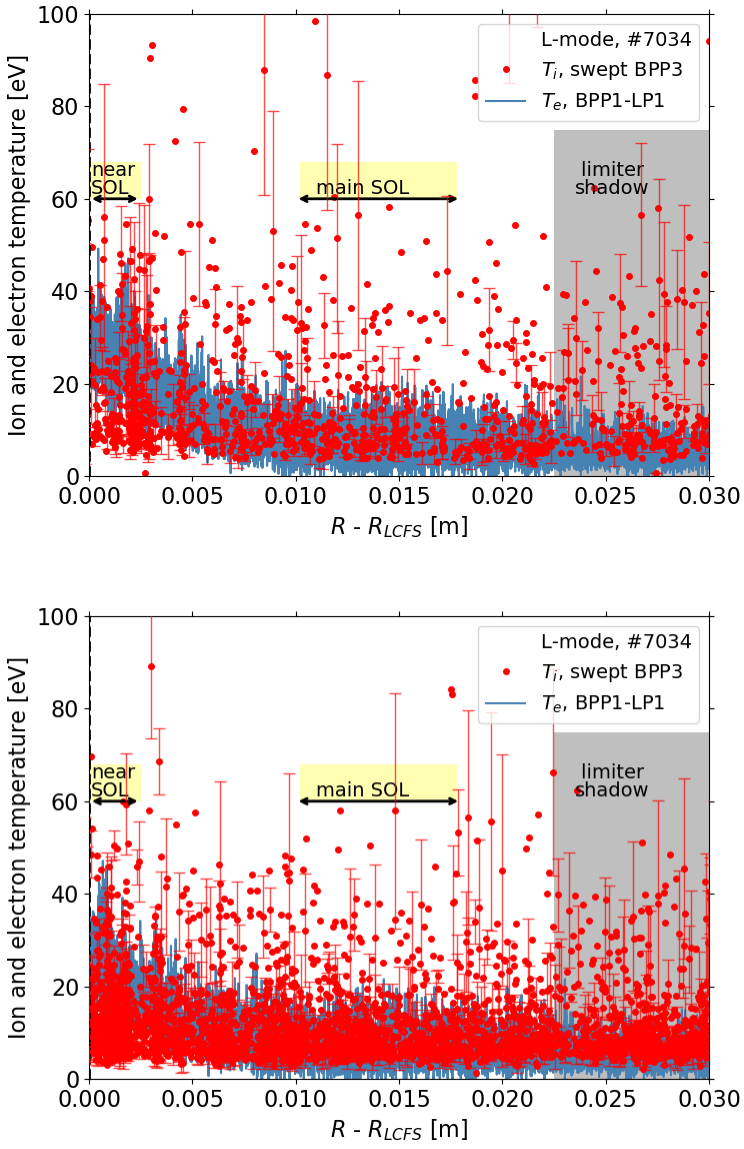

Figure 3.14: The radial profile of T_i and T_e. Top figure shows the results obtained using the same approach as in [34]. Bottom figure shows the results obtained with improved analysis. Radial profiles correspond to the same discharge #7034, using the same filtering criteria. The absolute error bars are only shown for a few points.

3.4.3 The temporal evolution of the plasma parameters

Particles and thus energy are mostly transported throughout SOL by intermittent filamentary structures (blobs). Thus, in the low-confinement modes the plasma parameters in the tokamak SOL tend to fluctuate with time. The scrape-off layer is at the same time a region near vessel walls with no external heating. One can thus expect that particles of two populations with different energies will be present. One of a "background" low temperature plasma and the other of a hot blobs undergoing an anomalous perpendicular transport from the core plasma, as shown on Fig. 3.15. Indeed this exact behavior was predicted by numerical simulations using HESEL (hot edge-sol-electrostatic) model for L-mode plasma at the mid-plane of medium sized tokamaks [29].

On the Fig. 3.15 we can see the comparison of all the measured plasma parameters evolution during 1 ms interval in the main SOL and near SOL. We can observe that the background ion temperature is present in both regions and intermittently perturbed by hot blobs. Note that the measurement of the T_i and T_e is displaced by roughly 8 mm in the poloidal direction.

The fluctuations of the ion saturation current are expected to be dominated by the electron density fluctuations [27]. Therefore, I_{sat} can be used as a measure of electron density fluctuations. The electric potential variation is expected to follow density and temperature variations [29].

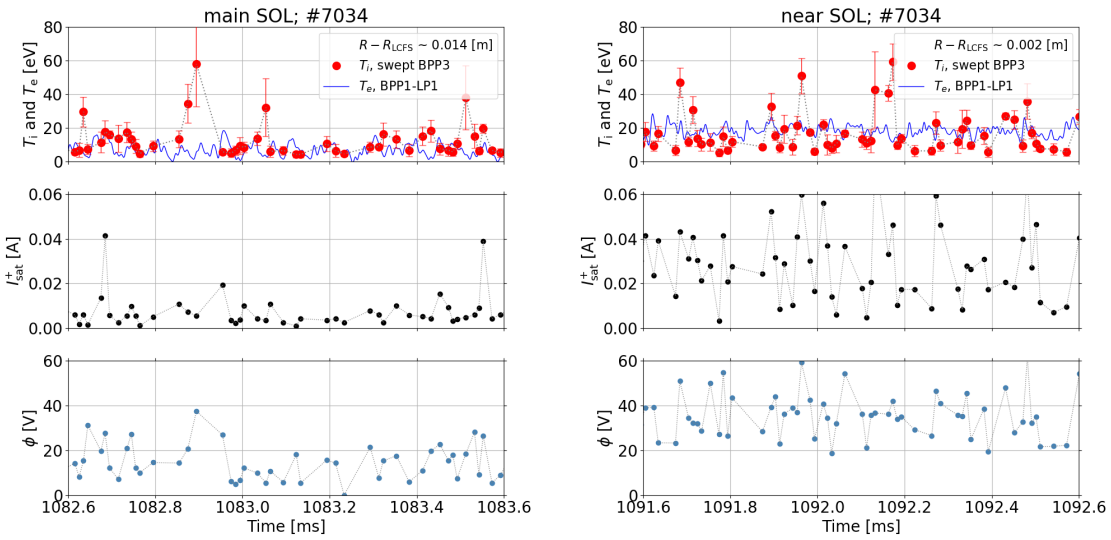

Figure 3.15: An example of temporal evolution of the plasma parameters from 1 ms interval in main SOL (left) and near SOL (right). Ion and electron temperature evolution is shown on the top figure, ion saturation current middle and plasma potential on the bottom figure, obtained using the cut-off refit technique.

A correlation was found between I_{sat}^+ and Φ, as is shown on Fig. 3.16.

3.4.4 Statistical evaluation of the results with 10 μs resolution

Temperature histograms

The fast ion temperature measurement yields thousands of scattered results, thus a statistical evaluation in form of histograms is needed. Since the two discharges #7034 and #7029 are complementary (see Fig. 3.12) we can merge the results from the same radial positions into the same histograms. The resulting T_i and T_e histograms fro the main SOL ($0.01 < R - R_{LCFS}\,[\mathrm{m}] < 0.018$) and near SOL ($0.0 < R - R_{LCFS}\,[\mathrm{m}] < 0.002$) regions are shown in Figure 3.17.

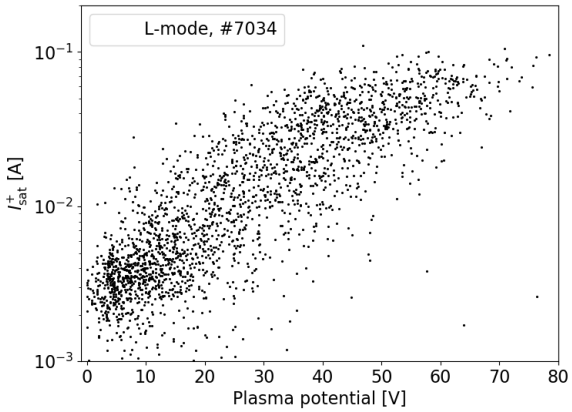

Figure 3.16: Dependency of I_{sat}^{+} as a function of Φ plotted in logarithmic scale, Shot: #7034.

The resulting histograms show non-Gaussian ion temperature distribution in the SOL. The histograms from both regions have a maximum at low energies (10 eV), that can be attributed to the background plasma and influenced by the impurity content (as discussed in the section 3.4.2) and a hot-tail extending to energies up to 60 eV in the near SOL and 40 eV in the main SOL, which is can be attributed to the blobs.

It is important to note that the overall shape of the histograms both in the near and main SOL does not change significantly with and without the cut-off refit procedure (see appendix A, Fig. 5). We can thus conclude that the cut-off procedure operates as expected, yielding results with the same distribution as was previously observed in [34].

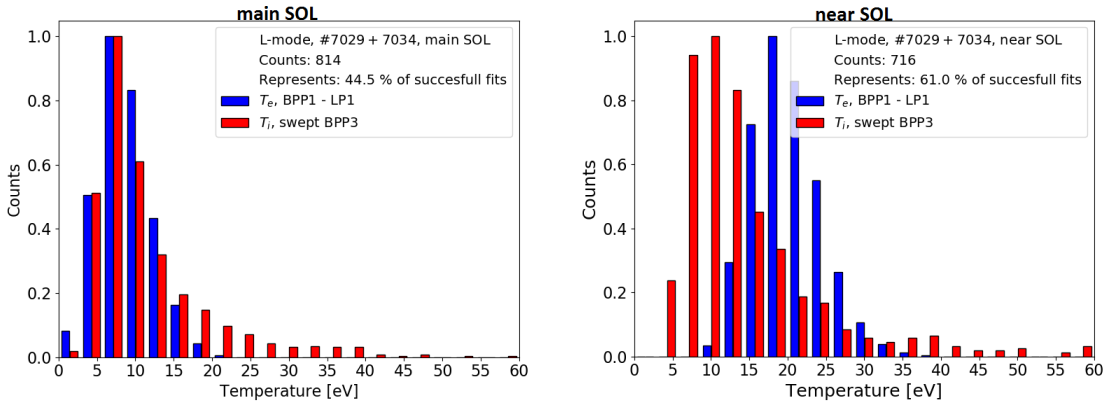

Figure 3.17: Temperature histograms of fast ion temperature measurements in chosen regions of the SOL (regions indicated in Fig. 3.14)

Radial profiles of ion temperature fluctuations

It was confirmed experimentally and by numerical simulations, that the electron density and electron temperature fluctuations in the SOL are caused by the blobs passing through the probes, with poloidal velocity of 10 mm/5 μs [35, 29]. Thus, the temperature and density spread through the SOL with the same velocity, although the density has wider spacial dimensions. An example of the

typical turbulent behavior of T_i, T_e, Φ and I_{sat} was shown at two radial positions in the SOL during L-mode discharge (see Fig. 3.15).

It is often observed, that fluctuations (n_e, T_e) follow Gamma-distributed statistics, where clustering of events is fundamental, given as: [36].

$$P(n_e) = \frac{A^2}{\langle n_e \rangle \Gamma(A^2)} \left(\frac{A^2 n_e}{\langle n_e \rangle} \right)^{A^2-1} \exp\left(- \frac{A^2 n_e}{\langle n_e \rangle} \right). \tag{3.11}$$

Based on the HESEL models [29], used for numerical simulations of blob ion dynamics, we can expect the ion temperatures to follow the Gamma distribution. If our measurements indeed follow the Gamma distribution then the skewness (S) should be related to mean (μ) and standard deviation (σ) as follows:

$$S = \frac{2}{A}, \quad \text{where} \quad A \equiv \frac{\mu}{\sigma} \tag{3.12}$$

We can also include the comparison to Log-normal distribution, in which case the Log-normal skewness is defined as follows [36]:

$$S = \frac{3}{A} + A^{-3} \tag{3.13}$$

It was shown, that density fluctuations observed in the vicinity of separatrix are weak compared to regions in main SOL [36]. We can expect the same behavior of T_i fluctuations, however this was never experimentally confirmed. In order to quantify this observation we can calculate the parameter A, characterizing the size of fluctuations relative to the mean value. The parameter $A \gg 1$ would correspond to relatively weak fluctuations while $A \approx 1$ indicates the presence of intermittent bursts. A radial profile of A and S, where $\mu \equiv \langle T_i \rangle$ and $\sigma^2 = \langle (T_i - \mu)^2 \rangle$ was created. The statistical analysis is performed from 3 ms long time intervals, which are large enough for reduction of statistical noise, while the spacial resolution remains sufficient. The results from a single discharge are plotted in Fig. 3.18. The A and S are compared for T_i and T_e measurements. However, from the T_i fluctuation measurements the region inside LCFS was excluded, due to possible influence of technique limitation.

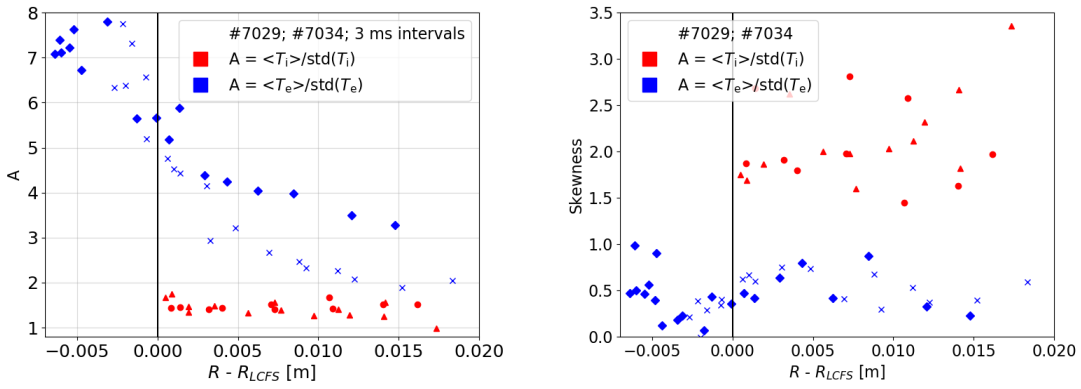

Figure 3.18: Radial profiles of cluster parameter A (left) and skewness (right) with respect to the LCFS. Two complementary discharges are plotted #7029 (triangles and diamonds) and #7034 (circles and crosses).

The general decreasing trend of the parameter A shows an increase in clustering with a distance from LCFS (shown on Fig. 3.18), which means that the plasma is less turbulent inside the LCFS. The parameter A obtained for the electron temperature fluctuations well complies with Fig. 3

in [36]. As for the ion temperature fluctuations the decrease parameter A is observed, although on much smaller scale. The parameter A calculated from T_e is systematically higher than from T_i, which can indicate that the T_e fluctuations are strongly damped in the SOL comparing to the T_i fluctuations, transported far into SOL. This exact behavior, corresponding to electrons being transported toward divertor faster than ions, was predicted by all the models of turbulence in SOL [37]. Until now this was not measured, since the experimental studies of the ion temperature fluctuations require extremely high temporal resolution. From the right-hand side graph of the Fig. 3.18 we can observe that the T_i distribution is highly positively skewed throughout the entire SOL, while the T_e is between 0.5 and 1 which represents a moderate positive skew.

Analysis of the fluctuations in the entire SOL (shown in Fig. 3.19) shows that the ion and electron temperature distribution conforms to the Gamma distribution. A simple stochastic model of SOL mathematically predicts that fluctuations should indeed follow the Gamma distribution [38]. The Gamma distribution of fluctuations in SOL can be mathematically derived from simple stochastic model in [38]. Bigger statistical sample, possibly achieved by measurements with a stationary probe, is required for precise experimental proof of the predicted Gamma distribution (Fig. 8 in [39]).

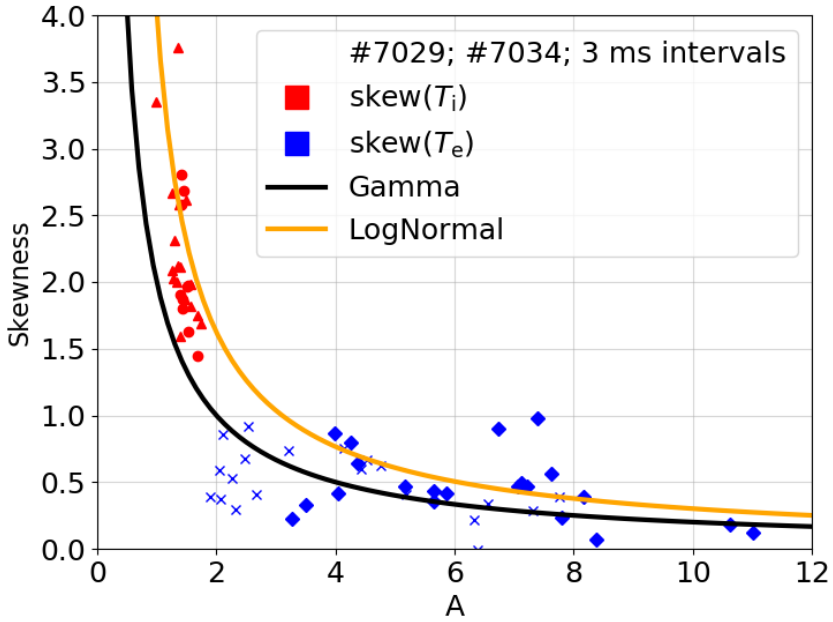

Figure 3.19: Variation of S as a function of A and comparison with the Gamma Eq. (3.12) and Log-normal Eq. (3.13) distributions. Two complementary discharges are plotted #7029 (triangles and diamonds) and #7034 (circles and crosses).

Yet another prediction of the stochastic modeling [38] is a parabolic relation between skewness and kurtosis K given as (eq. (16) in [39]):

$$K = \frac{3S^2}{2}. \tag{3.14}$$

This model is in agreement with many experimental studies of plasma fluctuations and also turbulence simulations based on interchange motions. It explains many experimental findings such as:

broad plasma profiles and large fluctuation levels, skewed and flattened amplitude probability distribution functions, and a parabolic relation between the skewness and kurtosis moments. [38]. The results shown in Fig. 3.20 are in agreement with the stochastic model for intermittent fluctuations in the plasma SOL, as well as, the experimental results obtained form electron density fluctuations shown in Fig. 20 in [39] or in [40]. The ion temperature fluctuations can thus be also explained by a stochastic model in a low confinement mode.

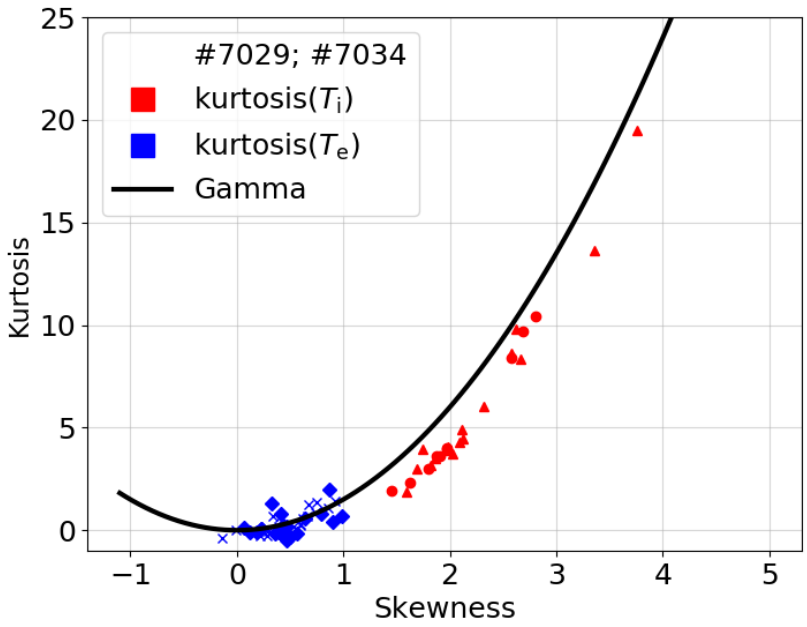

Figure 3.20: Kurtosis as a function of skewness and comparison with the Gamma Eq.(3.14) distribution. Two complementary discharges are plotted #7029 (triangles and diamonds) and #7034 (circles and crosses).

3.5 Ion temperature obtained from RFA-like *I-V* characteristics

The purpose of this approach is to show an averaged radial profile of the ion temperature, similar to a slow swept retarding field analyzer [18]. The technique of ion temperature measurement using the RFA was in detail discussed in the chapter 2.4.2. Here we present a novel approach of emulating the RFA *I-V* characteristics using a fast swept ball-pen probe.

Since the Ion temperatures measured with a high temporal resolution (10 μs) are found not to be normally distributed, we can not simply assign a mean and a standard deviation to the measured data in order to construct averaged temperature radial profile. We must use a more complex approach similar to analysis of data from a Retarding Field Analyser (RFA). To create an artificial RFA-like *I-V* characteristics we input the values of parameters T_i, ϕ, and I_sat^+ estimated by the 4-parameter fit. The parameter V is generated as an array ranging between 0 to 200 V with a sampling of 1 V. The current below the plasma potential is set to $I = I_\mathrm{sat}^+$, since the real retarding field analyzer does not measure the electron current (electrons are being repelled by the negatively biassed entry slit). The "artificial" RFA collector current I is than calculated using the equation describing an exponential decay of the ion current with coefficient T_i given as:

$$I = I_\mathrm{sat}^+ \exp\left(\frac{\phi - V}{T_\mathrm{i}}\right), \text{ where } (V > \phi) \tag{3.15}$$

Example of such artificial *I-V* characteristics and two fitting approaches are shown on Figure 3.21.

There are more possibilities or approaches of obtaining the ion temperature parameter from fitting of the RFA *I-V* characteristics. The differences in the results obtained by different fitting approaches were discussed in [18], where for the first time the RFA was used for T_i measurements with high temporal resolution. Very similar behavior was observed when fitting the artificial *I-V* characteristics and will be discussed in more detail in the next section.

3.5.1 Fitting of the synthetic RFA-like *I-V* characteristics

The classical analysis of the RFA current-voltage characteristics is based on conditional averaging (or mean) of the collector signal. All the RFA-like results in this thesis are based on this approach. We take the natural logarithm of the current I emulated using the eq. (3.15) and resulting plasma parameters obtained by the swept BPP. The average *I-V* characteristic is constructed by numerically averaging current vs. voltage obtained from a 3 ms time interval with a binning interval of 1 V. The resulting average *I-V* characteristic is plotted on Fig. 3.21 as a blue curve. The so-called knee of RFA *I-V* characteristic is clearly observed at the plasma potential. The plasma potential (measured by swept BPP) is indicated by black points and the average value of the plasma potential (from the 3 ms interval) is shown as a dashed vertical line. This technique gives very similar *I-V* characteristics in comparison to the real RFA. Indeed the measurements with fast-swept RFA show, that the collector current PDF is not symmetric, but rather follows Gamma-like shape [18].

Boundary conditions must be placed when performing a fit. The resulting T_i values are impacted by the chosen boundary conditions. It was shown in [18] that the conditions must be set to follow the plasma fluctuations in order to obtain realistic ion temperatures. The benefit of fast sweeping is that the plasma fluctuations can be resolved in more detail. By setting the boundary conditions as $5 < V < 50$ V and $I > 0$ A we would effectively ignore the fluctuations. Therefore, we compute the ion temperature from the *I-V* region bounded by $0 < I < e^{-1} I_\mathrm{sat}^-$ [17]. Since the change of ion saturation current is proportional to the change in plasma density, the fluctuations in plasma density are characteristic for the filamentary structures (blobs). The fitting of the "high energy" part of the collector signal (less affected by the impurity ions) is recommended in [17], in order to avoid the underestimating of the resulting T_i due to impurity content.

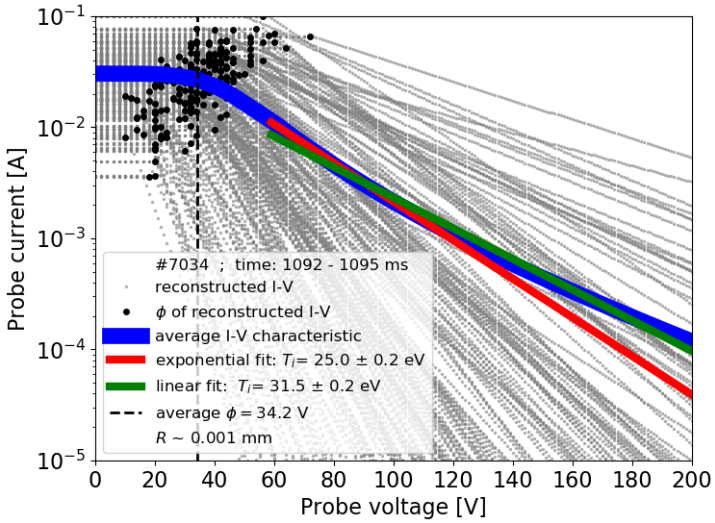

Figure 3.21: An example of the RFA-like *I-V* characteristic, emulated from fast (10 μs) T_i, I_{sat}^{+} and Φ measurement using swept BPP. The averaged RFA-like *I-V* shown in blue is fitted by equation 3.15 using least-square minimization. Shot: #7034.

A single ion temperature is obtained from a linear fit of the logarithmic slope of the averaged *I-V* characteristic. Also an exponential fit (according to eq. 3.21) of the averaged *I-V* characteristic in linear scale is performed and plotted in logarithmic scale for comparison. The difference in the resulting ion temperature from linear and exponential fit is caused by the fact that the exponential fit performed in linear scale is less sensitive to the high temperatures linked to the blobs and, hence, the calculated T_i is systematically lower. In order to compare the results to measurements with slow-swept RFA we have chosen linear fit which is the most commonly used approach. The linear fit is taking into account the high temperature blobs, which have significant impact on the profiles.

3.5.2 Ion temperature radial profile from RFA-like *I-V* characteristics

In this section we show the resulting radial profiles with artificially decreased temporal resolution (3 ms) so to match the resolution of slow swept retarding field analyzer. The profiles are created based on fitting the synthetic RFA-like *I-V* characteristics as described in the previous section, based on results from fast measurements with and without the cut-off refit procedure. Measurement was preformed in two identical L-mode discharges, both with medium electron density ($n_e = 5 \times 10^{19}$ m^{-3}) and plasma current during flat-top phase $I_p = 170$ kA.

Note that the low ion temperatures are no longer present in the radial profile shown on Fig. 3.22. Their absence is due to the fitting taking into account only the tail of the blob dominated *I-V* characteristics as was shown in [29]. The low ion temperatures, typically characterized by low plasma potential, are effectively neglected whether by fitting the RFA-like of the RFA *I-V* characteristic. Thus, the clear trend in radial profiles typically observed by RFA is reproduced. However, recent measurements with fast swept (10 kHz) RFA also indicate the possibility of a presence of the low-temperature background plasma and intermittent hot blobs [18].

The resulting radial profile shows that the ion temperature is systematically higher than the electron temperature throughout the entire SOL. It is clearly visible that the T_e decreases with radius faster than T_i, which is consistent with faster perpendicular energy losses of electrons in the

SOL. It indicates larger radial transport of of ion heat in the edge comparing to the electron heat. Ion-to-electron temperature ratio was found as 3-4 in the main SOL and 1-2 in vicinity of separatrix. This result agrees with experimental results performed using RFA and the theoretical expectations [41]. It is still often assumed for calculations that $T_i = T_e$ in the scrape-off layer. This assumption of thermal equilibrium can be true only for strong ion-electron thermal coupling, typically achieved during discharges with high plasma densities [41]. These conditions were not achieved during this experimental session and the resulting ion-to-electron temperature ratios conforms with the expected values for this discharge regime.

The complementary radial profiles of the two identical discharges (#7029 and #7034) indicate very good reproducibility of the results. If we extrapolate the ion temperature profiles inside the LCFS it is clearly visible that the ion-to-electron ratio would decrease to unity, indicating expected thermal equilibrium in the core plasma. The comparison shown in Fig. 3.22 depicts that the increment of fitting results provided by the cut-off fitting routine has improved the statistical sample. This can be seen as a decrease of the scatter in the resulting RFA-like T_i profile, while the trend of the profile remains the same.

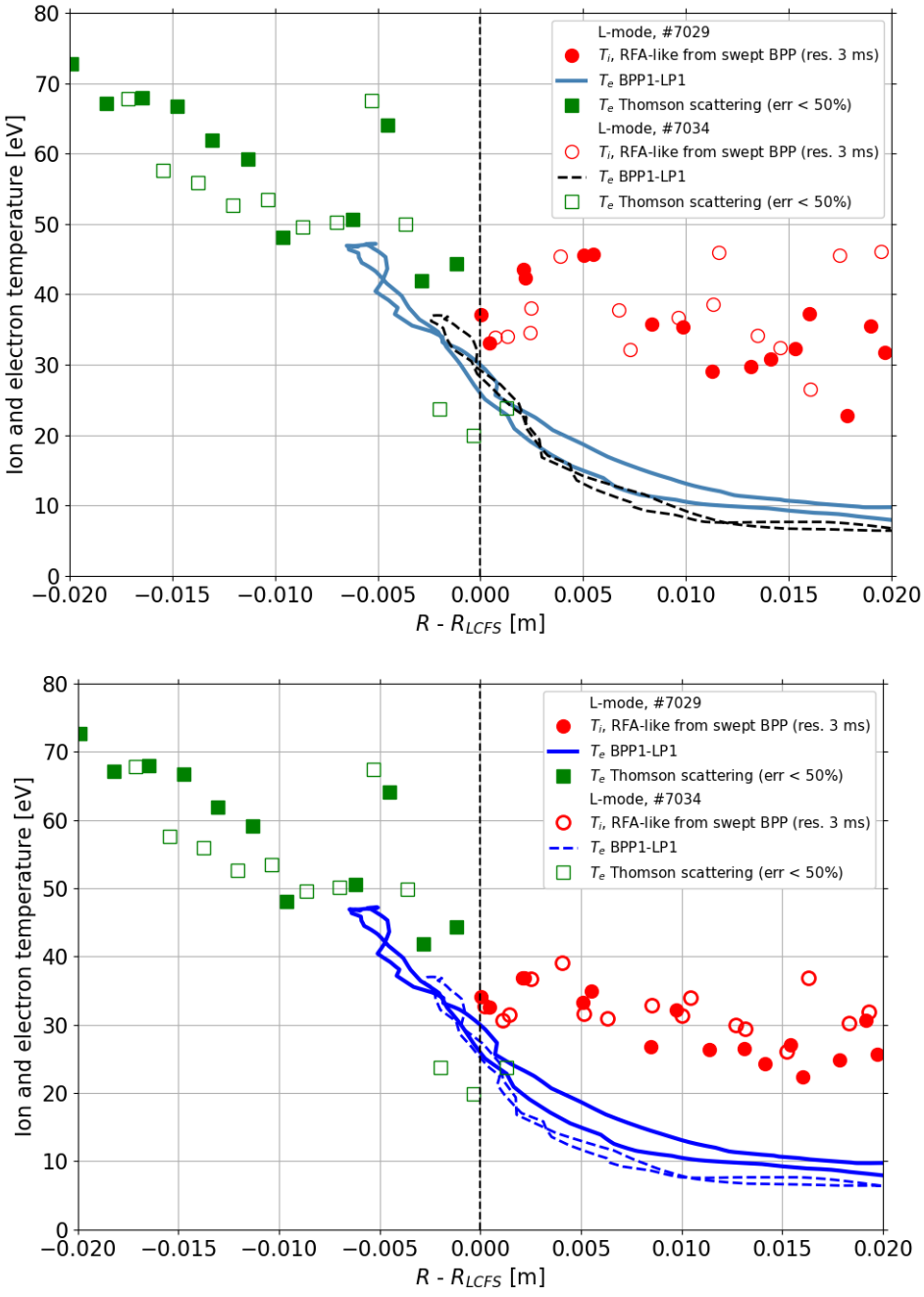

Figure 3.22: Radial profile of the ion temperature with low temporal resolution (3 ms) resulting from linear fit of the RFA-like *I-V* characteristics (red circles). The electron temperature is obtained from floating BPP and LP and smoothed with 0.1 kHz lowpass filter (lines). The electron temperature profiles obtained from Thomson scattering system (squares) are shown. Top figure shows the results published in [34]. The bottom figure shows results of the improved analysis with the cut-off refit procedure applied. Shots: #7029, 7034.

3.6 Comparison of results from discharges with different densities

In this section we summarize the all the results from a systematic measurements of the ion and electron temperature with a reciprocating probe. The experimental session took place on 17.04.2014 on the tokamak COMPASS. Eight L-mode discharges with different electron densities performed during this session were analyzed and the results compared. As can be seen in Fig. 3.23 the individual discharges have almost identical macroscopic plasma parameters such as the plasma current, the H_α signal and the loop voltage shown in Fig. 3.23 a), c) and d) respectively, which implies good discharge reproducibility. All the measurements with reciprocating probe were normalized to the position of LCFS as was described in section 3.1.4. This enables us to compare the results from the same regions in the SOL of all these discharges.

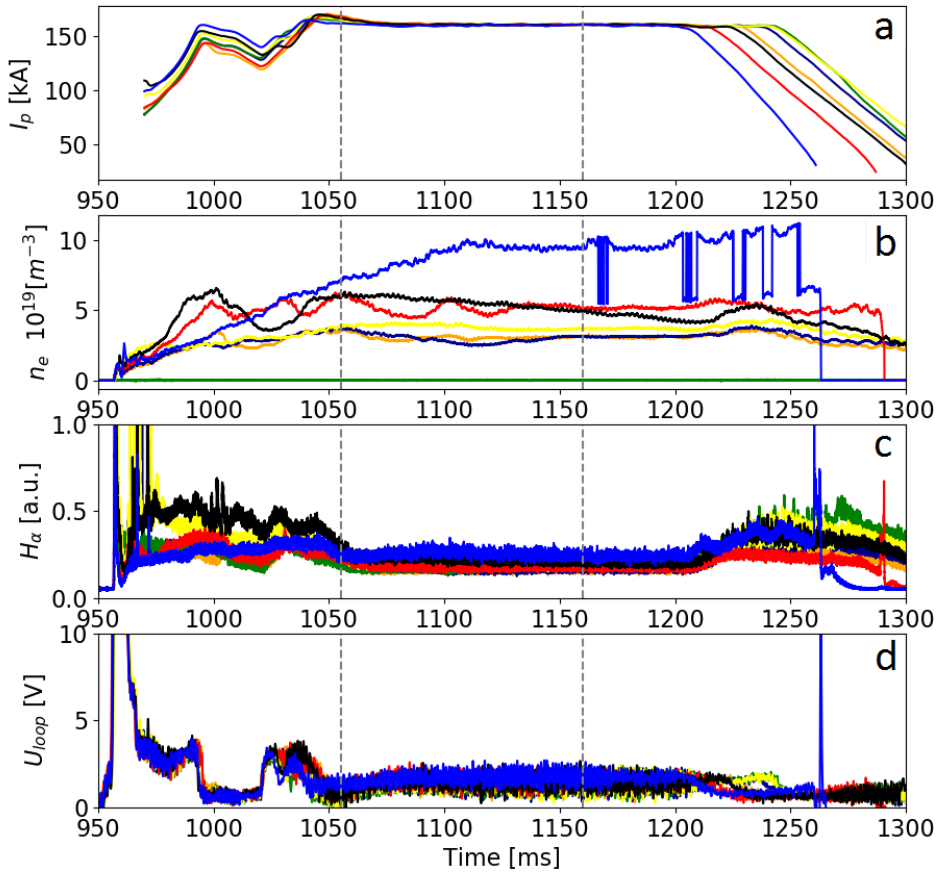

Figure 3.23: Comparison of a temporal evolution of macroscopic plasma parameters during discharges #7023, #7024, #7025, #7026, #7027, #7029, #7034, #7038. The following discharge parameters are plotted: a) plasma current, b) the line-average density, c) H_α signal, d) loop voltage.

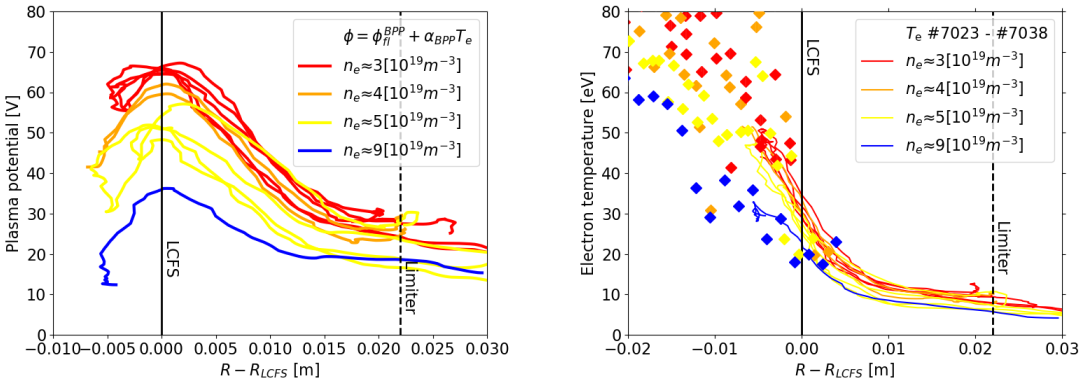

Figure 3.24: Radial profile of the plasma potential (left) and electron temperature (right) measured during 8 discharges with different densities. Measurements with a ball-pen and Langmuir probe were smoothed with a 0.1 kHz lowpass filter (lines). Measurements of T_e performed using Thomson scattering system are plotted (diamonds). The density scan of Φ and T_e are both showing significant decrease with the increasing line-average density.

3.6.1 Limitations of the technique

As does any other experimental technique, the ion temperature measurement using a swept BPP has its limitations given by the technical parameters of the experimental setup. First of all, the most obvious limitation comes from the nature of plasma probes. Since the direct contact with plasma is required, the radial position of the probe head is restricted to the scrape-off layer of plasma. Intruding deeper into the core plasma will necessarily soon overreach the maximum heat flux on the probes and will lead to the probe self-emission. If the probe is self-emitting the measurement can not be taken into account. The transition into self-emission with increasing depth of probe insertion greatly depends on plasma density and can be observed as a strange change in the probe data, in particular a sudden drop in T_e. The lower the plasma density the higher is the heat flux on the probe and the risk of transition into self-emission for the same radial position.

The second limitation depends on the plasma density. As can be seen in Fig. 3.24, the plasma potential is higher during discharges with lower electron density. The parameter T_i is obtained from the exponential decay of the ion current above the plasma potential, according to eq.(3.5). Thus the amplitude of voltage applied to the probe above the plasma potential must be sufficiently high in order to capture the exponential part of the *I-V* characteristic. Condition used throughout this thesis was set to $T_i < (V_{peak} - \Phi)$, which means that the saturation ion current exponentially decays at least to e^{-1} or approximately (37%) of its saturated value in the given voltage interval. This condition (visualized in Fig. 3.25) sets a limitation for the highest possible ion temperature measured given the voltage amplitude and the plasma potential. Therefore, in order to perform measurements in low density plasma in the near SOL region the amplitude of applied swept voltage must be set higher. Low density discharges are also characterized by higher electron temperatures as was shown before. Thus, the power load drawn from the voltage amplifier is higher and more likely to reach it's limitation. We often observe the swept voltage amplifier shut-down in the region inside the separatrix during low density discharges.

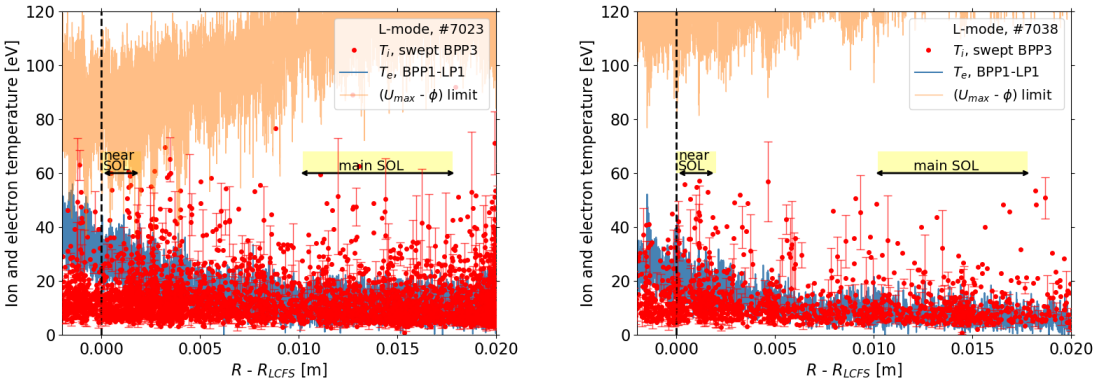

Figure 3.25: Comparison of radial profiles of T_i and T_e measured during low density $n_\mathrm{e} \approx 3$ m^{-3} (left) and high density $n_\mathrm{e} \approx 9$ m^{-3} (right) discharge. The limitation $T_\mathrm{i} < (V_\mathrm{peak} - \Phi)$ is shown, where Φ was obtained from the floating probes during the same discharge. We can see that the measurement in the low density discharge is affected by the limitation in the near SOL region, while the measurement during high density discharge is not.

3.6.2 Comparison of histograms resulting from the fast measurements during discharges with low and high density

In order to compare the ion temperature measured with (10 μs) resolution during discharges with $n_\mathrm{e} \approx 3$ m^{-3} and $n_\mathrm{e} \approx 9$ m^{-3} histograms were constructed from the same region in the main SOL. Comparison in the near SOL region is not possible due to the possible technique limitation described before. Both the histograms plotted in Fig. 3.26 show non-Gaussian distribution of the ion temperatures. Low temperature peak corresponds to the background plasma and the tail corresponds to intermittent blobs. We observe that the histogram representing both T_i and T_e during the discharges with ($n_\mathrm{e} \approx 3$ m^{-3}) is shifted toward higher temperatures in comparison to the histogram representing the discharge with ($n_\mathrm{e} \approx 9$ m^{-3}). This could indicate stronger damping of the ion and electron temperature fluctuations in the main SOL region of a high density discharge. The damping effect is more apparent on the electron temperature.

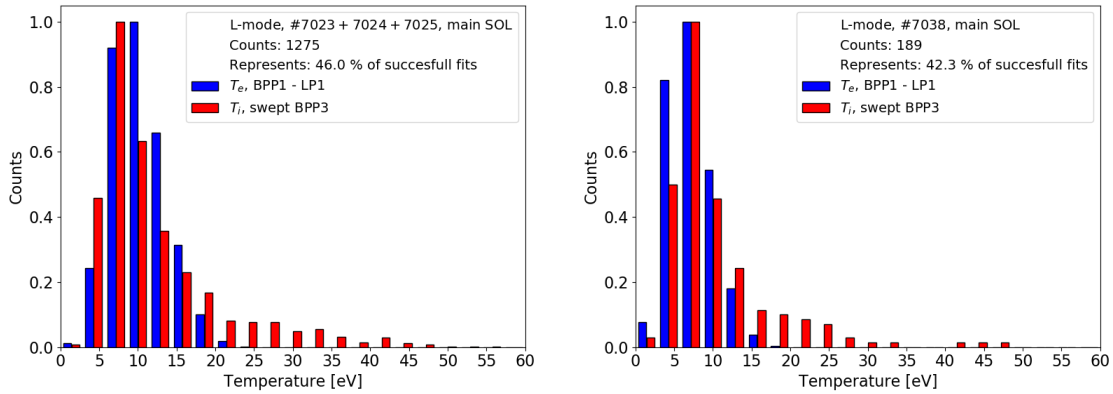

Figure 3.26: The resulting histograms of fast T_i and T_e measurements in the main SOL of 3 discharges with low density $n_\mathrm{e} \approx 3$ m^{-3} (left) and 1 high density discharge $n_\mathrm{e} \approx 9$ m^{-3} (right). In low density discharge the histograms are shifted toward higher temperatures.

3.6.3 Comparison of RFA-like radial profiles of discharges with low and high density

In the Fig. 4.2 we can see the comparison of the low resolution (3 ms) radial profiles resulting from linear fits of the artificial RFA-like *I-V* characteristics constructed from fast measurements during discharges with $n_e \approx 3$ m^{-3} and $n_e \approx 9$ m^{-3}. The ion temperatures measured in the vicinity of LCFS during the low density discharges are affected by the technique limitation (see Fig. 3.25), thus the results in this region are plotted in gray color. Since, the high density discharge should not be affected, the results are plotted even inside LCFS. However, despite the sufficient voltage range for high temperature measurement, we observe that the high ion temperatures "disappear" inside the LCFS. This can be seen as a drop in ion temperature in Fig. 4.2 (right graph) at $R \approx -0.002$ m. For this reason the measured values inside LCFS are potted in gray. Possible explanation for the missing T_i values is shorter shear flow decorrelation time in the vicinity of the LCFS. The high temperatures appear again when the probe moves even deeper inside LCFS, observed as a sudden increase of T_i in Fig. 4.2 (right graph) at $R \approx -0.005$ m. Where we can observe the ion to electron temperature ratio converge to unity deep inside LCFS.

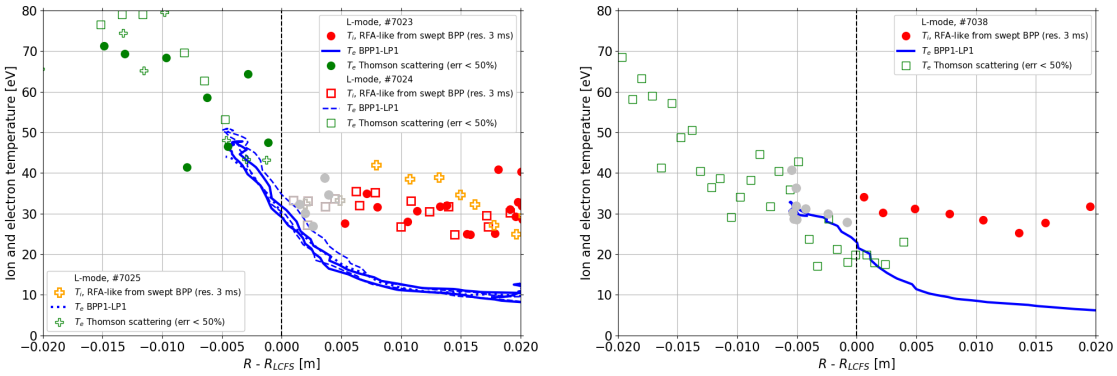

Figure 3.27: The radial profiles of T_i with low temporal resolution (3 ms) resulting from three low density discharges $n_e \approx 3$ m^{-3} (left) and one high density discharge $n_e \approx 9$ m^{-3} (right).

3.6.4 Ion and electron temperature density profiles

In this section we compare the ion temperatures obtained with 3 ms resolution during discharges with different densities. We have chosen two regions, in particular, the main SOL and the near SOL region, where the mean and a standard deviation of the ion and electron temperature is calculated for each discharge. We plot the mean values against the line-average density of the discharge, measured simultaneously with the probe measurement.

The results calculated in the main SOL region are shown in Fig. 3.28 on the left. We observe that the average ion temperature increases with decreasing density when $n_e < 3$ m^{-3}. The electron temperature depends weakly on the line-average density. The ion-to-electron temperature ratio in this region can be estimates as 3-4.

The results obtained in the near SOL region are plotted on the right side of the Fig. 3.28. We need to take into consideration the effect of the increasing plasma potential on the highest possible T_i that can measured. The resulting ion temperatures affected by the limitation are plotted in gray color. The ion-to-electron temperature ratio in this region can be estimates as 1-2.

Since the ion pressure has as a larger perpendicular but smaller parallel dissipation rate compared to the electron pressure, ion energy is transported far into the SOL. This implies that the ion temperature in the SOL should exceed the electron temperature. On AUG, JET, KSTAR, EAST were the ratios of ion to electron temperature also observed as 2-4 [41].

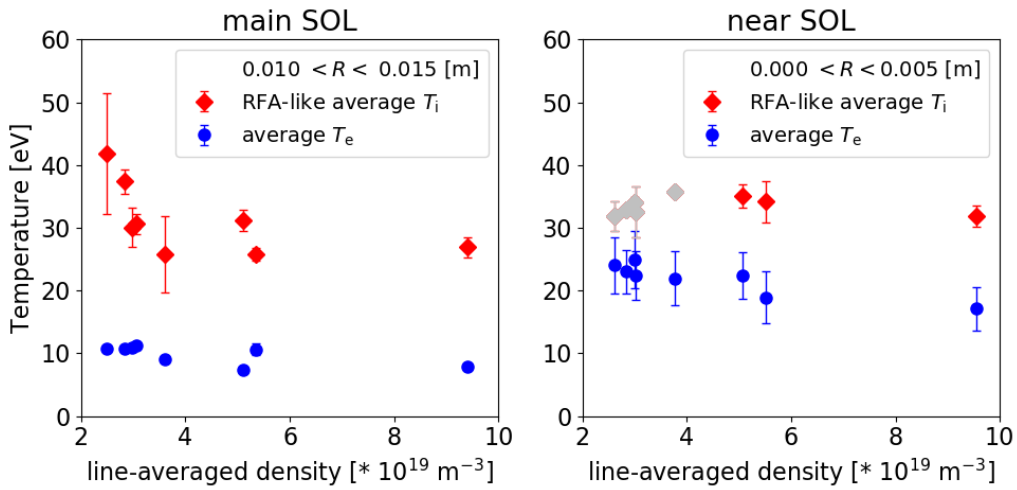

Figure 3.28: Ion and electron temperature density scan, measured at COMPASS during L-mode discharges (#7023 – #7038). Temperatures are plotted against the line-averaged plasma density showing comparison between near (right) and main SOL (left). We can see that the T_i/T_e ratio in the main SOL is higher than the ratio in the vicinity of separatrix.

Chapter 4

Measurement on the tokamak GOLEM

In this chapter results from measurements of the ion and electron temperature in Scrape-Off Layer of tokamak Golem are presented. At first the calibration constant α_{BPP} must be calculated for the currently installed BPP for the hydrogen plasma. We have found that the BPP operates correctly when the toroidal magnetic field applied is $B_{tor} > 0.22$ T. The ion temperature was measured using a swept ball-pen probe and the electron temperature was calculated using an equation (2.9) from floating potentials of ball-pen and Langmuir probe. Python script was developed for easy loading, fitting and plotting of the acquired and calculated data. A temporal evolution of the ion temperature was studied using a stationary probe placed at different radial positions. Average values of the ion temperature were estimated from synthetic RFA-like *I-V* characteristics.

4.1 Tokamak Golem

Tokamak golem is a small device currently operated by the Czech Technical University at the Faculty of nuclear sciences and physical engineering in Prague. Unique feature is possibility to operate the tokamak remotely from any computer connected to the internet. The engineering and plasma parameters are shown in Table 4.1. Golem, originally named TM-1 is the oldest tokamak still in operation. In 1977 it was installed at IPP in Prague under a name Czech Academy of Sciences TORus (CASTOR). Recent photograph of the tokamak Golem is shown in Fig. 4.1.

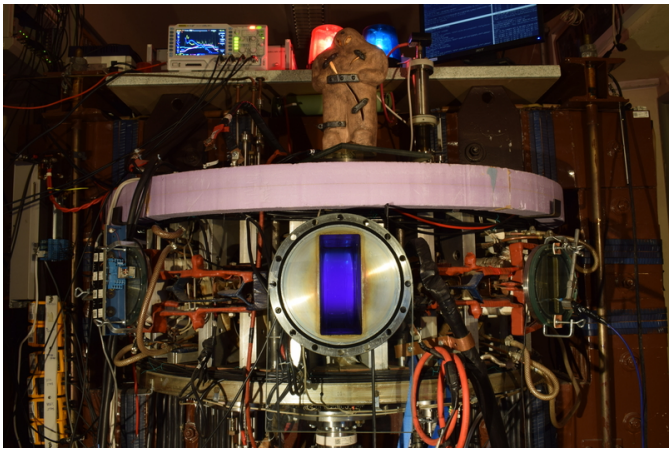

Figure 4.1: Tokamak Golem. [42].

Major radius of vessel (R)	0.4 m
Minor radius of vessel (r)	0.1 m
Minor radius of plasma (a)	0.085 m
Plasma current (I_P)	< 8 kA
Magnetic field (B_T)	< 0.5 T
Electron density (n_e)	$< 3 \times 10^{19}$ m^{-3}
Poloidal plasma shape	Circular
Plasma duration	≈ 20 ms
Loop voltage	1-2 V

Table 4.1: Basic parameters of the tokamak GOLEM.

The main purpose of this tokamak is to provide students "hands-on" experience with fusion a device. This is achieved due to simplicity of the device and exposed key components of the device (toroidal vacuum chamber, magnetic field coils, plasma diagnostics, etc.). Basic plasma diagnostics on this device include a coil wrapped around the transformer core for the U_{loop} measurement, a Rogowski coil wrapped around the vacuum chamber for the I_p measurement. Typically used working gas is Hydrogen and Helium. A combined probe head equipped with Langmuir probe (LP) and a ball-pen probe (BPP) was installed on a manual manipulator and inserted through a diagnostic port, located at the bottom of the tokamak GOLEM, into the scrape-off layer of plasma. The location of the probes is indicated in Fig. 4.2. Probes on the manipulator were placed perpendicular to the magnetic filed lines. It is important to note that the probes can not placed behind each other, relative to the magnetic field lines, otherwise one of the probes would lie in "shade" of the other. The probe head with BPP and LP on a manipulator is shown in Fig. 4.2. The probe position (distance) from the center of the vessel can be manually changed on shot-to-shot basis. The probe head insertion ranges between 100 mm (furthest) and 55 mm (deepest) and is set by a swivel thread manually before discharge. The diagnostic port is located at the radial position of $R = 97$ mm. Before the experimental sessions the tokamak was always purged by baking at 200° C and by a subsequent glow discharge in helium and was well prepared for measurement. Data Acquisition System (DAS) was set to sampling frequency of $f = 12.5$ MHz, allowing for measurement of the *I-V* characteristics with enough detail, even when the collector is biased with a voltage swept at a frequency of 100 kHz. The DAS sampling frequency is usually the limiting factor for temporal resolution of fitting routines.

4.2 Measurement of the calibration constant α_{BPP}

Prior to measurement of the ion temperature (T_i) using a swept ball-pen probe or a measurement of electron temperature (T_e) using BPP in a floating regime, it is necessary to acquire the calibration constant α_{BPP} for the used experimental set-up. This constant depends on construction of the BPP (position of a collector), as well as, on the tokamak plasma parameters, especially on the applied magnetic field. At tokamak GOLEM the task of obtaining the α_{BPP} is more complicated than on other devices (COMPASS, ASDEX-U) due to the magnetic field ramp-up from 0 T to max. 0.5 T throughout the whole discharge. The toroidal magnetic field strength is non-linearly increasing until reaching its maximum. We have performed multiple identical discharges, from which one discharge # 35366, has the macroscopic parameters potted in Fig. 4.4.

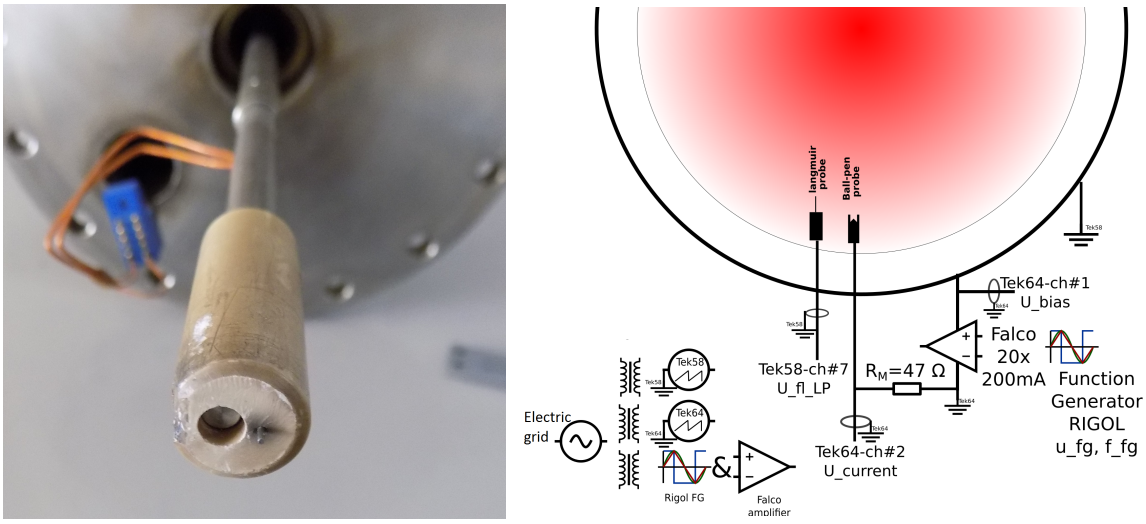

Figure 4.2: The manipulator installed on GOLEM carrying a probe head with LP and BPP [42] (left) and the view of a tokamak plasma cross-section with a simplified schematic of the experimental set-up on tokamak Golem (right).

4.2.1 Experimental setup

Data Acquisition System (DAS) was set to sampling frequency of $f = 12.5$ MHz. The coaxial cables had length of 7 m. In order to calculate the α_{BPP}, the ball-pen probe must be in a swept regime. The collector of ball-pen probe was fixed at position $h = -2.3$ mm. Swept bias voltage applied on the BPP collector was created by a function generator Rigol in a sine waveform, with an amplitude of 10 V at a sweeping frequency of 10 kHz. The signal was amplified by Falco systems WMA-100 high voltage amplifier. Resulting in BPP biased with voltage of -150 to +150 V. However, the oscilloscopes in this measurement were not yet connected to the grid through to individual galvanicaly separators. As a result the U_{loop} signal was superposed to the measured signal. The parasitic signal was successfully removed by subtracting the signal measured during vacuum discharge # 35353 with identical parameters from the signal measured in all the plasma discharges performed during this experimental session.

4.2.2 Signal preprocessing

At first a lowpass filter was applied in order to remove structures with much higher frequency than the voltage sweeping frequency. During this experimental campaign, that took place on 4.2.2021 we have performed measurements with the sweeping frequency of $f = 10$ kHz. We found the typical cut-off frequency of 74 kHz, representing 7 harmonics visible above the noise level (see Fig 4.11 b)). An example of the signal preprocessing routine is shown on Fig. 4.3. Note that we used sine waveform of the swept voltage.

4.2.3 Description of the method

At first the *I-V* characteristics needs to be normalized to ion saturation current (I_{sat}^{+}). The normalization is crucial for removing the effects of the plasma density fluctuations during the discharge and enables us to compare the results of multiple discharges. The value of I_{sat}^{+} can be obtained simply by performing a linear extrapolation of the "saturated" part of the ion branch. The difficulty of this approach lies in the very definition of the saturated part. Since the voltage from which the

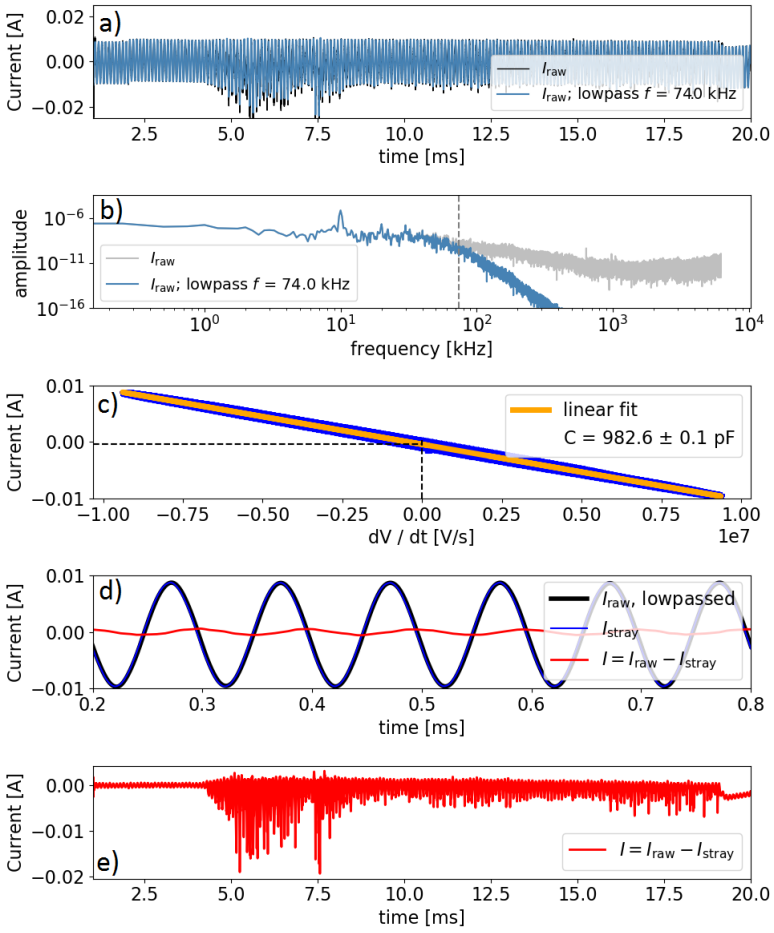

Figure 4.3: An example of the stray current reconstruction and removal for a discharge with voltage swept at $f = 10$ kHz. The figure a) shows an overview of the signal measured with swept BPP during the discharge (black) and the lowpassed signal (blue). The figure b) shows the Fourier transform of the signals. The figure c) shows the fit of a linear dependency between current measured and the first derivative of voltage applied. The figure d) is an enlarged interval before the discharge used to reconstruct the stray current. The figure e) is the final result of the signal preprocessing (red signal). Shot: #35366.

ion branch saturates is not constant and the *I-V* characteristics can fluctuate the results can often be affected by our choice of suitable fitting region. In order to avoid the possible confusion we can perform a 4-parameter fit of the ion-branch of the BPP *I-V* characteristics. The ion branch of BPP characteristics is measured when the bias voltage is below the plasma potential. We found an analytical function describing the ion-branch of BPP given as:

$$I = I_{\mathrm{sat}}^{+}[1 + K(V - \Phi_{\mathrm{fl}}^{\mathrm{BPP}})] - I_{\mathrm{sat}}^{+} \exp\left(\frac{(V - \Phi_{\mathrm{fl}}^{\mathrm{BPP}})}{T_{\mathrm{e}}}\right). \tag{4.1}$$

The 4-parameter fit is capable of accounting for the possible sheath expansion effect causing the linear growth of the ion saturation current with a slope $\frac{\Delta I}{\Delta V} = K$. This approach is routinely used in fitting the non-saturated ion branch of Langmuir probe I–V characteristics [16]. After the estimation of saturation current the whole I–V characteristics can be normalized. The example of

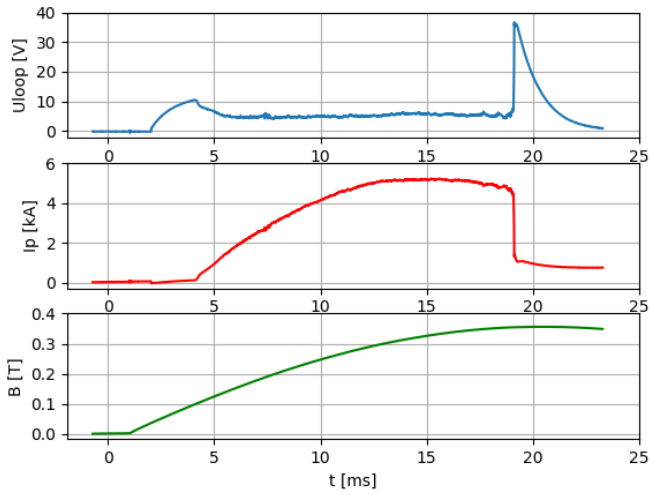

Figure 4.4: Macroscopic plasma parameters of a typical discharge at tokamak GOLEM Shot: # 35366.

4-parameter fit of the BPP ion branch and subsequent normalization to ion saturation current is shown on Fig. 4.5.

Secondly we need to estimate the electron saturation current from the electron branch of the *I-V*. Again it can be obtained simply by performing a linear extrapolation of the saturated part of the electron branch. The same difficulties apply as was discussed before. We approach the problem in a similar way. However, the electron branch tends to fluctuate on a much greater scale than the ion branch. In order to reduce the fluctuations it is reasonable to use an averaging method to receive more stable fits. We than repeat same process as discussed before, but this time for 10 single *I-V* characteristics. Each *I-V* charactristic is normalized to it's I_{sat}^{+}. These normalized *I-V* characteristics are than averaged into a single (slow) "bin-averaged" *I-V* characteristic over a period of 0.5 ms, with voltage bins of 10 V. This technique provides a robust approach to fitting and delivers stable parameters (see Fig. 4.6).

Now we can proceed to fitting of the bin-averaged *I-V* characteristics using a 4-parameter fitting formula. The analytical function 3.5 describing the electron branch of BPP needs to be modified since the electron branch was normalized to ion saturation current. We receive:

$$I = \mathscr{R}[1 + K(V - \Phi)] - 1 \exp\left(\frac{\Phi - V}{T_i}\right), \text{ where } \mathscr{R} = \frac{I_{sat}^{-}}{I_{sat}^{+}}. \tag{4.2}$$

The ratio of electron to ion saturation current $\mathscr{R}$ is obtained directly as a parameter of the 4-parameter fit. The calibration coefficient is then $\alpha_{BPP} = \ln(\mathscr{R})$. However, in order to increase the precision and stability of the fit, we estimate the plasma potential and fix the parameter Φ in the equation 4.2. The plasma potential of the ball-pen probe is located in the inflection point. Since we are fitting the smooth bin-averaged *I-V* characteristics, the plasma potential can be easily found as a second derivative of the collector current equaling zero. An approximate, but stable resulting value of the plasma potential can be calculated when we fit the dependency of d^2I/dt^2 on the voltage applied in an interval (-50 V; +50 V) with a linear function $a * x + b = 0$. Then the x-intercept of the linear dependency ($-b/a = \Phi$). This method effectively diminishes the possibility of false (double) extremes.

However, the normalized 4-parameter fit of the electron branch is not correct when $I_{sat}^{-} \gg I_{sat}^{+}$.

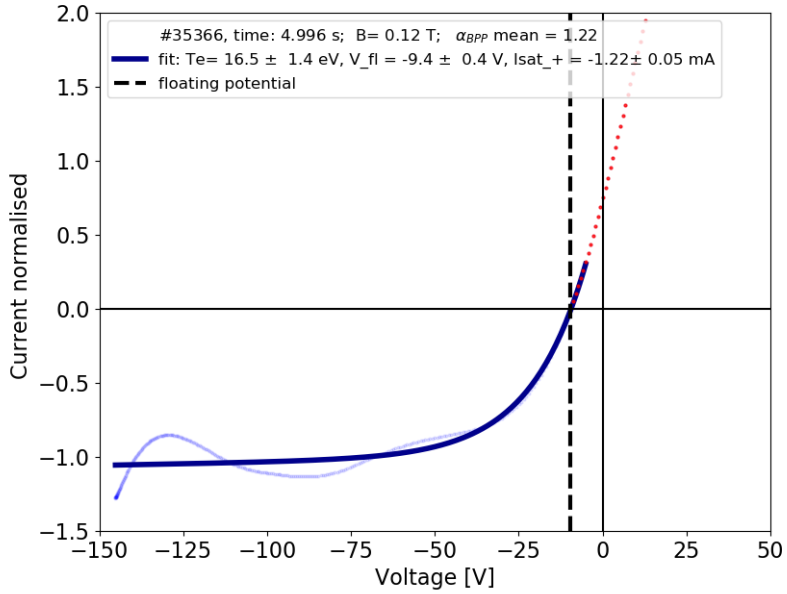

Figure 4.5: An example of the 4-parameter fit (dark blue) of the BPP ion branch (light blue) 4.1 and subsequent normalization to ion saturation current.

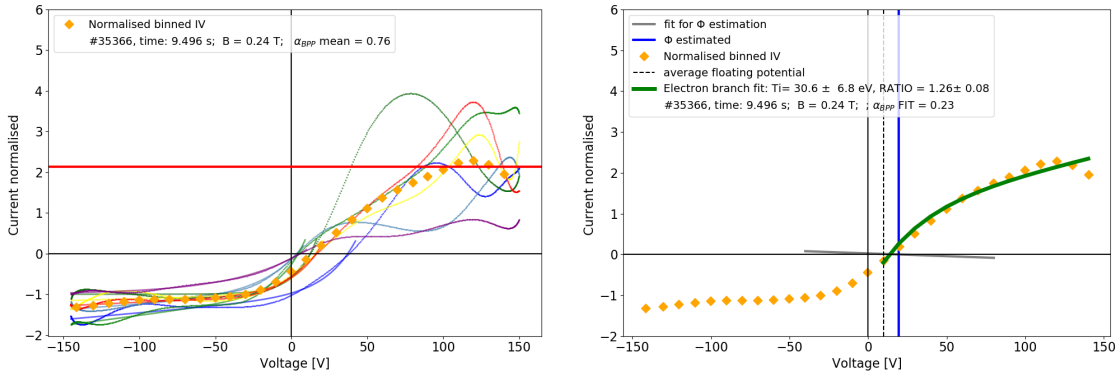

Figure 4.6: All the individual *I-V* characteristics (and individual fits of the ion branch) used to construct the normalized average *I-V* characteristics (orange diamonds) are shown in the figure on the left. The mean of saturated part of electron branch (red horizontal line) is the first estimate of electron to ion saturation current ratio. An example of the 4-parameter fit (4.2) (green) of the bin-averaged *I-V* characteristics is hown on the right. The black dashed line represents the average floating potential. The gray line is a linear fit of the second derivatives of the bin-averaged *I-V* characteristic on the voltage applied, used for locating the plasma potential (blue line).

This assumption is a requirement for the minimum magnetic field applied, where the effect of the systematization of the BPP *I-V* characteristic appears. In a very low magnetic field the Larmor radius of electrons increases until the electrons start to ignore the shielding tube and transport to the collector the same way ions do. In this case the BPP works as a simple Langmuir probe. The BPP operating as a Langmuir probe is undesirable. If this condition is not met we can only estimate the electron saturation current using a mean value from a chosen (saturation) interval (+80 V; +140

V) of the electron branch. This estimated (approximate) value of I_{sat}^{-} is used for confirmation of validity of 4-parameter fit 4.2. We have applied a condition: $I_{sat}^{-} < 4$, where 4 represents $4 * I_{sat}^{+}$ normalized to 1. When this condition is satisfied we can fit the electron branch and obtain the value of $\mathscr{R}$ as a fitting parameter. The received mean values of the saturation interval are only an approximate estimation of the ratio and are not used for calculation of the final α_{BPP}.

In order to construct the dependency of the coefficient on magnetic field strength, the above described process is run over the whole discharge. Extremely unsaturated *I-V* characteristics (10% of all available) were removed from the bin-averaging process. The bin-averaged *I-V* characteristic is constructed from 0.5 ms (10 *I-V*s) time interval using a "running" (or "floating") window, with a step of 0.05 ms (1 *I-V*). For better statistics 3 discharges were used for calculation of the mean value and the standard deviation of the final α_{BPP} (see Fig. 4.7).

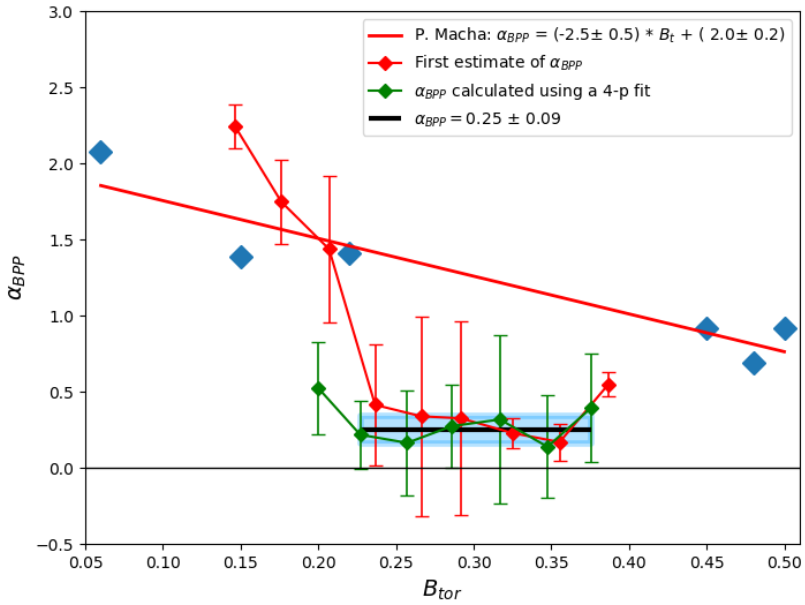

Figure 4.7: The resulting coefficient $\alpha_{\mathrm{BPP}} = 0.25 \pm 0.09$ (black line) was found as a mean of smooth (bin-averaged over 0.03 T) results gathered from 3 different discharges #35347, #35352, #35366 (green diamonds). The confidence interval of 1σ is indicated (blue area).The first estimates of the coefficient are shown (red diamonds). The previously found calibration dependency calculated by P. Mácha [43] is shown for comparison (blue diamonds, red line).

4.2.4 Summary

A calibration constant for BPP currently installed at GOLEM was found using a 4-parameter fit of the electron branch normalized to ion saturation current. The resulting dependency of calibration coefficient on magnetic field (Fig. 4.7) shows good agreement of two different approaches of the coefficient estimation in the interval 0.22 T - 0.4 T. The resulting coefficient was found as $\alpha_{\mathrm{BPP}} = 0.25 \pm 0.09$. We have also found an optimal magnetic field strength interval for the measurement as 0.22 T - 0.4 T, where the BPP operates correctly and *I-V* characteristics are symetrized. The upper boundary of 0.4 T is given by the effective signal strength, which decreases with the strength of magnetic field applied. For higher effective signal (higher plasma density, shorter coaxial cable,

radial probe position closer to central plasma) the upper boundary can be increased assuming the ball-pen probe operates as expected. This calibration can be used for future measurements of plasma potential, electron and ion temperature with ball-pen probe (collector position h = - 2.3 mm) on GOLEM.

4.3 Measurement of the ion and electron temperature on Golem

In this section we present the first results of the ion and electron temperature measurements on the tokamak Golem using a ball-pen and Langmuir probe. The experimental set-up shown on Fig. 4.2 was used for the ion temperature measurement with high temporal resolution.

4.3.1 Experimental setup

All coaxial cables were specially shortened in order to minimize effects of the cable capacitance to a length of 1 m. Both oscilloscopes used were connected to the electric grid through separate galvanic isolators as is indicated on Fig. 4.2. Swept bias voltage applied on the BPP collector was created by a function generator Rigol as a triangular waveform, from -10 to +10 V. The signal was amplified by Falco systems WMA-100 high voltage amplifier in order to reach the sweeping amplitude of 90 V. Measurement of the electron branch requires sweeping positive voltage above the plasma potential, therefore a constant voltage of (+60 V) generated by DC power supply was also connected to the sweeping circuit in series with the amplifier. The resulting bias has a voltage of -30 to +130 V, at a sweeping frequency of 50 kHz. This voltage range enables us to measure the parameter T_i even if the plasma potential is close to zero or negative. A sweeping frequency of 100 kHz was also tested during this experimental session. The discharge parameters were set to:

Voltage on condenser batteries powering toroidal magnetic field coils: $U_{Bt} = 1200$ V,

Current drive field source voltage: $U_{CD} = 450$ V,

Requested gas pressure: $p = 16$ mPa.

Resistor: $R_\mathrm{i} = 47\,\Omega$.

Since only one ball-pen probe could be placed on the vertical manipulator, we have preformed two identical discharges at the same radial position of the manipulator. During one of the discharges the electron temperature was measured using the relation 4.3. During the second discharge the Ball-pen probe was biased with swept voltage. The radial position of the manipulator in range of 80 to 58 mm. The position was changed on shot-to-shot basis. The comparison of the macroscopic plasma parameters of all the analyzed discharges is shown in Fig. 4.8. We can assume that the performed discharges were nearly identical and the quasi-stationary phase of the discharge is at $6 < \mathrm{t\ [ms]} < 17$. During this interval strength of the toroidal magnetic field increased from 0.22 T up to 0.5 T. However, the position of the plasma column is not constant in time. Typically the stabilization is tokamak is performed by a feedback loop, which is not yet installed on Golem. As can be seen on the right-hand side of the Fig. 4.9, with increasing magnetic field $B_\mathrm{tor}(t)$ the radius of the plasma column is decreasing, as well as, the plasma center position shifts toward the High Field Side (HFS). The probe measurements performed with a stationary probe must be analyzed and compared with respect to the strength of magnetic field. Also we can assume that all the measurements within the radial position range of 80 to 58 mm were performed in the scrape-off layer of plasma.

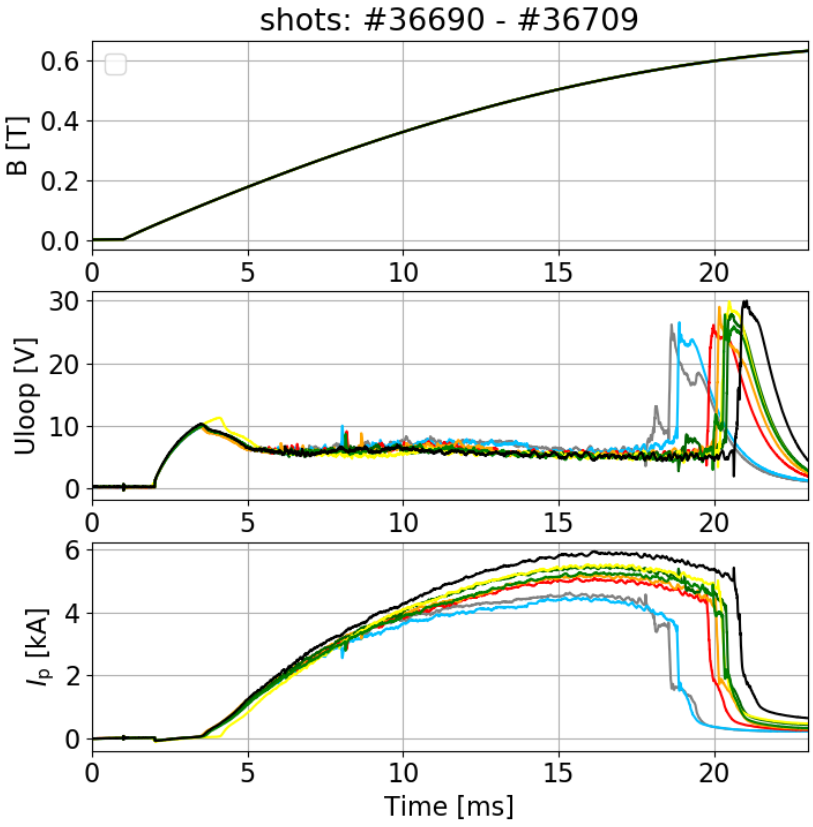

Figure 4.8: Comparison of the macroscopic plasma parameters of all discharges, during which the ion and electron tempearature was studied.

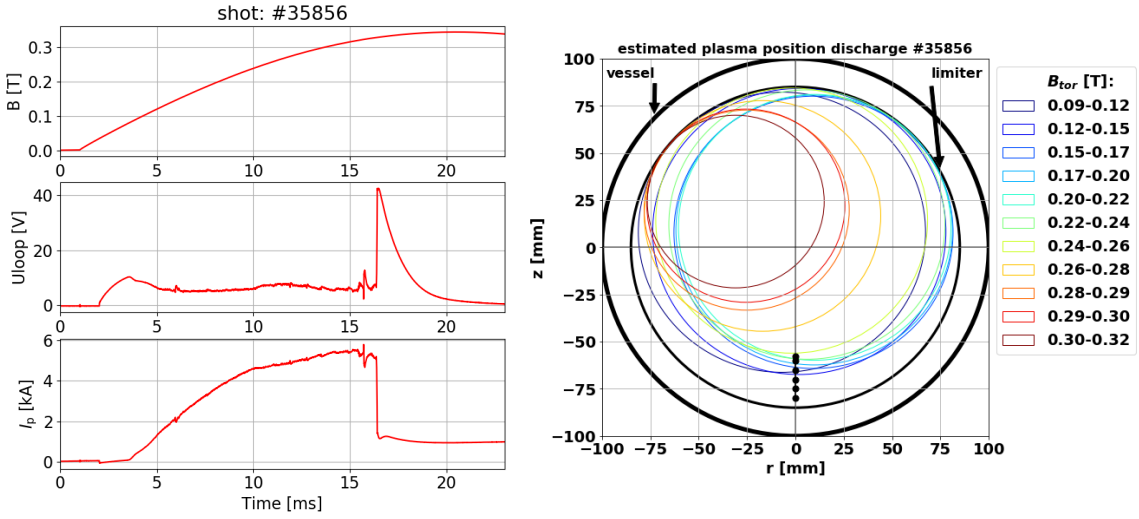

Figure 4.9: An example of the change of a separatrix position during a discharge due to the increasing B_{tor} is shown on the right (courtesy of P.Mácha). The stationary probe radial positions are indicated (black dots). The measurement was performed in a discharge with macroscopic parameters plotted in figure on the left.

4.3.2 Electron temperature measurement using floating LP and BPP

The electron temperature measurement on Golem was performed using the same technique as on the tokamak COMPASS, using the equation:

$$T_e = \frac{\phi^{BPP} - V_{fl}^{LP}}{\alpha_{LP} - \alpha_{BPP}}, \text{ where } \alpha_{LP} - \alpha_{BPP} = 2.5 \tag{4.3}$$

The coefficient $\alpha_{LP} - \alpha_{BPP} = 2.5$ was measured on tokamak Golem [44]. The manipulator does not reciprocate during the discharge. Thus, we can compare the measurements preformed on different radial positions only on shot-to-shot basis. Examples of temporal evolution of the LP and BPP floating potential along with the electron temperature are shown in Fig. 4.10. Note, that due to the significant change of the plasma column position the resulting electron temperature temporal evolution is constant of slightly decreasing during the discharge. An observation of this strange behavior of T_e evolution confirms the estimated evolution of the plasma position. The relatively low electron temperature (≈ 7.5 eV) and an absence of electron temperature gradient (measured even at a radial position $R = 58$ mm) indicates that the probe did not cross of even reach the vicinity of a separatrix. Insertion of the probe deeper into the plasma, for example at $R = 55$ mm, was already causing plasma disruptions, difficulties with ignition or significant cooling of plasma, since at the beginning of the discharge the plasma is located significantly closer to the diagnostic port on the bottom of the tokamak.

4.3.3 The ion temperature measurement

In order to understand the measurements of the ion and electron temperature on tokamak GOLEM we need to take into consideration:

- The strength of toroidal magnetic field is increasing during the whole discharge
- The plasma current is increasing during the whole discharge
- The position of plasma and it's radius is changing with strength of the toroidal magnetic field during the whole discharge
- The collector may be retracted too deep into shielding tube

From the measurement of the calibration constant we have found the optimal range of the toroidal magnetic field for the BPP with a collector position of $h = -2.3$ as $B_{tor} > 0.22$ T. The field coils creating the toroidal magnetic field are powered by capacitor batteries and the resulting intensity follows a sinus function. With an increasing toroidal magnetic field the plasma confinement also increases. The increase of toroidal field is accompanied by an increase of the toroidal plasma current I_p, which is responsible for the poloidal magnetic field and in turn ohmic heating and equilibrium. Since the plasma position is not stabilized by a feedback system the plasma position and radius changes. The radius decreases and center of the plasma drifts away from the probes as we increase the toroidal magnetic field. Therefore, in order to account for the change of the plasma position and other properties, we must take into consideration only short time intervals corresponding to a specific magnetic field strength.

Other difficulty that appeared during the experiments on Golem is that the effective signal was in order of tens of mA, much lower comparing to measurements on COMPASS. This could be caused by two factors. Measurements were performed far from the separatrix, due to change in plasma position. And the BPP collector retraction into the shielding tube ($h = -2.3$). Note that the effective signal measured by BPP decreases exponentially with the collector depth of retraction.

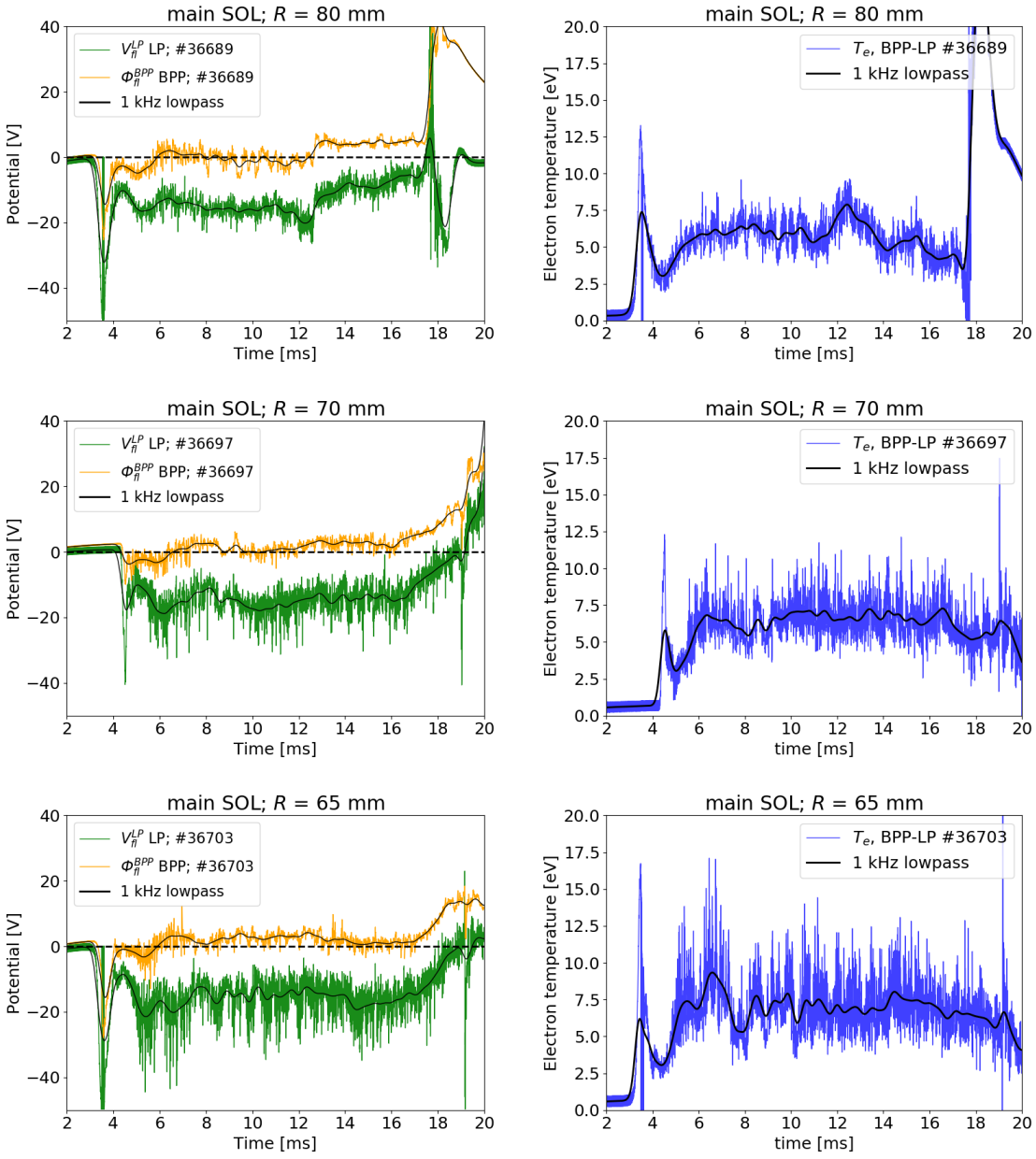

Figure 4.10: The temporal evolution of floating potentials measured with the Langmuir (green) and ball-pen probe (orange) are shown on the left. The temporal evolution of the resulting electron temperature, calculated using the equation (2.9) is shown on the right. Measurements were taken at different radial positions. Absence of a gradient of the electron temperature (with increasing depth of insertion) indicates that all the measurements were performed in the main (or far) SOL region.

If the collector was moved closer to plasma, in turn even higher magnetic field than $B_{\mathrm{tor}} > 0.22$ T would be required. The exact strength of the magnetic field required for the BPP operation would be obtained again form the calibration (described before) along with a new value of a calibration constant α_{BPP}. On the other hand, the high toroidal field would cause the plasma to be too far from the probes.

Solution of the problem would be placing the probes on a manipulator to the horizontal diag-

nostic port and installation of a plasma stabilization system.

Signal preprocessing

Lowpass filter was applied in order to remove structures with much higher frequency than the voltage sweeping frequency. During the experimental campaign, that took place on 5.5.2021 we have performed measurements with the sweeping frequency of $f = 50$ kHz as well as with $f = 100$ kHz. We found the typical cut-off frequency of 370 kHz for the sweeping frequency $f = 50$ kHz. The same cut-off frequency was previously found also at COMPASS. As for the sweeping frequency of $f = 100$ kHz an cut-off frequency of 740 kHz was used, representing 7 harmonics visible above the noise level (see Fig. 4.11 b)). An example of the signal preprocessing routine is shown on Fig. 4.11. Note that we used triangular waveform of the applied swept voltage, thus the voltage derivative is a constant (positive for ramp-up and negative for ramp-down), except for the points where the voltage reaches maximum or minimum. At these points "corners" appear, causing spikes in the resulting signal. Reconstruction of "corners" cannot be well performed, thus we can only avoid the spikes by cutting-off the parts of the *I-V* characteristics where the voltage applied is reaching maxima and minima. Result of the signal preprocessing is shown in Fig. 4.11 d) and e), we can see that the routine increased the effective signal roughly by a factor of 10.

4.3.4 The cut-off fitting technique

On the tokamak Golem the same improved analysis fitting approach was applied as previously described (see section 3.3.1). The cut-off fitting technique is based on varying the peak voltage, yielding one representative value of T_i from the flat-top phase of the *I-V* characteristic. The only difference is that on the tokamak Golem we must use the unweighted method for fitting the *I-V* characteristics. We cannot apply weighted fitting method due to changing magnitude the magnetic field and plasma current during the whole discharge. We use the same 4-parameter analytical function, describing the electron branch, given as:

$$I(V) = I_\mathrm{sat}^{+}\Big(\exp(\alpha_\mathrm{BPP})[1+K(V-\Phi)] - \exp((\Phi - V)/T_\mathrm{i})\Big), \tag{4.4}$$

where the coefficient $\alpha_\mathrm{BPP} = 0.25 \pm 0.09$ was obtained in the previous section. Examples of *I-V* characteristics fitted using cut-off fitting technique, according to the equation (4.4) are shown in Fig.4.12. The following filtering criteria for the quality of the fit are applied to all the presented results:

$$T_{\mathrm{i,err}}/T_\mathrm{i} < 0.5,$$
$$\Phi_{,\mathrm{err}}/\Phi < 0.5,$$
$$T_\mathrm{i} < (V_\mathrm{peak} - \Phi)/1,$$
$$R^2 > 0.9,$$

where $V_\mathrm{peak} = 120$ V is the peak value of voltage applied on the BPP. A criterion on coefficient of determination was added to further increase the credibility of the obtained results.

4.3.5 Temporal evolution of ion and electron temperature

Since the probes were stationary during the discharge we can study the evolution of the ion and electron temperature with time. In the Fig. 4.15 and 4.16 we can see the comparison of measurements with 5 μs and 10 μs resolution at two radial positions. The low electron temperature

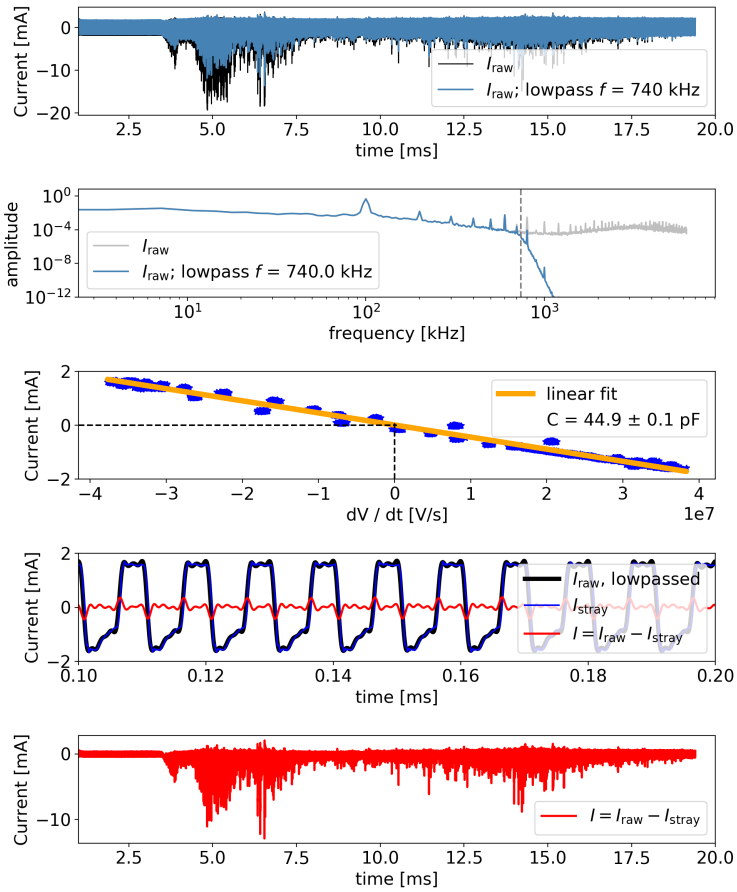

Figure 4.11: An example of the stray current reconstruction and removal for a discharge with voltage swept at $f = 100$ kHz. The figure a) shows an overview of the signal measured with swept BPP during the discharge (black) and the lowpassed signal (blue). The figure b) shows the Fourier transform of the signals. The figure c) shows the fit of a linear dependency between current measured and the first derivative of voltage applied. The figure d) is an enlarged interval before the discharge used to reconstruct the stray current.The figure e) is the final result of the signal preprocessing (red signal). Shot: #36709.

($T_e \approx 7.5$ eV), similar in all 4 discharges, indicates that all the measurements are preformed in the main (or far) SOL of plasma. The T_i measurements with 5 μs and 10 μs resolution are in agreement in terms of the measured T_i and T_i fluctuation. However, the measurements with 5 μs provide more relevant data, improving the size of a statistical sample. Measurements with both resolutions indicate the presence of the background plasma with $T_i \approx T_e$ and a presence of intermittent blobs.

Histograms corresponding to the same discharges and the same intervals are plotted in Fig. 4.15 and 4.16. Since the discharge parameters are changing we are limited to only a short time interval, limiting the size of a statistical sample. We observe the non-Gaussian shaped T_i histograms with a tail toward high energies as was observed on COMPASS. The ion temperature of the background plasma appears to be higher than the electron temperature, which might be related to the gradual retraction of the plasma column.

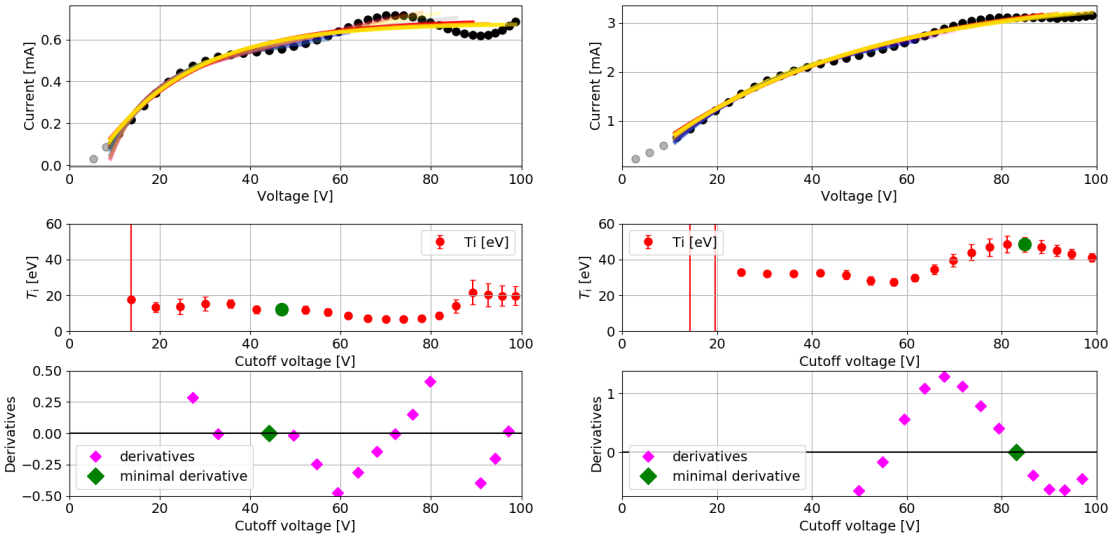

Figure 4.12: Example of a 4-parameter fit of the electron branch using cut-off method with temporal resolution of 5 μs at a radial position $R = 65$ mm. A fit is shown resulting in low T_i (left) and high T_i (right). Shot: #36709

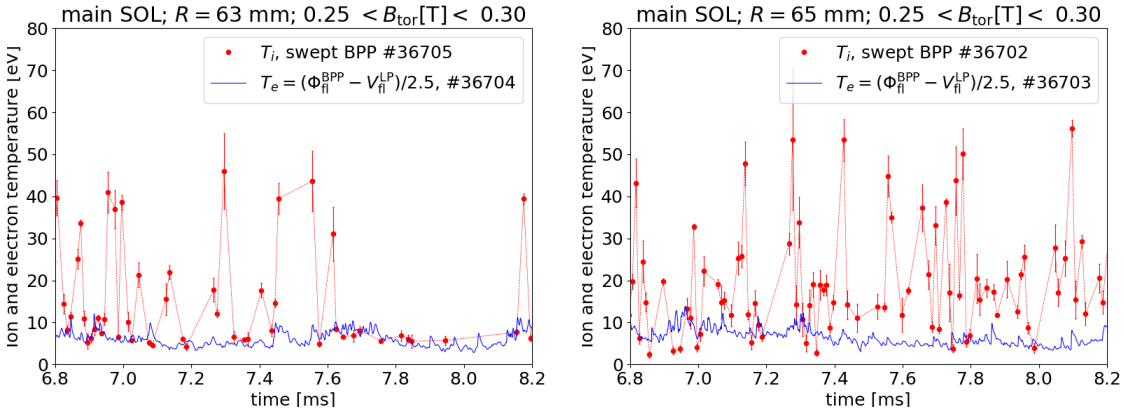

Figure 4.13: Comparison of the T_i temporal evolution, obtained with 10 μs resolution at two different radial positions. $R = 65$ mm is shown on the left and $R = 63$ mm is shown on the right.

4.3.6 Ion temperature obtained from RFA-like *I-V* characteristics

In order to create an average temperature profile we again need to take into consideration all the changes of the discharge and divide the discharge into intervals with near constant macroscopic plasma parameters. However, choosing particular time intervals can prove to be misleading, since the discharges are not perfectly synchronized. For this reason we have divided the discharge into intervals according to strength of magnetic field, rather than time. Since the histograms of fast measurements reveal non-Gaussian distribution of T_i we cannot simply assign mean and a standard deviation of the ion temperature to any interval of the discharge, but rather simulate the RFA-like *I-V* characteristics and perform a linear fit (as was described in section 3.5.2). And example of a construction and fitting of these synthetic *I-V* characteristics is shown in Fig. 4.17 and 4.18.

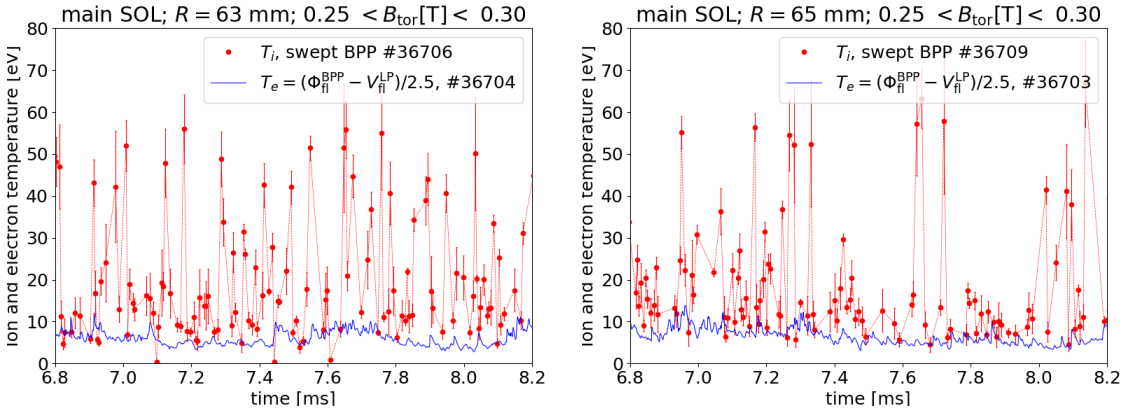

Figure 4.14: Comparison of the T_i temporal evolution, obtained with 5 μs resolution at two different radial positions. $R = 65$ mm is shown on the left and $R = 63$ mm is shown on the right.

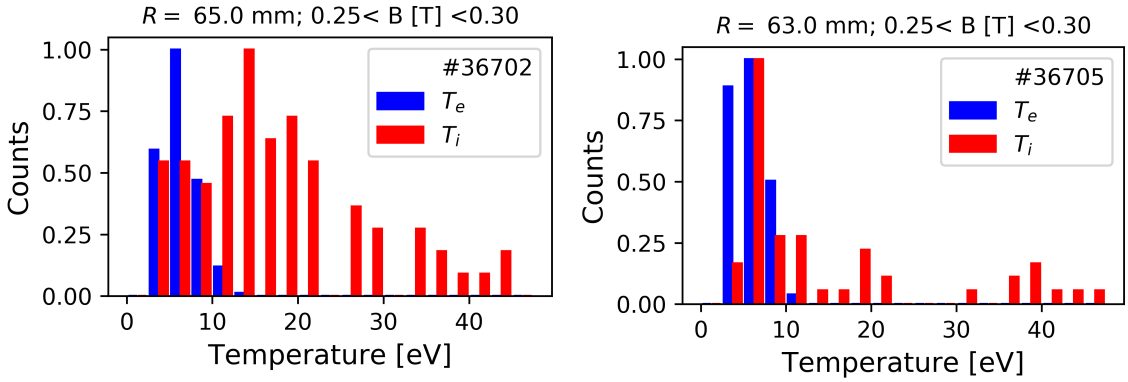

Figure 4.15: The ion and electron temperature histograms resulting from measurements with 10 μs resolution at two radial positions on Golem.

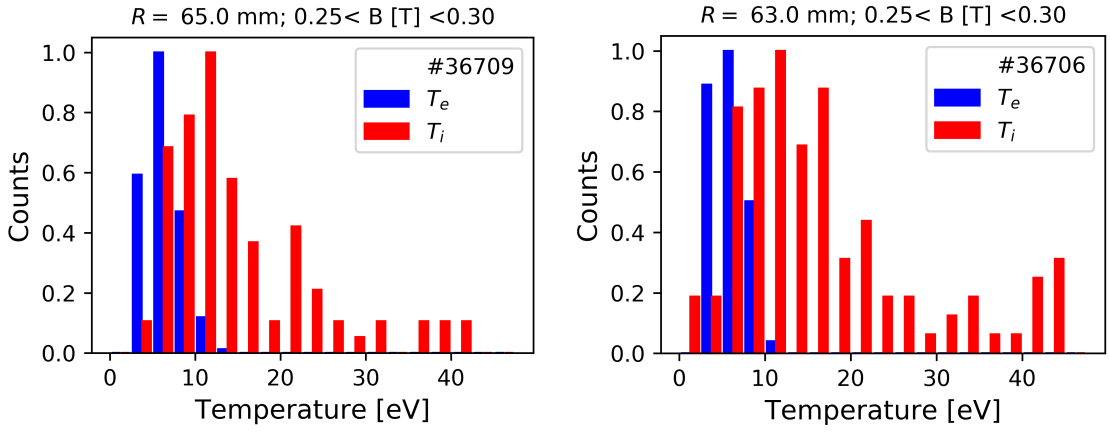

Figure 4.16: The ion and electron temperature histograms resulting from measurements with 5 μs resolution at two radial positions on Golem.

4.3.7 Summary

Using the Ball-pen and Langmuir probes we were able to measure the ion and electron temperature during discharges (#36690 - #36709) at eight different radial positions. Ion temperature measure-

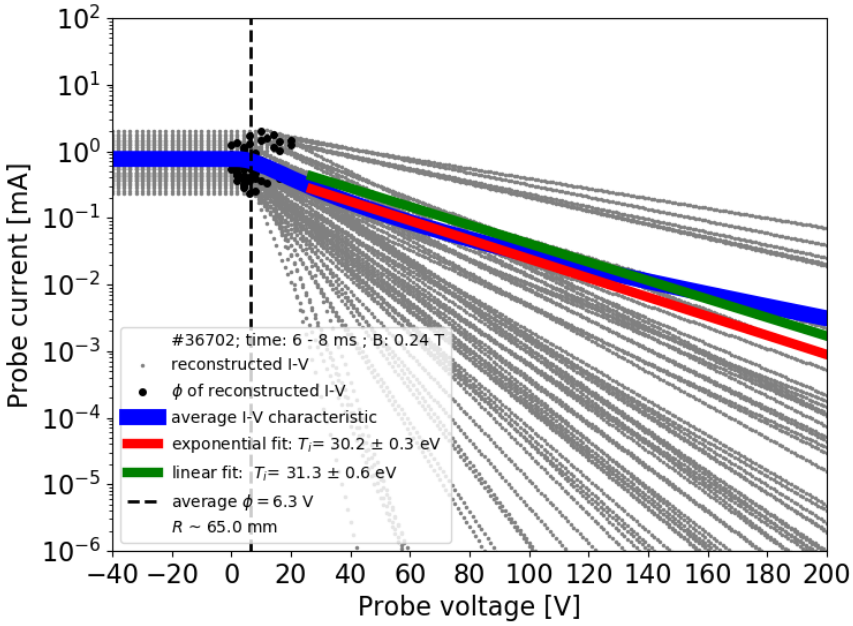

Figure 4.17: Example of a linear and exponential fit of the RFA-like *I-V* characteristic, shot: 36702. Radial position $R = 65$ mm, probe swept at $f = 50$ kHz.

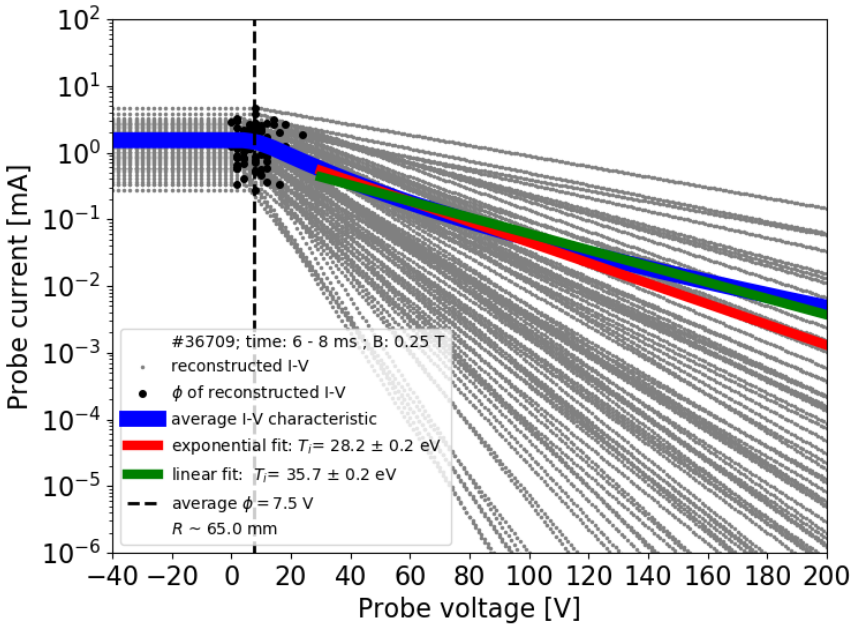

Figure 4.18: Example of a linear and exponential fit of the RFA-like *I-V* characteristic, shot: 36709. Radial position $R = 65$ mm, probe swept at $f = 100$ kHz.

ments were preformed during an interval where the intensity of a magnetic field B_{tor} ranged from 0.22 to 0.34 T. Since during this interval the plasma column was already retracted away from the

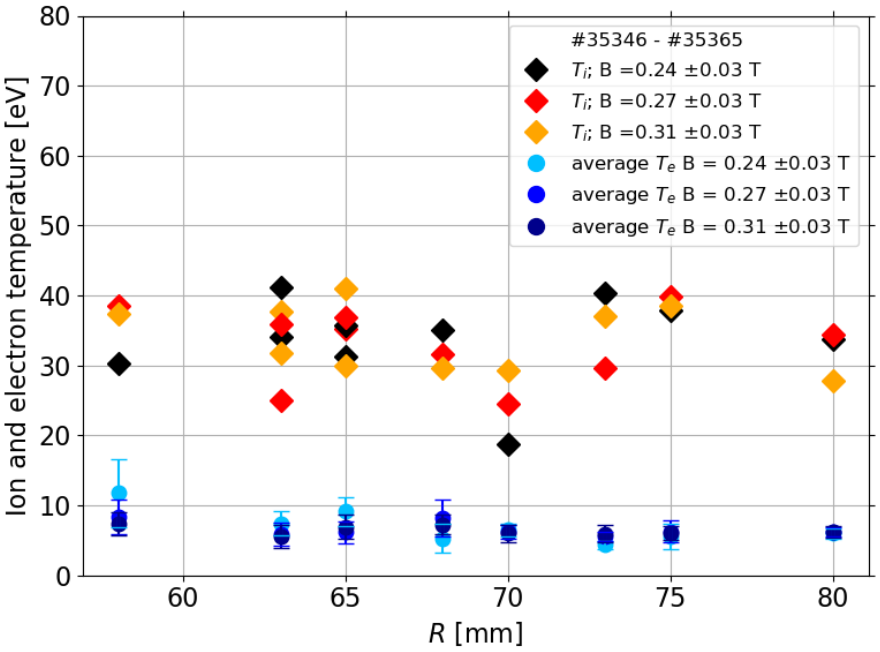

Figure 4.19: The resulting radial profile of ion and electron temperature, obtained by fitting the RFA-like *I-V* characteristics. The data points of the same color trace the same toroidal magnetic field in different discharges.

probes, all the measurements were performed in the main (or far) SOL. As a result, no radial gradient of the ion or electron temperature was found. Measurements reveal ion temperatures ranging approximately between 5 eV to 30 eV with short bursts up to $\approx$ 50 eV. Ion temperatures were successfully obtained with an increased 5 μs temporal resolution showing a decrease of the data fluctuation during measurement of individual *I-V* characteristics. Thus providing the expected improvement in number of successfully converged fits. The resulting values of average T_i (obtained from RFA-like *I-V* characteristics) and average T_e measured in the main and far SOL regions show $T_\mathrm{i} > T_\mathrm{e}$ by a factor of 3-5. Dependency of the T_i on the magnetic field strength was not found. Next steps toward improvement of the measurements on Golem are:

- stabilization of the plasma column position
- installation of the probes on the horizontal manipulator instead of the vertical manipulator
- decrease of the BPP collector depth and subsequent calibration to the optimal magnetic field range

Conclusion

Experimental data presented in this thesis were obtained on the tokamak COMPASS of the IPP CR and on the tokamak Golem operated by the Czech Technical University. The goal of this research was to further explore and confirm the possibility of the ion temperature measurement in the scrape-off layer (SOL) of plasma using the ball-pen probe. First results of this research were presented on the ECPD (European Conference on Plasma Diagnostics) in May 2019. Completed results were later published in the Nuclear Fusion journal [34]. Moreover, an improved analysis technique was developed during preparation of this thesis, increasing the amount of relevant data obtained and supplementing the statistical characterization of the SOL. The first results from the tokamak Golem were submitted to the EPS conference in Jun 2021.

Systematic measurements were performed in the edge plasma with different line-averaged electron densities on COMPASS. The ion temperatures obtained with uniquely high temporal resolution (10 μs) show non-Gaussian ion temperature histograms with a tail extending toward high temperatures. Currently the same temporal resolution cannot be achieved by any other experimental technique, however the results are in a good qualitative agreement with numerical simulations [29]. Moreover, a fluctuation study of both the ion and electron temperature reveal that the plasma turbulence conforms to Gamma distribution, which is in a good agreement with a stochastic model of the intermittent plasma fluctuations in the SOL [38]. The ion temperature fluctuations were never experimentally studied before. The ion temperatures obtained with a low temporal resolution (3 ms) from emulated RFA-like *I-V* characteristics show a clear radial profile of the T_i in the SOL. Similar trends of the T_i profile with 3 ms resolution is commonly observed with RFA on devices such as ASDEX-U. Nevertheless, recent measurements using fast swept (10 kHz) RFA show the importance of fast T_i measurements for an accurate reconstruction of the ion temperature histograms. Measurements in discharges with different line-averaged densities reveal an increase of the ion temperature with decreasing density, which complies with measurements using RFA [10]. Resulting ion-to-electron temperature ratios are found as 1-2 in the vicinity of LCFS and 3-4 in the main SOL.

First ion temperature measurements with 5 and 10 μs temporal resolution were successfully achieved on Golem. The calibration constant $\alpha_\mathrm{BPP} = 0.25 \pm 0.09$ was precisely calculated for the toroidal magnetic field $B_\mathrm{tor} > 0.22$. Fluctuations of the ion temperature ranging between 5 eV up to 60 eV reveal the turbulent behavior of the edge plasma. The RFA-like *I-V* characteristics were also analyzed for different strength of the toroidal magnetic field at different probe positions. The temperature gradient was not found, due to significant movement of the plasma column away from the probes, when the magnetic field $B_\mathrm{tor} > 0.24$ T is applied. Thus, all the measurements correspond to the main (or far) SOL region and show ion-to-electron temperature ratios of 3-5.

This study presents a new ion temperature measurement technique able to account for the turbulent nature of the SOL and demonstrates that only fast measurements are relevant for the understanding of T_i behavior in the SOL.

Appendix

nuclear fusion
IAEA

PAPER

Ion temperature measurements in the tokamak scrape-off layer with high temporal resolution

To cite this article: J. Adamek *et al* 2021 *Nucl. Fusion* **61** 036023

View the article online for updates and enhancements.

IOP ebooks™

Bringing together innovative digital publishing with leading authors from the global scientific community.

Start exploring the collection–download the first chapter of every title for free.

This content was downloaded from IP address 78.98.198.143 on 18/02/2021 at 15:28

IOP Publishing | International Atomic Energy Agency Nuclear Fusion

Nucl. Fusion **61** (2021) 036023 (6pp) https://doi.org/10.1088/1741-4326/abd41d

Ion temperature measurements in the tokamak scrape-off layer with high temporal resolution

J. Adamek[1,*], D. Cipciar[2], A. Devitre[3], J. Horacek[1], J. Cavalier[1], M. Komm[1], J. Krbec[1], M. Tichy[4], D. Trunec[2], P. Böhm[1], R. Panek[1] and the COMPASS team[1]

[1] Institute of Plasma Physics of the CAS, Prague, 18200, Czech Republic
[2] Faculty of Science, Masaryk University, Brno, 61137, Czech Republic
[3] Department of Nuclear Science and Engineering, Massachusetts Institute of Technology, Cambridge MA United States of America
[4] Charles University, Faculty of Mathematics and Physics, Prague, 12116, Czech Republic

E-mail: adamek@ipp.cas.cz

Received 12 October 2020, revised 14 December 2020
Accepted for publication 16 December 2020
Published 15 February 2021

Abstract

We present a uniquely fast (10 μs) ion temperature measurements in the tokamak edge plasma. Our approach is based on the sweeping of a ball-pen probe, where the ion temperature is obtained by fitting the electron branch of the corresponding I–V characteristic. We have performed measurements on the COMPASS tokamak during L-mode discharge. The temperature histograms reveal a non-Gaussian shape with a high-temperature tail peaking at low values. The fitted values of fast I–V measurements can be used to reconstruct (emulate) the slow swept I–V characteristic of a retarding field analyzer. The resulting ion temperature profile is nearly flat and provides a ratio of ion to electron temperature close to 1–2 in the vicinity of the last closed flux surface during L-mode discharges, as observed on other tokamaks.

Keywords: plasma, magnetic-confinement fusion, L-mode, ion temperature

(Some figures may appear in colour only in the online journal)

1. Introduction

The ion and electron temperatures, T_i and T_e, are essential parameters of magnetic fusion devices. The ion energy is crucial especially for physical sputtering of the tungsten material of plasma facing component [1]. The edge electron temperature is commonly measured by probe diagnostics with high and low temporal resolution [2–5]. Conversely, ion temperature measurements are typically limited to a few kHz using e.g. a retarding field analyzer (RFA) [6–9]. Applying a fast-swept voltage to this diagnostic is challenging because the measured current—on the level of tens of microamps—is very small compared to the parasitic current of the coaxial cable. For example, 100 V at a frequency of 50 kHz causes ~30 mA of parasitic current over a 5 m coaxial cable. However, recent measurements on ASDEX Upgrade using RFA with a higher sweeping frequency of 10 kHz [8] show that only fast sweeping should be used in intermittent scrape-off layer (SOL) plasmas for an accurate reconstruction of the ion temperature histograms.

Another possibility to measure the ion temperature is to use the Katsumata probe [10]. This probe technique has a high effective signal, but it requires sweeping both the collector and the metal shielding tube [10, 11]. This needs a complex isolation of the conducting parts within the graphite body of the probe head [12]. The segmented tunnel probe [10, 13] can also provide T_i with high temporal resolution. However, the interpretation of the measured signal relies on PIC simulations. Alternatively, the ball-pen probe (BPP) has a total current in

* Author to whom any correspondence should be addressed.

 © 2021 EURATOM Printed in the UK

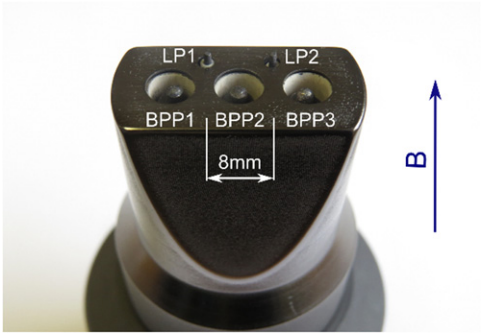

Figure 1. Probe head with three BPPs and two Langmuir probes. BPP3 is biased by a sweeping voltage at 50 kHz.

the order of 100 mA [2], large enough to use sweeping frequencies of 50 kHz, and can measure the ion temperature without a complex insulation system or the need for simulations. The sweeping frequency 50 kHz (10 μs per I–V characteristic) is already within the range of the typical blob autocorrelation time (10–20 μs) on COMPASS (figure 2 in [14]).

Its simple build [15] is designed to capture the ions by leveraging their larger gyro-radius as compared to the electrons. Nevertheless, detailed 3D PIC simulations have shown that it is the $E \times B$ drift, which mainly transports particles towards the collector [16]. Some of the electrons are therefore collected, resulting in a symmetric I–V characteristic [2, 17] where the floating potential (Φ^{BPP}) is approximately equal to the plasma (space) potential. In the following we assume that the electron branch of the BPP characteristic is the sum of the ion current, exponentially decaying with coefficient T_i, and the electron current, saturated or linearly increasing with the applied voltage. The ion temperature T_i can thus be obtained with high temporal resolution by fitting the exponential part of the electron branch.

2. Experimental setup and description of the method

A fast reciprocating probe head (see figure 1) [2], with ball-pen and Langmuir pins, is installed at the COMPASS midplane manipulator and inserted into the SOL during L-mode discharges. The BPP have stainless steel collectors with a diameter of 2 mm and an alumina shielding with inner diameters of 5 mm. The Langmuir pins are made of graphite (0.9 mm in diameter) and protrude 1.5 mm into the plasma. The averaged reciprocation time is roughly 150 ms. BPP3 is biased with a voltage of 0 to +140 V, at a sweeping frequency of 50 kHz, via a 5 m coaxial cable (parasitic capacity 100 pF m^{-1}). The data is collected with a sampling rate of 5 MHz.

The electron branch of the BPP characteristic is measured when the bias voltage is above the plasma potential Φ. The probe current is there described by a general formula for non-saturated I–V characteristics, where the former term gives the linear growth of the electron current, while the latter corresponds to the exponential decay of the ion current.

$$I(V) = I_{\mathrm{sat}}^{-}[1 + K(V - \Phi)] - I_{\mathrm{sat}}^{+} \exp\left(\frac{\Phi - V}{T_\mathrm{i}}\right). \quad (1)$$

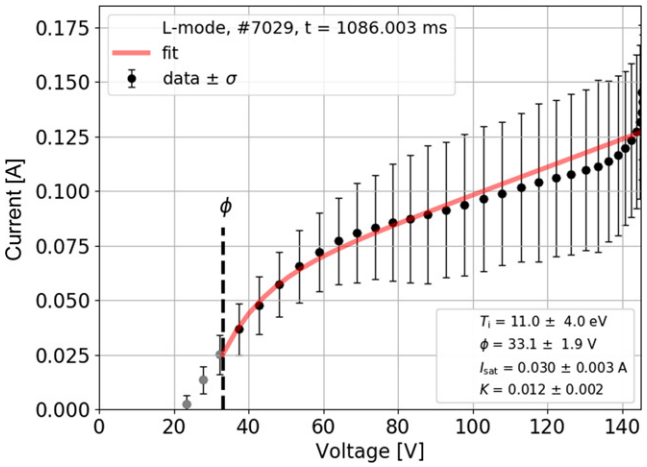

Figure 2. Electron branch ($V \geqslant \Phi \approx 35$ V) of a single-sweep BPP characteristic fitted by equation (3) using least-square minimization weighing each point by $1/\sigma$.

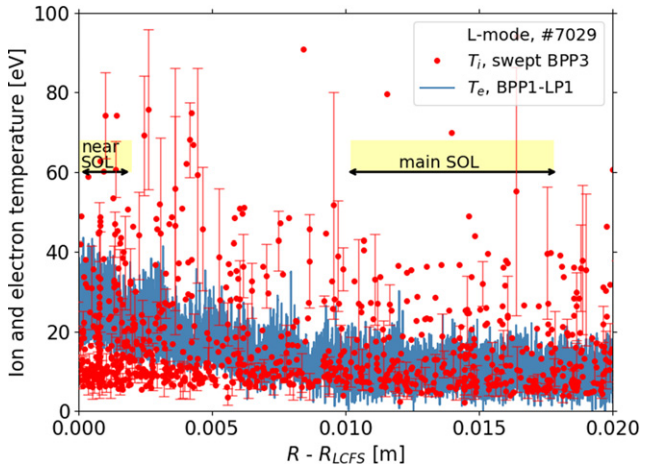

Figure 3. Radial profile of T_i and T_e. The position of the probe is shown on the x-axis with respect to the coordinate of the LCFS in the outer midplane. For clarity, the absolute error bars are only shown for a few points.

The values I_{sat}^{-} and I_{sat}^{+} represent the electron and ion saturation currents, respectively. The coefficient K represents the slope $\Delta I/\Delta V$ of the non-saturated part of the I–V characteristic. Such a linear coefficient is routinely used to account for sheath expansion in fitting the non-saturated ion branch of Langmuir probe I–V characteristics, equation (2) in [18]. The linear increase of the electron current has been reproduced in PIC simulations (chapter 4 in [16]) and awaits theoretical explanation. The coefficient K is equal to 0 when the electron current is fully saturated above Φ. We introduce the ratio between the electron and ion saturation currents

$$\alpha = \ln\left(\frac{I_{\mathrm{sat}}^{-}}{I_{\mathrm{sat}}^{+}}\right). \quad (2)$$

For the BPP measurements, a value of $\alpha_{\mathrm{BPP}} = 0.6$ can be used on COMPASS [2], as well as AUG [17]. The combination of the equation (1) and (2) leads to a general four-

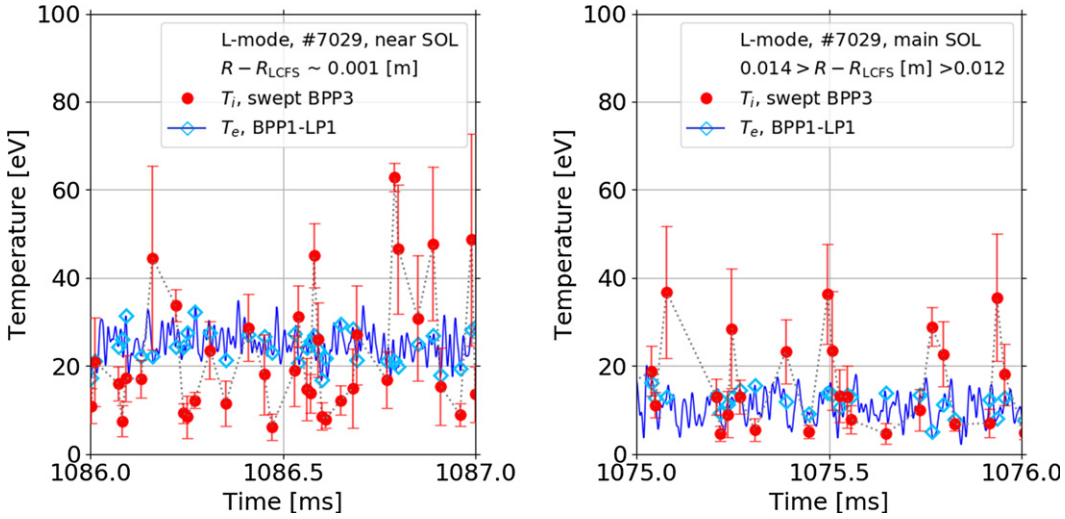

Figure 4. Example of the temporal evolution of T_i (red circles) and T_e (blue line and diamonds) in the near SOL (left) and in the main SOL (right). The electron temperature is plotted with high temporal resolution (line) and with points (diamonds) corresponding to the time of T_i measurements.

parameter fitting formula of the electron branch of the BPP I–V characteristic

$$I(V) = I_{sat}^{+} \cdot \left(\exp(\alpha_{BPP}) \cdot [1 + K \cdot (V - \Phi)] - \exp\left(\frac{\Phi - V}{T_i}\right)\right). \quad (3)$$

Previous work on AUG [19] used a three-parameter fitting formula, with $K = 0$, and the assumption that $I_{sat}^{-} = I_{sat}^{+}$. However, it was found that in many cases the electron branch is not fully saturated ($K > 0$) and that the strict application of three-parameter fitting lead to an overestimation of T_i. The probe head can also simultaneously provide T_e, with high-temporal resolution, combining the floating potentials measured by LP1 (V_{fl}^{LP}) and BPP2 (Φ^{BPP}):

$$T_e = \frac{\Phi^{BPP} - V^{LP}}{\alpha_{LP-}\alpha_{BPP}} = \frac{\Phi^{BPP} - V^{LP}}{2.2}. \quad (4)$$

This technique is routinely employed on COMPASS ($\alpha_{LP} = 2.8$) [2, 20] and has been used on AUG, MAST and ISTTOK [2, 21–23].

3. Ion temperature profile measurements with 10 μs resolution

The main obstacle for high temporal resolution RFA measurements is the instrument's very low effective signal—in the order of tens of μA [6, 7]. This is generally incompatible with the large capacitive currents (tens of mA) caused by high sweeping frequencies. This problem can be overcome using BPP technique as it provides high enough effective signal. The capacitive current is typically reconstructed from the time derivative of the voltage and current measurements before the tokamak discharge. The reconstructed parasitic current is then subtracted from the current measurements during the whole discharge. This process reduces the parasitic contribution to the total current by a factor of 6 or 7. We also apply a low-pass filter to remove the frequencies above 370 kHz. The probe current and voltage are then split into individual I–V characteristics and fitted by equation (3). One difficulty is that the model is only valid for the electron branch ($V > \Phi$). Therefore, a first fit must be used to find the plasma potential, using all positive current values above the BPP floating potential. The fitting process is then repeated for current values strictly above the obtained plasma potential. All fittings use the least square technique with a weighing factor of $1/\sigma$, as shown in figure 2. The value σ of each point of the I–V characteristic is obtained as a standard deviation of all current fluctuations around the probe voltage +/−1 ms. We also check if the voltage range above the plasma potential is equal or larger than $3T_i$ where the linear part of the I–V characteristic starts to dominate. When this is not the case, a new iteration is done for which the four-parameter fitting formula is reduced to three-parameter ($K = 0$) to re-fit the I–V characteristic without the linear part. Following this approach, we analysed the measurements performed during L-mode discharge #7029 ($B_T = 1.15$ T, $I_P = 170$ kA, $n_e = 5 \times 10^{19}$ m^{-3}) with density on last closed flux surface (LCFS) $n_{e,LCFS} \sim 1 \times 10^{19}$ m^{-3} obtained by Li-beam diagnostic [24]. The resulting SOL ion temperature profile (T_i obtained every 10 μs), with a maximum relative error 60%, is plotted in figure 3. The graph also shows T_e with the same lowpass filter. The radial position of the probe head is plotted with respect to the position of the LCFS, routinely obtained on COMPASS [2] by finding the maximum of the plasma potential profile, where the electric field $E = -\text{grad}(\Phi)$ and the corresponding $E \times B$ flow is zero. It is evident that the T_i measurements are scattered rather than forming a clear profile. An example of the T_i and T_e temporal evolution from within the near SOL ($R - R_{LCFS} \sim 0.001$ m) and main SOL ($0.012 < R - R_{LCFS}$ [m] < 0.014 m) region is shown in figure 4. The electron temperature is plotted with high temporal resolution as well as with points corresponding to the time of T_i measurements. It is important to

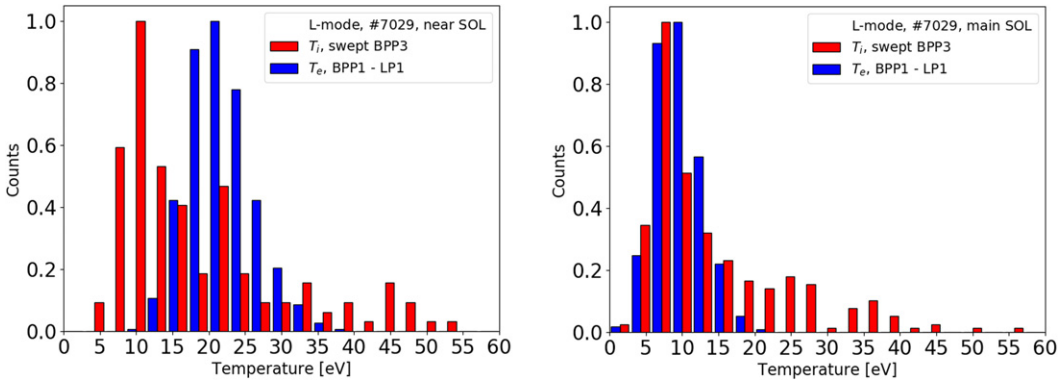

Figure 5. Ion and electron temperature histograms for near SOL (left) and main SOL (right) locations in shot #7029.

stress that T_i and T_e measurements are performed at different poloidal locations (displaced roughly by 15 mm on the probe head). Thus, the same event (blob) will be observed by T_i and T_e at different time with respect to its poloidal velocity (figure 9 in [25]). Note that the successfully obtained T_i values represents roughly 30% of all measured I–V characteristics. Thus, we can only see part of the temporal evolution with high resolution. The reason might be that the sweeping frequency is still not high enough to catch all blobs with shorter period and consequently the I–V characteristics are strongly deformed.

The T_i and T_e histograms for the near SOL ($0 < R - R_\mathrm{LCFS}$ [m] < 0.002) and the main SOL ($0.01 < R - R_\mathrm{LCFS}$ [m] < 0.018) regions are shown in figure 5. The T_i histogram has a non-Gaussian shape peaking at ∼10 eV, with a large tail up to ∼55 eV. The large tail may be the product of turbulent filamentary structures (blobs) [26] originating in the vicinity of the LCFS and propagating through the entire SOL. The low values may be attributed to the background plasma (figure 12 in [7]) and the impurity content [27]. These low values are similar for ions and electrons in the main SOL. We have also observed that the level of relative fluctuation, standard deviation of the temperature normalized by its mean value, decreases towards the LCFS for both T_i and T_e. It is a direct consequence of the blobby transport in SOL [2, 21, 23]. A secondary T_i maximum appears in the near SOL and corresponds to the maximum of the T_e histogram.

4. Ion temperature profiles from RFA-like *I–V* characteristics (low resolution)

In order to show an averaged profile, similar to a slow swept RFA, we have reconstructed the slow-swept RFA-like characteristics with period 3 ms using the fitted parameters obtained with the fast-swept BPP. The fitted values of T_i, Φ and $I_\mathrm{sat}{}^+$ from fast BPP measurements are used to reconstruct the RFA characteristic using the functional form:

$$I = I_\mathrm{sat}^+; (V < \Phi) \quad \text{and} \quad I = I_\mathrm{sat}^+ \exp\left(\frac{\Phi - V}{T_\mathrm{i}}\right); (V > \Phi)$$

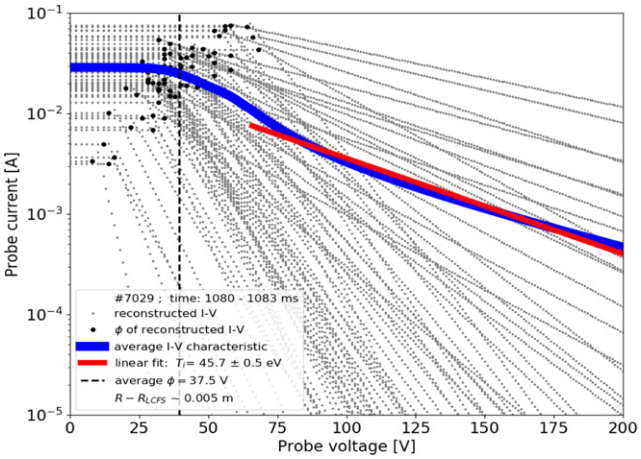

Figure 6. I–V characteristics reconstructed from fast swept BPP fittings (T_i, Φ and $I_\mathrm{sat}{}^+$) over a 3 ms interval in the vicinity of LCFS (#7029). The averaged I–V characteristic is fitted with the same upper limit for collector current as shown in [27].

These reconstructed I–V characteristics are then averaged over 3 ms intervals to create one slow (RFA-like) I–V characteristic of pure ion current, as shown in figure 6. The ion current decay in logarithmic scale, starting from the vicinity of the averaged plasma potential $\Phi \sim 38$ V, is fitted by a linear function with a current cut-off ($I_\mathrm{sat}{}^+/\mathrm{e}$) corresponding to roughly 37% of the nominal $I_\mathrm{sat}{}^+$ [27]. The result is that only the tail of the I–V characteristic is taken into account.

The ion temperatures obtained by the averaged (RFA-like) I–V characteristics from discharge #7029 and the complementary discharge #7034 (same plasma parameters) are shown in figure 7. The electron temperature profiles are obtained from fast BPP-LP measurements and smoothed down to the same temporal resolution and from the Thomson scattering system [28] as well. Both, T_i and T_e profiles show the good reproducibility of our measurements. The resulting T_i profile does not contain any low values, apparent in figure 3. This is to be expected since the fitting procedure applied on the tail of the I–V characteristic is dominated by blob temperatures, as pointed out in [26]. However, the T_i histograms may differ if the RFA (-like) I–V characteristics are fitted with different current cut-off or voltage cut-off, as noted in [8]. We see in

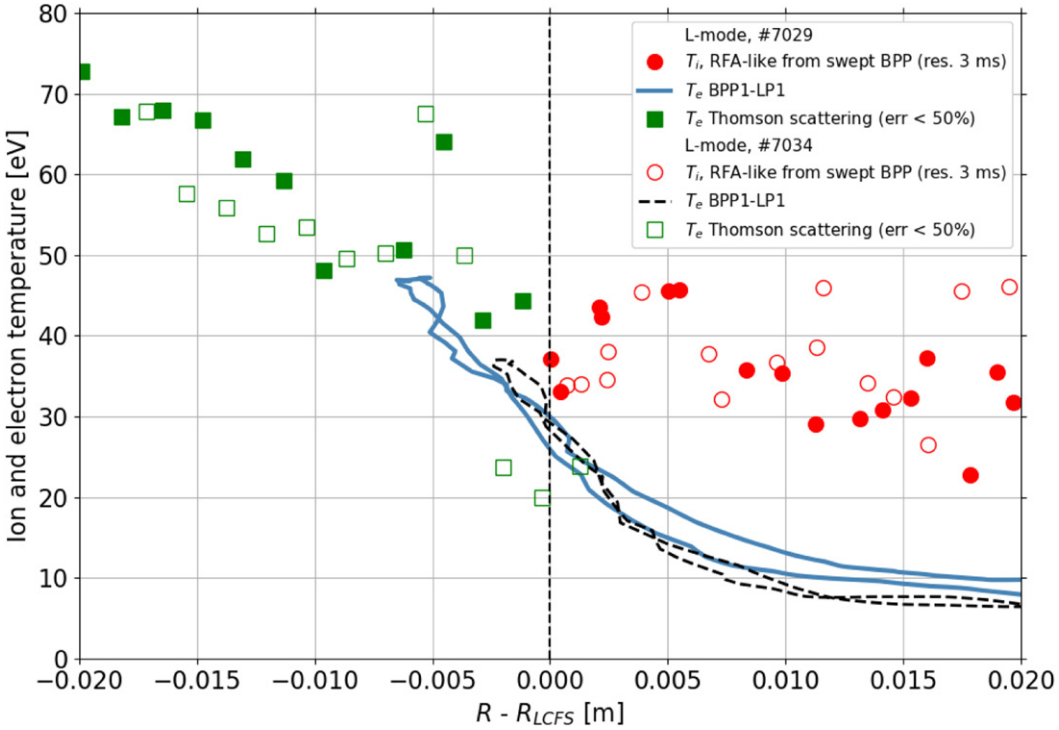

Figure 7. Ion temperature profiles obtained from averaged (RFA-like) I–V characteristics (circles) in two L-mode discharges #7029 and #7034 with the temporal resolution 3 ms. The electron temperature profile in SOL is obtained from fast BPP-LP measurements (line) and smoothed down to the same temporal resolution and Thomson scattering system (squares). The limiter is located around $R - R_{\mathrm{LCFS}} = 0.02$ m.

figure 7 that the ratio $T_\mathrm{i}/T_\mathrm{e}$ is larger in the main-SOL than in the vicinity of the LCFS. This was also observed on JET, KSTAR, EAST and AUG (cf figure 1 in [29]) where T_i is measured by other diagnostic systems.

5. Conclusion

We used the fast swept BPP technique to obtain fast measurements (every 10 μs) of the ion temperature during L-mode tokamak discharges on COMPASS. The BPP I–V characteristics are fitted by a four-parameter formula providing T_i, Φ and $I_{\mathrm{sat}}{}^{+}$. The resulting temperature histograms have a non-Gaussian shape with a peak at low temperatures and a tail towards high temperatures. This feature is observed in the near SOL as well as the main SOL. The large tail T_i values might be attributed to the filamentary turbulent structures (blobs) originating at the vicinity of LCFS and propagating through the SOL. The low values may correspond to the background plasma and the impurity content. In order to obtain an ion temperature profile with very low temporal resolution (similar to a slow swept RFA), we have used an averaged RFA-like I–V characteristics with the period 3 ms using fitted values of T_i, Φ and $I_{\mathrm{sat}}{}^{+}$ from fast BPP measurements. The resulting ion temperature profile is nearly flat and provides the ratio of ion to electron temperature close to 1–2 in the vicinity of the LCFS as it is observed on other tokamaks (JET, KSTAR, EAST, AUG).

Fast swept BPP technique reveals a broad spectrum of T_i values with the blob and background temperatures as similarly observed by recent RFA measurements on MAST and AUG, albeit a significantly higher temporal resolution. It is clear that the slow swept technique combines all these T_i values within a single I–V characteristic causing a difficult interpretation of the measurements. The BPP technique is robust and simple and features a very high effective signal allowing for T_i measurements at the edge of magnetic fusion facilities. It is reported in this work that we were able to successfully obtain 30% of all available data with 50 kHz sweeping frequency (5 MHz sampling frequency). Thus, with an even higher sweeping frequency (∼100 kHz) this diagnostic should be able to 'catch' more blob events with typical autocorrelation time 10–20 μs as shown for COMPASS (figure 2 in [14]). It is worth mentioning that using slow sweeping frequency (∼1 kHz , typical for RFA diagnostic) we would deliver only several points per 1 ms. Thus, our fast measurements resolve more data than it is typically achieved for T_i measurements.

Acknowledgments

The first author would like to thank M. Peterka for initial discussions on the fitting routines. This work has been carried out in the framework of the EUROFusion Consortium and has received funding from the Euratom research and training programme 2014–2018 and 2019–2020 under Grant agreement No. 633053. The views and opinions expressed herein do not necessarily reflect those of the European Commission. This investigation was supported projects MEYS #LM2018117, CZ.02.1.01/0.0/0.0/16_019/0000768 and IAEA CRP F13019 -

Research Contract No. 22727/R0. This work was also supported by the Czech Science Foundation within the project GACR 20-28161S and 19-00579S.

ORCID iDs

J. Adamek https://orcid.org/0000-0001-8562-1233
A. Devitre https://orcid.org/0000-0001-7428-0373
J. Horacek https://orcid.org/0000-0002-4276-3124
M. Komm https://orcid.org/0000-0001-8895-5802
J. Krbec https://orcid.org/0000-0002-3780-6257
D. Trunec https://orcid.org/0000-0003-0210-5087

References

[1] Guillemaut C. *et al* 2015 *Plasma Phys. Control. Fusion* **57** 085006
[2] Adamek J. 2016 *Rev. Sci. Instrum.* **87** 043510
[3] Demidov V.I., Ratynskaia S.V. and Rypdal K. 2002 *Rev. Sci. Instrum.* **73** 3409
[4] Silva C. and Gonçalves B. 2004 *Rev. Sci. Instrum.* **75** 4314
[5] LaBombard B. and Lyons L. 2007 *Rev. Sci. Instrum.* **78** 073501
[6] Kocan M., Gennrich F.P., Kendl A. and Müller H.W. 2012 *Plasma Phys. Control. Fusion* **54** 085009
[7] Allan S.Y., Elmore S., Fishpool G. and Dudson B. 2016 *Plasma Phys. Control. Fusion* **58** 045014
[8] Ochoukov R., Dreval M., Bobkov V., Faugel H., Herrmann A., Kammerloher L. and Leitenstern P. 2020 *Rev. Sci. Instrum.* **91** 063506
[9] Elmore S., Allan S.Y., Fishpool G., Kirk A., Thornton A.J., Walkden N.R. and Harrison J.R. 2016 *Plasma Phys. Control. Fusion* **58** 065002
[10] Adamek J. *et al* 2008 *Contrib. Plasma Phys.* **48** 395–9
[11] Komm M., Adamek J., Dejarnac R., Gunn J.P. and Pekarek Z. 2010 *Plasma Phys. Control. Fusion* **53** 015005
[12] Brunner D., LaBombard B., Ochoukov R. and Whyte D. 2013 *Rev. Sci. Instrum.* **84** 053507
[13] Kocan M., Panek R., Stöckel J., Hron M., Gunn J.P. and Dejarnac R. 2007 *J. Nucl. Mater.* **363–365** 1436–40
[14] Carralero D. *et al* 2015 *J. Nucl. Mater.* **463** 123–7
[15] Adámek J. *et al* 2004 *Czech. J. Phys.* **54** C95
[16] Murphy-Sugrue S., Harrison J., Walkden N.R., Bryant P. and Bradley J.W. 2017 *Plasma Phys. Control. Fusion* **59** 055007
[17] Adamek J. *et al* (ASDEX Upgrade Team) 2010 *Contrib. Plasma Phys.* **50** 854–9
[18] Tsui C.K., Boedo J.A. and Stangeby P.C. 2018 *Rev. Sci. Instrum.* **89** 013505
[19] Adamek J., Horacek J., Müller H.W., Schrittwieser R., Tichy M. and Nielsen A.H. 2011 *Proc. 38th EPS Conf. on Plasma Physics,* (Strasbourg, France) (http://ocs.ciemat.es/EPS2011PAP/pdf/P1.059.pdf)
[20] Adamek J. *et al* 2020 *Nucl. Fusion* **60** 096014
[21] Horacek J., Adamek J., Müller H.W., Seidl J., Nielsen A.H., Rohde V., Mehlmann F., Ionita C. and Havlíčková E. 2010 *Nucl. Fusion* **50** 105001
[22] Walkden N.R., Adamek J., Allan S., Dudson B.D., Elmore S., Fishpool G., Harrison J., Kirk A. and Komm M. 2015 *Rev. Sci. Instrum.* **86** 023510
[23] Silva C., Adamek J., Fernandes H. and Figueiredo H. 2015 *Plasma Phys. Control. Fusion* **57** 025003
[24] Krbec J., Háček P., Berta M., Seidl J., Hron M. and Pánek R. 2018 *Rev. Sci. Instrum.* **89** 113504
[25] Cavalier J. *et al* 2019 *Nucl. Fusion* **59** 056025
[26] Nielsen A.H. *et al* 2017 *Plasma Phys. Control. Fusion* **59** 025012
[27] Kocan M. and Gunn J.P. 2011 *Plasma Phys. Control. Fusion* **53** 085016
[28] Bilkova P., Bohm P., Aftanas M., Sos M., Havranek A., Sestak D., Weinzettl V., Hron M. and Panek R. 2018 *J. Instrum.* **13** C01024
[29] Kocan M. *et al* 2011 *J. Nucl. Mat.* **415** S1133–8

Bibliography

[1] Iliadis, C. Nuclear Physics of Stars. Weinheim: Wiley-VCH. ISBN 9783527406029, 2007

[2] Bittencourt, J. A. Fundamentals of plasma physics. 3rd ed. New York: Springer, c2004. ISBN 0-387-20975-1.

[3] Freidberg, Jeffrey P. Plasma Physics and Fusion Energy. Cambridge University Press, 2008.

[4] Sevillano, M. Sliding-mode loop voltage control using ASTRA-Matlab integration in Tokamak reactors. International journal of innovative computing, information and control: IJICIC 8(9), 2012.

[5] Goldston, R. J. Introduction to plasma physics. Bristol, UK: Institute of Physics Pub, 1997.

[6] Kates-Harbeck, J. Predicting disruptive instabilities in controlled fusion plasmas through deep learning. Nature. doi:10.1038/s41586-019-1116-4, 2019

[7] CHEN, F. F. (2016). INDISPENSABLE TRUTH: How fusion power can save the planet. SPRINGER.

[8] Ion temperature gradient instability. (n.d.). Retrieved March 25, 2021, from http://fusionwiki.ciemat.es/wiki/Ion_Temperature_Gradient_instability#:~:text=The%20ion%20temperature%20gradient%20(ITG,nature%20of%20Grad-B%20drift.

[9] Whyte, D. G. I-mode: an H-mode energy confinement regime with L-mode particle transport in Alcator C-Mod. Nuclear Fusion, 50(10), 105005. doi:10.1088/0029-5515/50/10/105005, 2010.

[10] Matthews, G. F. (1994). Tokamak plasma diagnosis by electrical probes. Plasma Physics and Controlled Fusion, 36(10), 1595-1628. doi:10.1088/0741-3335/36/10/002

[11] Federici, G. (2001). Plasma-material interactions in CURRENT tokamaks and their implications For NEXT-STEP fusion reactors. doi:10.2172/773280

[12] "TrainingCourses/FTTF/2014-2015/MatCveng/Index." Sitewide ATOM, golem.fjfi.cvut.cz/wiki/TrainingCourses/FTTF/2014-2015/MatCveng/index.

[13] Adámek, J. et al. Direct measurements of the plasma potential in ELMy Hmode plasma with ball-pen probes on ASDEX Upgrade tokamak. Journal of Nuclear Materials. 2009, 1114–1117. ISSN 0022-3115. doi: 10. 1016/j.jnucmat.2009.01.286. , from http://www.sciencedirect.com/science/article/pii/S0022311509003110. [online][cit. 2019-04-18].

[14] Adámek, J., Müller H., Silva C., et al. Profile measurements of the electron temperature on the ASDEX Upgrade, COMPASS, and ISTTOK tokamak using Thomson scattering, triple, and ball-pen probes. Review of Scientific Instruments [online]. 2016, 87(4) [cit. 2019-03-31]. DOI: 10.1063/1.4945797. ISSN 0034-6748. Accessible from: http://aip.scitation.org/doi/10.1063/1.4945797

[15] Adamek, J. Profile measurements of the electron temperature on the ASDEX Upgrade, COMPASS, and ISTTOK tokamak using thompson scattering, triple, and ball-pen probes. Review of Scientific Instruments, 87(4), 043510. doi:10.1063/1.4945797, 2016.

[16] Tsui, C. K. Accounting for Debye sheath expansion for Proud langmuir probes in magnetic confinement FUSION PLASMAS. Review of Scientific Instruments, 89(1), 013505. doi:10.1063/1.4995353, 2018

[17] Kočan, M., Gunn, J. P. Influence of impurities on ion temperature measurements in the tokamak scrape-off layer by retarding field analysers. Plasma Physics and Controlled Fusion [online]. 2011, 53(8) [cit. 2019-05-04]. DOI: 10.1088/0741-3335/53/8/085016. ISSN 0741-3335. Accessible from: http://stacks.iop.org/0741-3335/53/i=8/a=085016?key=crossref.e9b380fa27758c52d9de98e48a097548

[18] Ochoukov, R. (2020). Ion temperature measurement techniques using fast sweeping RETARDING FIELD analyzer (RFA) in STRONGLY intermittent Asdex upgrade tokamak plasmas. Review of Scientific Instruments, 91(6), 063506. doi:10.1063/5.0010788

[19] Matthews, G. F. (1984). A combined retarding field analyser and e×b probe for measurement of ion and electron energy distribution in tokamak edge plasmas. Journal of Physics D: Applied Physics, 17(11), 2243-2254. doi:10.1088/0022-3727/17/11/011

[20] Murphy-Sugrue, S., Harrison, J., Walkden, Improved understanding of the ball-pen probe through particle-in-cell simulations. Plasma Physics and Controlled Fusion [online]. 2017, 59(5) [cit. 2019-03-31]. DOI: 10.1088/1361-6587/aa60d0. ISSN 0741-3335. Accessible from: http://stacks.iop.org/0741-3335/59/i=5/a=055007?key=crossref.cdd362d2b0d2b9019824163ae59c4829

[21] Adámek, J., Stöckel, J., Hron, M., et al. A novel approach to direct measurement of the plasma potential. Czechoslovak Journal of Physics [online]. 2004, 54(S3), C95-C99 [cit. 2019-05-04]. DOI: 10.1007/BF03166386. ISSN 0011-4626. Accessible from: http://link.springer.com/10.1007/BF03166386

[22] Adámek, J. et al. Ball-Pen Probe Measurements in L-Mode and H-Mode on ASDEX Upgrade. Contributions to Plasma Physics. 2010, 50, 9, s. 854–859. ISSN 1521-3986. doi: 10.1002/ctpp.201010145. [online][cit. 2019-03-24].

[23] Adámek J., Stöckel J., Ďuran I., et al. Comparative measurements of the plasma potential with the ball-pen and emissive probes on the CASTOR tokamak. Czechoslovak Journal of Physics [online]. 2005, 55(3), 235-242 [cit. 2019-03-31]. DOI: 10.1007/s10582-005-0036-8. ISSN 0011-4626. Accessible from: http://link.springer.com/10.1007/s10582-005-0036-8

[24] 18Th SUMTRAIC - 2020. (n.d.). Retrieved April 19, 2021, from https://indico.ipp.cas.cz/event/18/

[25] Tokamak parametres - ipp.cas.cz [online] Accessible from: http://www.ipp.cas.cz/vedecka_struktura_ufp/tokamak/tokamak_compass/

[26] Shot list - COMPASS logbook. Accessible from: logbook.tok.ipp.cas.cz

[27] Müller, H.W., Adámek, J., Cavazzana, R., et al. Latest investigations on fluctuations, ELM filaments and turbulent transport in the SOL of ASDEX Upgrade. Nuclear Fusion [online]. 2011, 51(7) [cit. 2019-05-04]. DOI: 10.1088/0029-5515/51/7/073023. ISSN 0029-5515. Accessible from: http://stacks.iop.org/0029-5515/51/i=7/a=073023?key=crossref.1f1fd59e5a18c5df2c04ae3591d48567

[28] Boedo, J. A., Rudakov, D. L., Moyer, (2003). Transport by intermittency in the boundary of the DIII-D tokamak. Physics of Plasmas, 10(5), 1670–1677. https://doi.org/10.1063/1.1563259

[29] Nielsen, H., Rasmussen, J., Madsen, J., et al. Numerical simulations of blobs with ion dynamics. Plasma Physics and Controlled Fusion [online]. 2017, 59(2) [cit. 2019-04-28]. DOI: 10.1088/1361-6587/59/2/025012. ISSN 0741-3335. http://stacks.iop.org/0741-3335/59/i=2/a=025012?key=crossref.240c51a7a5503c0485858b6ef701941c

[30] Jirakova, K., Kovanda, O., Adamek, J., (2019). Systematic errors in tokamak magnetic equilibrium reconstruction: a study of EFIT++ at tokamak COMPASS. Journal of Instrumentation, 14(11). https://doi.org/10.1088/1748-0221/14/11/c11020

[31] Carralero, D. Implications of high DENSITY operation on SOL Transport: A Multimachine investigation. Journal of Nuclear Materials, 463, 123-127. doi:10.1016/j.jnucmat.2014.10.019, 2015

[32] M., Varavin, A., Naydenkova, (2019). Study for the microwave interferometer for high densities plasmas on COMPASS-U tokamak. Fusion Engineering and Design. doi:10.1016/j.fusengdes.2019.03.051

[33] Elmore, S., Allan, S. Y., Fishpool, (2016). Scrape-off layer ion temperature measurements at the divertor target during type III and type I ELMs in MAST measured by RFEA. Plasma Physics and Controlled Fusion, 58(6), 065002.https://doi.org/10.1088/0741-3335/58/6/065002

[34] Adamek, J., Cipciar, D., Devitre, A., (2021). Ion temperature measurements in the tokamak scrape-off layer with high temporal resolution. Nuclear Fusion, 61(3), 036023. https://doi.org/10.1088/1741-4326/abd41d

[35] Horáček, J., Adámek, J., Müller, H.W. et al. Interpretation of fast measurements of plasma potential, temperature and density in SOL of ASDEX Upgrade. Nuclear Fusion [online]. 2010, 50(10) [cit. 2019-05-07]. DOI: 10.1088/0029-5515/50/10/105001. ISSN 0029-5515. http://stacks.iop.org/0029-5515/50/i=10/a=105001?key=crossref.176b9ce6cd2ce3fcc74a48317cd3a88c

[36] Horacek, J., Pitts, R. A., (2005). Overview of edge electrostatic turbulence experiments on TCV. Czechoslovak Journal of Physics, 55(3), 271–283. https://doi.org/10.1007/s10582-005-0040-z

[37] Havlíčková, E., Fundamenski (2011). Steady-state and time-dependent modelling of parallel transport in the scrape-off layer. Plasma Physics and Controlled Fusion, 53(6), 065004.https://doi.org/10.1088/0741-3335/53/6/065004

[38] Garcia, O. E. (2012). Stochastic Modeling of Intermittent Scrape-Off Layer Plasma Fluctuations. Physical Review Letters, 108(26). https://doi.org/10.1103/physrevlett.108.265001

[39] Theodorsen, A., Garcia, O. E., Horacek, J. (2016). Scrape-off layer turbulence in TCV: evidence in support of stochastic modelling. Plasma Physics and Controlled Fusion, 58(4), 044006. https://doi.org/10.1088/0741-3335/58/4/044006

[40] Labit, B., Diallo, A., Fasoli, A.,(2007). Statistical properties of electrostatic turbulence in toroidal magnetized plasmas. Plasma Physics and Controlled Fusion, 49(12B). https://doi.org/10.1088/0741-3335/49/12b/s26

[41] Kočan, M., Gunn, J. P., Carpentier-Chouchana, S., (2011). Measurements of ion energies in the tokamak plasma boundary. Journal of Nuclear Materials, 415(1). https://doi.org/10.1016/j.jnucmat.2010.08.036

[42] Tokamak golem wiki - front page. (n.d.). Retrieved March 26, 2021, from http://golem.fjfi.cvut.cz/wiki/

[43] Combined Langmuir AND BALL-PEN PROBE. (n.d.). Retrieved March 29, 2021, from http://golem.fjfi.cvut.cz/wiki/Diagnostics/ParticleFlux/BallPenProbe/index

[44] P. Mácha, Edge plasma parameter measurements of the GOLEM tokamak using ball-pen and Langmuir probe. Bachelor thesis, CVUT, 2018.

[45] Matthews, G. F. A combined retarding field analyser and $\vec{E} \times \vec{B}$ probe for measurement of ion and electron energy distribution in tokamak edge plasmas. Journal of Physics D: Applied Physics [online]. 1984, 17(11), 2243-2254 [cit. 2019-05-04]. DOI: 10.1088/0022-3727/17/11/011. ISSN 0022-3727. Accessible from: http://stacks.iop.org/0022-3727/17/i=11/a=011?key=crossref.5b162b8342c5c0ea644d45f512b23d9f

[46] Adámek, J., Kocan, M., Panek, R., et al. Simultaneous Measurements of Ion Temperature by Segmented Tunnel and Katsumata Probe. Contributions to Plasma Physics [online]. 2008, 48(5-7), 395-399 [cit. 2019-05-04]. DOI: 10.1002/ctpp.200810063. ISSN 08631042. Dostupné z: http://doi.wiley.com/10.1002/ctpp.200810063

[47] Popov, T. K., Ivanova, P., Stöckel, J., Dejanac R. Electron energy distribution function, plasma potential and electron density measured by Langmuir probe in tokamak edge plasma. Plasma Physics and Controlled Fusion [online]. 2009, 51(6) [cit. 2019-05-04]. DOI: 10.1088/0741-3335/51/6/065014. ISSN 0741-3335. Accessible from: http://stacks.iop.org/0741-3335/51/i=6/a=065014?key=crossref.a4c657fd13080a1f325fc2e7a45fe264